
Molecular Networks Through Surface-Mediated Reactions - From Hydrogen Bonds to Covalent Links



Dissertation
der Fakultät für Geowissenschaften
der Ludwig-Maximilians-Universität
München

Hermann Walch

München, den 14. September 2010

Erstgutachter: Prof. Dr. Markus Lackinger

Zweitgutachter: Prof. Dr. Wolfgang M. Heckl

Disputation: **16. Februar 2011**

Contents

Table of Contents	i
Abbreviations	iii
Abstract	v
1 Motivation	1
2 Experimental Methods	3
2.1 Introduction	3
2.2 Scanning Tunneling Microscopy	4
2.2.1 Basic Principle	4
2.2.2 Theoretical Description	5
2.2.3 Imaging Molecules	8
2.3 UHV System	9
2.3.1 Overview	9
2.3.2 Modifications of the Omicron VT STM	10
2.3.3 Electron Beam Tip Heater	11
3 Molecule-Molecule Interactions	13
3.1 Non-Covalent Bonds	13
3.2 Metal-Coordination Bonds	17
3.3 Covalent Bonds	20
4 Molecule-Substrate-Interactions and Reactivity	23
4.1 Physisorption	23
4.2 Chemisorption	26
4.3 Active Sites	29
4.4 2D Adatom Gas	31
5 Summary	35
6 Publications	37
6.1 Isotopological Supramolecular Networks from Melamine and Fatty Acids	37
6.2 Surface mediated synthesis of 2D covalent organic frameworks: 1,3,5-tris(4-bromophenyl)benzene on graphite(001), Cu(111), and Ag(110)	51
6.3 Material and Orientation dependent activity for heterogeneously catalyzed carbon-bromine bond homolysis	65

6.4	On the Scalability of Supramolecular Networks - High Packing Density vs Optimized Hydrogen Bonds in Tricarboxylic Acid Monolayers	73
6.5	Extended Two-dimensional Metal-Organic Frameworks Based on Thiolate-Copper Coordination Bonds	91
	References	97
	Acknowledgements	109
	Curriculum Vitae	111

Abbreviations

AFM	atomic force microscope
BTB	1,3,5-benzenetribenzoic acid
COF	covalent-organic framework
DFT	density functional theory
DOS	density of states
FCC	face centered cubic
HOMO	highest occupied molecular orbital
HOPG	highly oriented pyrolytic graphite
LDOS	local density of states
LEED	low energy electron diffraction
LUMO	lowest unoccupied molecular orbital
MOF	metal-organic framework
PDOS	projected density of states
RAHB	resonance-assisted hydrogen bonding
SAM	self-assembled monolayer
SPA-LEED	spot profile analysis - low energy electron diffraction
STM	scanning tunneling microscope
TBB	1,3,5-tris-(4-bromophenyl)benzene
TCBPB	1,3,5-tris[4'-carboxy(1,1'-biphenyl-4-yl)]benzene
TMA	trimesic acid
TDS	thermal desorption spectroscopy
TMB	1,3,5-tris(4-mercaptophenyl)benzene
TPD	temperature programmed desorption
TSK	terrace-step-kink
UHV	ultrahigh vacuum

Abstract

This thesis deals with adsorption, self-assembly, and surface reactions of organic molecules on solid substrates, with the aim to fabricate higher hierarchical two-dimensional (2D) structures. It is of genuine interest in materials science to develop strategies and methods for reproducible growth of extended molecular assemblies with specific and desired chemical, physical and functional properties. The experimental technique used was Scanning Tunneling Microscopy (STM) - an outstanding method to gain real space information of the atomic-scale realm of adsorbates on crystalline surfaces.

The investigated systems are characterized by a complex interplay between adsorbate-adsorbate interactions and adsorbate-substrate interactions. In one series of experiments this could be illustrated through self-assembly of hydrogen bonded heteromeric molecular networks on a chemically relatively inert graphite substrate. In this case, van-der-Waals forces between adsorbate and substrate have to be balanced with intermolecular hydrogen bonds in concert with weaker van-der-Waals forces. Since the magnitude of van-der-Waals forces between adsorbates and substrates correlates with the contact area, this type of interaction becomes more dominant for larger molecules. By stronger interactions which do not depend on molecule size, it was also possible to grow isotopological molecular networks, i.e. networks following a similar building plan. By varying for instance the length of aliphatic spacers, supramolecular structures with tuneable lattice parameter could be formed.

Studies of organic molecules on chemically more active metal substrates show that more complex processes can be involved. In particular the concept of reactivity and surface-catalyzed reactions are discussed and illustrated by an intuitive example. It is demonstrated that strong molecule-substrate interaction can induce unimolecular reactions such as deprotonation of molecules or more generally dissociation of intramolecular bonds. This interaction strength, thus substrate reactivity is highly influenced by a variety of factors which include material, crystallographic surface orientation, and temperature. Further more the importance of so-called active sites on crystal surfaces, i.e. special sites with significantly increased interaction strength, is taken into account and exemplified with experimental results. Exploiting these fundamental principles, C-Br bond scission of brominated aromatic compounds was demonstrated upon adsorption on reactive substrates and followed by successful incorporation in covalently bonded networks. However, irreversibility of covalent bonds prevents similar control and error correction mechanisms over the system as compared to hydrogen bonded networks. A high defect density and a low degree of ordering is the consequence for the resulting 2D structures.

In a final set of experiments aromatic thiol molecules could be assembled into highly or-

dered structures via metal-coordination bonds. The 2D gas of freely diffusing adatoms of a copper surface was thermally excited to finally transform a trithiolate precursor structure into metal-coordination networks via Cu-S metal coordination bonds. Two different coordination geometries were observed giving rise to the formation of two morphologically distinct phases. These studies revealed the impact of the adatom gas for surface reactivity and chemistry of metals.

1 Motivation

Nanoscale science and nascent nanotechnology aim at controlling matter on the smallest length scale accessible. For materials the ultimate building blocks which can be designed and synthesized are molecules. By altering size, geometry, and chemistry it is possible to tailor functionalities in unprecedented ways.^[1] Although some rather fantastic ideas as "assemblers", nanorobots, or the apocalyptic "grey goo" scenario have attracted popular interest in the past,^[2] organic thin films for instance are an example of successfully applied nanotechnology.^[3] They entered in particular the field of organic optoelectronics as electroluminescent devices^[4], photovoltaics,^[5] or organic field-effect transistors.^[6] Apart from these applications - still being macroscopic in two dimensions - one of the main driving forces for nanoscale science has up to now been the exciting vision of molecular electronics. If silicon based microelectronic technology continues to scale down according to Moore's law^[7] individual devices will soon reach the atomic scale, quickly exceeding the limits of fabrication with lithographic techniques. Already in 1974 Avram and Ratner theoretically introduced the concept for a molecular rectifier based on a single organic molecule.^[8] They suggested that an organic molecule with a donor-spacer-acceptor structure would behave like a diode when coupled to metallic electrodes. Some thirty years later, molecular electronics has become a very active field of research.^[9,10] A major difficulty is that physical concepts as electrical conductance cannot be applied to single molecules in a straightforward way,^[9,11,12] since quantum mechanical phenomena (and thus non-linear behavior) dominate nanoscale systems. This can also be seen as an advantage since most electronic devices are based on non-linear response behavior. The major challenges for future research will be addressing and contacting single molecules, in other words, architectural issues.^[13] However, impressive progress has already been made in fabricating and understanding nanoscale systems as for instance carbon nanotubes^[14], molecular wires^[8], switches^[15] or magnetic systems.^[16]

Now in order to synthesize novel functional nano-devices, a very promising approach is exploiting molecular self-assembly as a bottom-up fabrication strategy. Whitesides defined the term self-assembly as the spontaneous association of molecules under equilibrium conditions into stable, structurally well-defined aggregates joined by non-covalent bonds.^[17] This brief definition already comprises the strengths but also the challenges that have to be faced. In particular the term "non-covalent" emphasizes these two aspects. The reversible nature of non-covalent (=weak) interactions gives rise to the emergence of highly ordered structures. As stated before, control over spatial arrangement is of utmost importance since molecular interconnection eventually determines any kind of functionality. Additionally, in contrast to impressive experiments where single molecules are deliberately arranged by scanning probe tech-

niques,^[18-21] self-assembly is a parallel process and therefore a fast route for synthesis. However, the major drawback of self-assembly lies in the weakness of non-covalent bonds, resulting in inferior mechanical stability, but above all, weak interactions cannot mediate electronic coupling between molecules. In the recent years a lot of research activities aimed at strengthening intermolecular bonds, while maintaining the structural order of resulting assemblies. In particular synthesis of long range ordered molecular networks based on metal-coordination bonds^[22,23] or covalent bonds^[24-26] can meet the desired properties in an adequate way. Roughly speaking, bond strength is negatively correlated to bond reversibility. As a consequence, molecular networks with strong intermolecular bonds exhibit a high defect density. A defect-free covalently bound network could for instance not yet be realized in a bottom-up approach. Studies of molecules adsorbed on surfaces are hence not only important from a fundamental point of view, but probing and understanding physical and chemical properties of molecules and assemblies of molecules are rather a prerequisite for further use in devices. Among various surface sensitive experimental techniques, Scanning Tunneling Microscopy (STM) has been established as leading method to gain fundamental insights into molecular adsorption on crystal surfaces and on-surface reactions. The topics covered in this work include molecular self-assembly of hydrogen bonded networks and synthesis of molecular assemblies stabilized by metal-coordination or covalent bonds with particular emphasis on interactions of organic molecules with metal substrates. The outline of the thesis is as follows: Chapter 2 introduces the experimental method, the Scanning Tunneling Microscope (STM) and its basic theory. Besides, a brief overview of the ultrahigh vacuum (UHV) chamber is given, where the majority of experiments was conducted. Chapter 3 and 4 describe the complex interactions that can occur in adsorbate-substrate systems. Firstly, in chapter 3 various types of intermolecular bonds present in the investigated supramolecular entities are discussed. Weak non-covalent bonds, but also strong interactions as metal-coordination bonds and covalent bonds are treated. Chapter 4 outlines some concepts of molecule-substrate interactions which aim at understanding phenomena as self-assembly, diffusion, or reactivity. A conclusion is given in chapter 5, followed by the articles published in the framework of this thesis.

2 Experimental Methods

This chapter focuses on the main experimental method of the thesis, Scanning Tunneling Microscopy (STM). After an introduction to STM and its impact on surface- and nano-science, its basic theory is outlined. Difficulties arising in the interpretation of STM images of adsorbates are briefly discussed. In the last part, the ultrahigh vacuum (UHV) system, where most of the experiments were conducted, is described. Modifications to enhance the STM performance as well as a home-built electron beam tip heating device are presented.

2.1 Introduction

For this thesis mainly STM experiments were performed, partly under ambient conditions at the liquid-solid interface, but mostly under UHV conditions. Moreover, further analytical surface science tools as low energy electron diffraction (LEED) or mass spectrometry with the possibility for temperature programmed desorption (TPD) were available, but will not be treated here. Since its invention in 1982 the STM has been established as an essential tool in surface science. Although inherently limited to studies of electrically conductive samples, a variety of STMs have been developed working in different environments - from ultrahigh vacuum to ambient conditions, in liquids,^[27,28] at low temperatures,^[29] or at high pressures.^[30,31] Of course, the scope of the study determines the experimental conditions. For single molecule spectroscopy for instance, ultrahigh vacuum and very low temperatures (realized by liquid helium cooling) are necessary, whereas for studies of extended periodic molecular network structures room temperature conditions might be sufficient. The topics treated in this thesis can be subdivided into two parts: molecular self-assembly at the liquid-solid interface and UHV studies of extended molecular networks stabilized by coordinative and covalent bonds. In the first part self-assembly properties of hydrogen bonded systems at the graphite-liquid interface were studied. By choosing appropriate molecular building blocks, engineering of tailored nanostructures was possible. The latter studies aimed at understanding how different metal surfaces interact with organic molecules to eventually induce chemical reactions leading to covalently linked molecular nanostructures.

2.2 Scanning Tunneling Microscopy

2.2.1 Basic Principle

STM is based on the quantum mechanical tunneling effect. This microscopic technique is capable of producing real space images of conductive surfaces with atomic resolution. An example of an atomically resolved Cu(111) surface is shown in figure 2.1. The probability of electrons tunneling through a classically forbidden barrier depends roughly exponentially on the barrier width, which will be treated in detail later in this section. This property gives rise to extreme sensitivity and the ability to distinguish single atoms.

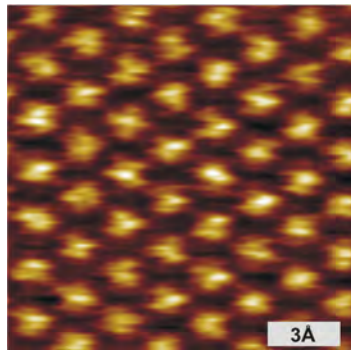


Figure 2.1: Atomically resolved STM image of a Cu(111) surface. The image was taken at room temperature. $I_T = 199$ pA, $U_T = 158$ mV

The final development of the STM in 1981 was preceded by two technological achievements, the topografiner by Young et al. in 1972^[32] and the electron tunneling experiments by Teague in his PhD thesis in 1978.^[33] The topografiner - in a way the first scanning probe microscope - is an instrument where a field emission current between a tip and the sample was employed to image a surface. A piezoelectric driver was used to scan a surface with a tip-sample distance of about 100 nm. By applying a positive voltage of a few kilovolts to the sample, a lateral resolution of roughly 400 nm could be achieved. Teague could demonstrate vacuum tunneling between two gold electrodes at voltages and tunneling gap widths comparable to STM tunneling conditions.^[34] For the STM, Binnig and Rohrer combined these two developments.^[35] The basic operation principle is shown in figure 2.2. An atomically sharp metallic tip is brought close to a surface at a distance of less than one nanometer. When a small voltage of about 1 V is applied to the surface or the tip, electrons can tunnel through the gap either from sample to tip or vice versa, depending on bias voltage polarity. Using a piezo-electric tube, the tip can now be raster-scanned over an area of interest, and images with the contrast based on spatial variations of the tunneling current can be created. Typically 512×512 measurements in a regular array are taken to generate one image. Nominally, there are two modes of operation in STM. In the *constant-current mode* an electronic feedback loop controls the vertical position of the tip in such a way that the current remains at a constant preset value. The

image is generated by recording the vertical position of the tip as a function of lateral coordinates. In the *constant-height mode* the vertical position of the tip, i.e. average tip-sample distance, is constant. A low cut-off frequency of the feedback loop still allows for spatial modulation of the tunneling current but avoids tip crashes. The current recorded as a function of the lateral position represents the image. Generally, the constant-current mode yields more reliable information about topographic height, whereas the constant-height mode allows for higher scanning frequencies. A new microscope was developed recently by Frenken and coworkers^[36] capable to operate at video rates and beyond (200 frames/s), which will open new perspectives in the study of dynamic processes.

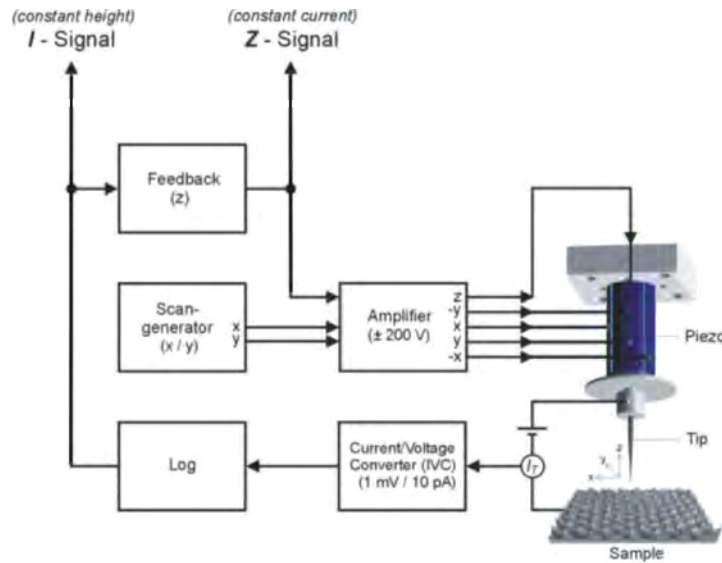


Figure 2.2: Operation principle of a computer-controlled STM. The tip motion is realized by piezo-electric actuators. See text for details. Figure adapted from Trixler.^[37]

2.2.2 Theoretical Description

An exact treatment of the tunneling process in STM is virtually impossible, since this would require a detailed description of electronic sample and tip states and their evanescence into the tunneling gap. Especially, describing the tip is impossible due to its unknown geometry on the atomic level. Besides, its apex structure can frequently change even during an experiment. Nevertheless, models at different levels of approximation have been developed and will be presented in the following. An overview of existing theories can be found e.g. in Chen's textbook^[38] or the review article by Drakova.^[39]

An elementary model

The treatment of the tunneling process in one dimension serves as an introduction to

the concept of STM imaging.^[38] Considering a constant potential barrier with barrier height U in the region $0 < z < d$, as illustrated in figure 2.3, the wavefunction $\Psi(z)$ of an electron with an energy $E < U$ moving in $+z$ direction in the forbidden region can be approximated by

$$\Psi(z) = \Psi(0)e^{-\kappa z} \quad (2.1)$$

where $\kappa = \sqrt{2m(U - E)}/\hbar$ with m being the electron mass and \hbar Planck's constant. The probability of observing an electron at $z = d$ is hence proportional to $|\Psi(d)|^2 = |\Psi(0)|^2 \exp(-2\kappa d)$ which means that there is a non-zero probability for electrons to overcome the barrier. Now some basic features of a metal-vacuum-metal junction can be considered with sample states Ψ_n and work function Φ . For simplicity the work functions Φ of the two metals (representing tip and sample) are assumed to be equal. By applying a bias voltage V , a net tunneling current can flow. For small bias voltages, i.e. $eV \ll \Phi$, the probability for an electron in the n^{th} sample state with energy E_n between the Fermi level E_F and $E_F - eV$ is according to equation 2.1 proportional to $|\Psi_n(d)|^2 = |\Psi(0)|^2 \exp(-2\sqrt{2m\Phi}d/\hbar)$. Since the tunneling current is proportional to the sum over all states within the energy interval eV it can be stated that

$$I \propto \sum_{E_n=E_F-eV}^{E_F} |\Psi_n(d)|^2. \quad (2.2)$$

For small V , the electronic *density of states* (DOS) does not vary significantly within the energy interval $[E_F - eV, E_F]$ and the sum in equation 2.2 can be expressed in terms of the *local density of states* (LDOS)* $\rho_s(z = d, E_F)$ of the sample at the Fermi level and the tip position $z = d$, which for sufficiently small energies close to the Fermi edge is defined as

$$\rho_s(z, E_F) \equiv \frac{1}{eV} \sum_{E_n=E_F-eV}^{E_F} |\Psi_n(z)|^2. \quad (2.3)$$

Accordingly equation 2.2 reads

$$I \propto V \rho_s(z = d, E_F) = V \rho_s(z = 0, E_F) e^{-\frac{2}{\hbar} \sqrt{2m\Phi}d} \quad (2.4)$$

which basically states that a constant-current STM image is a contour map of the sample LDOS at the Fermi energy. Taking into account typical work functions of $\Phi \approx 5$ eV, the decay constant has a value of approximately 2.3 \AA^{-1} . This means that the tunneling current increases by about one order of magnitude when the tip-sample distance is decreased by 1 \AA .

Bardeen's approach

In 1961, long before the invention of the STM, Bardeen found a method based on perturbation theory to calculate the tunneling current between two planar metal plates

*The *density of states* (DOS) is generally defined as the sum over all states i with energy E : $\rho(E) = \sum_i \delta(E_i - E)$, whereas the *local density of states* (LDOS) is further more weighted by the square of the wavefunction Ψ_i at a certain point in space, yielding an additional spatial dependency: $\rho(E, \vec{r}) = \sum_i \delta(E_i - E) |\langle \Psi_i(\vec{r}) \rangle|^2$.

in the context of metal-insulator-metal junctions. Instead of solving the Schrödinger equation for the whole system, Bardeen considered two separate subsystems. He ob-

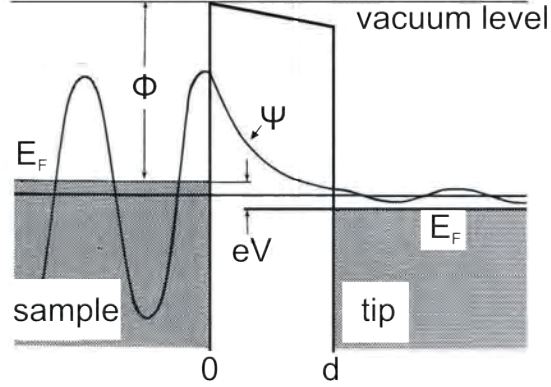


Figure 2.3: Schematic energy diagram for the sample-tip tunneling junction with a width d . A positive bias voltage is applied to the tip, i.e. tunneling occurs from occupied sample states to unoccupied tip states. Tunneling is only possible in the energy interval eV . Ψ represents a wavefunction that decays exponentially inside the barrier region and has a non-zero probability in the tip region. Figure adapted from Chen.^[38]

tained the individual electronic wavefunctions by solving their stationary Schrödinger equations and calculated the electron transfer by using first-order time-dependent perturbation theory. The formula which is commonly used to describe electron transitions within perturbation theory is Fermi's golden rule. It states that the transition rate, i.e. the probability p of a transition from a sample state Ψ_s into tip state Ψ_t , is obtained by

$$p = \frac{2\pi}{\hbar} |M_{st}|^2 \delta(E_{\Psi_s} - E_{\Psi_t}) \quad (2.5)$$

if only elastic tunneling is considered, i.e. only tunneling between states with similar energy E_{Ψ_s} and E_{Ψ_t} . The tunneling matrix element M_{st} describes the amplitude of electron transfer. It is determined by the overlap of the wavefunctions of the two subsystems at a more or less arbitrary separation surface S_0 , that separates the two electrodes as follows:

$$M_{st} = \frac{\hbar^2}{2m} \int_{S_0} (\Psi_s^* \nabla \Psi_t - \Psi_t^* \nabla \Psi_s) dS. \quad (2.6)$$

When a bias voltage is applied, the tunneling current is given by integrating over all possible combinations of sample and tip states

$$I = \frac{2\pi e}{\hbar} \int_{-\infty}^{\infty} [f(E_F - eV) - f(E)] \rho_s(E - eV) \rho_t(E) |M_{st}|^2 dE. \quad (2.7)$$

Here $f(E) = [1 + \exp((E - E_F)/k_B T)]^{-1}$ is the Fermi distribution at temperature T which considers thermal excitations of electrons; ρ_s and ρ_t are the densities of states of the two electrodes. For not too high temperatures the Fermi distribution can be approximated as a step function and equation 2.7 simplifies to

$$I = \frac{2\pi e}{\hbar} \int_{E_F}^{E_F + eV} \rho_s(E - eV) \rho_t(E) |M_{st}|^2 dE. \quad (2.8)$$

Provided that the tunneling matrix element does not change much in the energy interval eV , the tunneling current is determined by the convolution of the density of states of the two electrodes. Commonly, the tip DOS is assumed constant, so the measured current scales with the DOS of the sample.

Tersoff-Hamann's s-wave approximation

Using Bardeen's formalism, Tersoff and Hamann approximated the tip as an object with spherical symmetry and radius R ^[40,41] in order to evaluate the tunneling matrix element M_{st} in equation 2.8. By considering only tip states with s-symmetry, the solution for the tunneling matrix element in equation 2.6 yields

$$M \propto \kappa R e^{\kappa R} \Psi_s(r_0) \quad (2.9)$$

where $\kappa = \sqrt{2m\Phi}/\hbar$ is the minimum inverse decay length for the wavefunctions into the vacuum gap with an effective local barrier height Φ . $\Psi_s(r_0)$ is the sample wavefunction evaluated at the center r_0 of the tip. With all these assumptions made so far^[34] the result for small bias voltages is

$$I \propto V \frac{R^2}{\kappa^4} e^{2\kappa R} \rho_t(E_F) \rho_s(E_F, r_0) e^{\kappa R} \Psi_s(r_0) \quad (2.10)$$

which means that the tunneling current is proportional to the sample density of states ρ_s at the Fermi level and at the center of the tip apex. Similar to the result obtained in the elementary one-dimensional model, the exponential dependence on the gap distance is again reproduced due to the exponential decay of the sample wavefunctions into the vacuum gap. Tersoff and Hamann relate the tunneling current only to the spatial variations of the sample LDOS at the Fermi level.

However, Tersoff and Hamann's model is grounded on several approximations that have to be considered when interpreting STM data:^[34] Tip and sample are treated separately, i.e. mutual interactions are neglected which means that the model only holds for large tip-sample distances. Moreover, by approximating the tip with s-wavefunctions, no tip dependent imaging characteristics can be obtained.

2.2.3 Imaging Molecules

STM studies of adsorbed molecules provide access to their chemistry and physics, since the contrast in STM topographs is a direct result of interactions between molecules

and substrate and in between molecules. The direction of the tunneling current determines whether electrons tunnel into occupied or unoccupied molecular states. So-called dI/dV maps probe for instance the LDOS at a fixed energy level and allow thus for mapping orbital structures.^[42] However, first occupied and unoccupied orbitals are generally not comparable to HOMO and LUMO of isolated molecules, since interactions with the substrate lead to complex perturbations and hybridization effects. Only for molecules electronically decoupled from the substrate^[43] (which can be realized e.g. by two layers of sodium chloride grown on a metal substrate^[44]) a comparison with unperturbed orbitals is valid.^[45] Deeper insights into the various types of interactions will be given in chapters 3 and 4. The first STM images of organic adsorbates date back to 1987. Gimezewski *et al.* reported on copper phthalocyanine on polycrystalline silver surfaces^[46] and in the same year Smith *et al.* imaged lipid bilayers^[47] and sorbic acid.^[48] Generally speaking a simple interpretation based on the topological height is rather unsatisfying. Also identifying the chemical nature of an adsorbed species by its apparent height with respect to the surface is not possible. The reason is that according to Tersoff and Hamann's results the tunneling current scales with the LDOS at the Fermi energy. Some examples for counterintuitive STM image contrasts are for instance the systems Br/Cu(111)^[49] or O/Pt(111),^[50] where the adsorbates appear as depressions in the topography data. The pioneering work tackling the problem of contrast mechanism was carried out by Lang.^[51,52] Making use of the perturbation approach, he showed for atomic adsorbates that they are imaged either as protrusions or depressions depending on whether the LDOS at the Fermi level is increased or depleted. STM image simulation relies for many methods on perturbation theory, following Bardeen and Tersoff and Hamann. Another very popular method, which is a non-perturbative approach, is the electron scattering quantum chemical (ESCQ) method developed by Sautet and Joachim.^[53] Therein the tunneling process is described as a scattering problem. The tunneling gap is treated as a two-dimensional defect located in between two semi-infinite electrodes. The tunnel event is then regarded as a scattering process, i.e. incoming electrons scatter from the tunneling junction having a small probability to penetrate the gap and a large one to be scattered back. A famous example of a successful application of this theory is the adsorption of benzene on Pt(111) where different adsorption sites could - in agreement with experimental data - be discerned.^[54,55] An overview of various theoretical methods to simulate STM images of adsorbates is given in a review by Sautet.^[56]

2.3 UHV System

2.3.1 Overview

A major part of the experiments in this thesis was conducted in two different UHV chambers, one equipped with a VT STM by *Omicron NanoTechnology* and the other one with a home-built beetle-type STM. For the liquid-solid experiments a home-built ambient conditions STM was used. Here, only the chamber housing the Omicron VT STM is shortly presented.

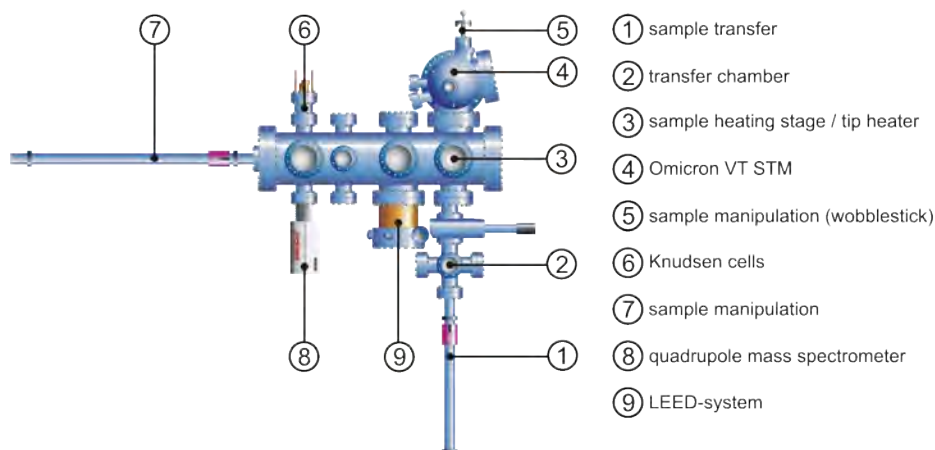


Figure 2.4: Sketch of the UHV chamber and its components

The UHV-system consists of a main chamber housing all analytics, preparation and deposition facilities, and a transfer chamber. A schematic overview with all components described below is given in figure 2.4. A separately pumped transfer chamber allows for easy transfer of samples and tips into the main chamber without breaking the vacuum. Main and transfer chamber can be pumped independently by turbomolecular pumps backed by oil-free forepumps. Additional pumping is provided by an ion getter pump and a titanium sublimation pump. The resulting base pressure after bakeout is below 5×10^{-10} mbar. During STM measurements turbomolecular pumps and forepumps are turned off for mechanical noise reduction. For sample preparation standard components as a sample heating stage and an argon ion sputter gun are available. Various molecular evaporators are attached to the chamber working with resistive heating of a tungsten filament.^[57] For TPD experiments a quadrupole mass spectrometer is available. It was mainly used for leak detection, analysis of residual gas, or to determine optimal sublimation temperatures of organic evaporants. Besides, the main instrument, the Omicron VT STM, the chamber is also equipped with a Spot Profile Analysis LEED system (SPA-LEED).

2.3.2 Modifications of the Omicron VT STM

The STM in the main chamber is an Omicron VT STM which in its original design can operate at variable temperatures (between 25 K and even at elevated temperatures). For vibrational isolation the microscope is suspended on four springs with a vertical resonance frequency of about 2 Hz. In addition an eddy-current damping is implemented. Coarse positioning is based on the stick-slip principle and allows for automated coarse approach of the tip, whereas for scanning a piezo tube with a maximum lateral scan range of 12 μm and a maximum vertical scan range of 1.5 μm is utilized. A view into the scanning unit is shown in figure 2.5.

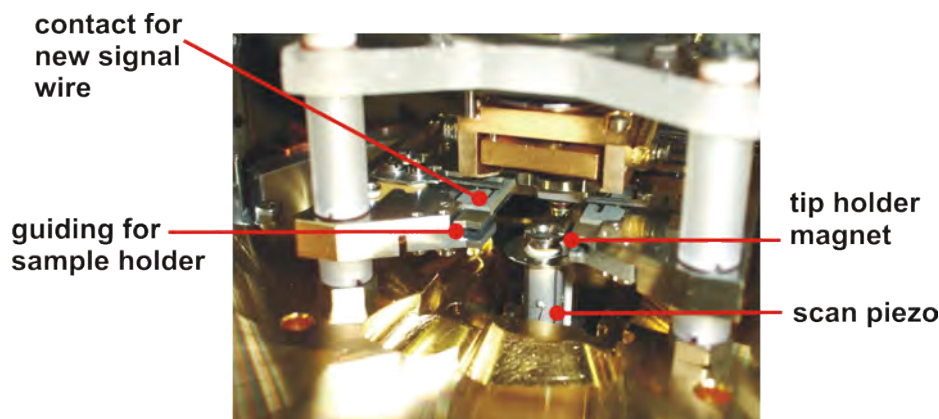


Figure 2.5: View into the scanning unit of the Omicron VT STM

One of the main difficulties in STM is the fact that very small currents (in modern STMs even below 1 pA) have to be handled. A preamplifier or more precisely a transducer that converts the current into a (electronically easier to handle) voltage is usually utilized. The signal carrying wire therefore has to be carefully shielded and reduced to minimum length in order to minimize noise pick-up. In the original Omicron design two stages of amplification were present - the first stage mounted very close to the STM, and a second stage located at the atmospheric side. The signal was passed inside the tube piezo by a coaxial wire. A drawback of this setup is the vicinity of the wire carrying the unamplified signal to the piezo electrodes which resulted in unwanted cross-talk. Especially imaging rough surfaces was difficult since abrupt changes in the z-position always caused disturbances in the tunneling signal. In order to circumvent this problem the design was changed. The signal wire was attached to the sample instead of the tip, and a one-stage preamplifier (*Femto LCA-2K-2G*) with a bandwidth of 2 kHz and a feedback resistance of 2 G Ω replaced the two stages of the original design. Although the distance from sample to preamplifier is larger in the new design, a considerably better signal-to-noise ratio could be established.

2.3.3 Electron Beam Tip Heater

A crucial issue in STM in general is the fabrication and post-processing of scanning probe tips. For the UHV studies in this work electrochemically etched polycrystalline tungsten tips were utilized. In addition, the tips were dipped into a 40 % aqueous solution of hydrofluoric acid before introducing into the STM chamber. In order to further improve their performance, it is indispensable to remove a remaining oxide layer that still coats the tips after transfer into the vacuum chamber, and to remove organics collected by the tip during experiments. Various approaches have been discussed in literature, mostly high-temperature annealing,^[58] possibly in combination with ion sputtering.^[59,60] Whereas for single crystalline tips faceting due to enhanced diffusion and a subsequent sharpening of the tip is intended,^[58] the tip heater developed within this thesis serves mainly to remove oxide layers and organic contaminations. It

is compatible with standard Omicron tip holders. A schematic sketch of the principle is depicted in figure 2.6.

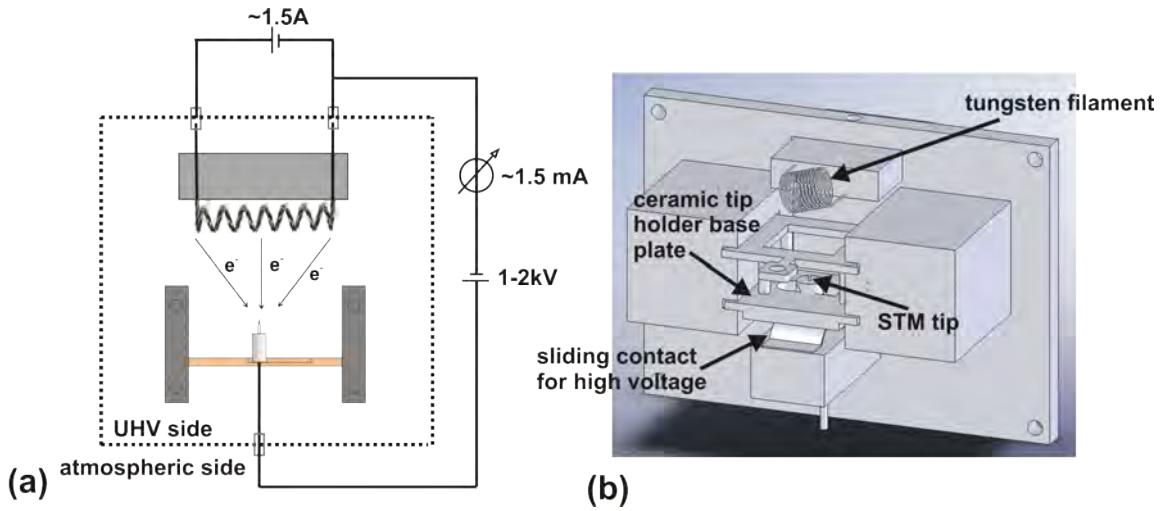


Figure 2.6: (a) Scheme of the electron beam tip heater. Electrons are emitted from a hot filament and accelerated towards the tip. (b) 3D model of the tip heater

A looped tungsten filament which is taken from a commercial 20 W halogen light bulb, driven with about 1.5 A, is placed some 5 mm above the STM tip. The tip - electrically isolated from the Omicron tip holder due to a custom made ceramic base plate (macor) - is contacted from below by a sliding contact, where a high voltage of +1.5 kV...+2 kV is applied. Electrons are then thermally emitted from the hot filament and accelerated towards the tip resulting in a current of roughly 1.2 mA - 2.0 mA. The sharp geometry of the tip gives rise to high electric fields, and thus high current densities at the tip. This leads to a local heating and high temperatures at the tip apex, required to remove the oxide layer.

3 Molecule-Molecule Interactions

Synthesis of ordered two-dimensional networks of organic molecules has drawn a lot of attention over the last decades. Possible applications in the fields of template structures for host-guest chemistry, sensors, or molecular electronics have been discussed extensively. The crucial issue in this context is the apparent mutual exclusion between strong intermolecular bonds and long-range ordering. Generally speaking, strong bonds tend to be irreversible under common experimental conditions and lead to networks with high defect densities. On the other hand, strong intermolecular bonds facilitate superior mechanical, chemical, and thermal stability, as well as functionality as for instance electrical conductivity. Networks based on relatively weak bonds, like hydrogen bonds exhibit a high degree of crystallinity, but lack stability. This chapter deals with the different intermolecular bonds that have been studied within this thesis. Starting with the weakest types, hydrogen bonds and halogen-halogen interactions, metal coordination bonds, and finally covalent bonds are discussed and illustrated with results of this thesis.

3.1 Non-Covalent Bonds

Hydrogen Bonds

Hydrogen bonds are of utmost importance in nature. For instance proteins or DNA obtain their three-dimensional structure amongst other interactions from hydrogen bonds. They are also responsible for intermolecular bonds between water molecules, and thus for the unique properties of water. Hydrogen bonding is a donor-acceptor interaction involving hydrogen atoms. They are formed when the electronegativity (as defined by Pauling in 1939) of an atom A relative to hydrogen in an A-H covalent bond withdraws electrons from hydrogen resulting in a partial positive charge at the H atom. The hydrogen bond acceptor B must have lone-pair electrons or polarizable π electrons to interact with the donor A-H.^[61] The notation is then A-H \cdots B. It is nowadays well established that hydrogen bonding can neither exclusively be described by electrostatic theory nor by covalent bonding, but involves a rather complicated superposition of individual contributions, i.e. electrostatic energy, exchange repulsion, polarization energy, covalent bonding and dispersion forces.^[62-64] Typical H-bond energies are in the range of 2 kJ/mol to 20 kJ/mol, which renders them reversible at room temperature and hence makes them suitable mediators for synthesizing long-range ordered 2D structures on surfaces.^[65] The angular dependence of the binding energy for two-center hydrogen bonds has a minimum at a bond angle of 180°, i.e. a

linear arrangement is energetically favored. However, for weak hydrogen bonds this potential curve is not very steep which means the bond angle can easily be bent,^[61] which renders hydrogen bonds versatile and topologically flexible interconnects for supramolecular architectures.^[66]

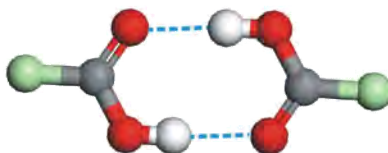


Figure 3.1: Scheme of the double H-bond interconnecting two carboxylic groups (oxygen: red, hydrogen: white, organic remainder: green).

In this thesis surface mediated self-assembly of carboxylic acids into ordered structures has been studied at the liquid-solid interface. Carboxylic groups are interesting functional units for several reasons. They can act both as donor (via the carbonyl oxygen atom) and acceptor (via the hydroxyl group)^[67] as schematically sketched in figure 3.1. Another striking feature of the double hydrogen bond is the occurrence of resonance-assisted hydrogen bonding (RAHB).^[68–70] The concept of resonance is well known in *molecular orbital theory*. It leads to the fact that the total energy of multiple bonds is larger than the sum of the individual components, as it is the case for the aromatic bonds in benzene for instance. Similarly, also for the double hydrogen bond between carboxylic groups, or more generally in cyclic hydrogen bond patterns, this resonance in the π electron system can strengthen the bond considerably by increasing the positive charge at the proton and the negative charge at the carbonyl oxygen atom.^[71]

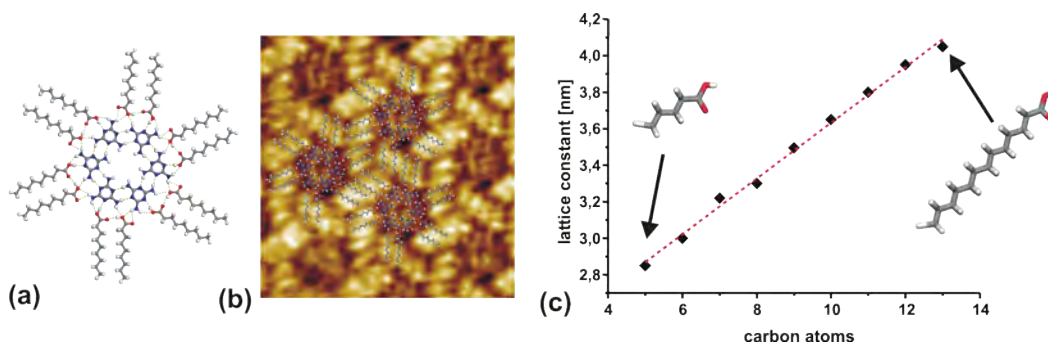


Figure 3.2: (a) Molecular model of the basic unit consisting of a melamine hexamer and 12 radially arranged fatty acid molecules. (b) STM topograph of melamine with nonanoic acid with overlaid molecular model. (c) Experimentally determined dependency of the lattice parameter on the length of the fatty acid spacer.

Hydrogen bonds also play a crucial role in many self-assembled systems, partially because they are the strongest, and hence dominant interactions. Concerning hydrogen bond assisted self-assembly, the formation of bimolecular isotopological monolayers comprised of melamine and members of the homologous series of fatty acids (extending from pentanoic through tridecanoic) has been investigated in a liquid-solid interface STM study (see manuscript 6.1). Melamine is a heterocyclic aromatic molecule and consists of a triazine ring endowed with three amine groups at the 2, 4, and 6 positions. The molecule is well functionalized to interact with carboxylic groups: amine groups can act as proton donors whereas the nitrogen atoms in the triazine ring can be proton acceptors through their lone pair electrons. In these systems the carboxylic acids not only serve as solvents, i.e., provider and transport medium for solute molecules, but are also a structure determining part of the self-assembled monolayers. For all solvents, hexagonal structures were observed where the lattice parameter increases linearly with the chain length of the fatty acid from 2.8 nm for pentanoic acid to 4.1 nm for tridecanoic acid. An STM topograph for the system melamine and nonanoic acid on graphite is shown in figure 3.2. As the corresponding molecular model and the linear dependence illustrate, all bimolecular networks exhibit the same topology: the basic unit consists of a melamine hexamer which is stabilized by internal $N \cdots H-N$ hydrogen bonds and surrounded by 12 radially arranged fatty acid molecules interaction via van-der-Waals forces. The length of the interconnects, i.e. the fatty acids makes it now possible to tune the lattice parameter of the system.

Halogen-halogen interactions

Another example of rather weak intermolecular forces are halogen-halogen interactions. It is well known that halogen molecules or alkyl and aryl halides form complexes with atoms containing lone pairs of electrons,^[72,73] which makes the halogen site in principle behave like a Lewis acid. Very similar to hydrogen bonding halogenated molecules can interact with an electron rich site resulting in a donor/acceptor relationship. However, an attractive force between two similar halogens is also present; the hydrogen analogue is referred to as dihydrogen bonds.^[74] The chlorine-chlorine interactions have for instance been recognized and exploited in the seminal studies of photodimerization initiated by Schmidt and coworkers several decades ago.^[75] Desiraju has argued that the halogen-halogen interaction in organic compounds is an attractive force, and hence of special interest in the field of supramolecular chemistry and crystal engineering.^[65] The origin is electrostatic and attributed to a non-spherical atomic charge distribution in halogen substituents as the simulation of iodobenzene by Bosch and coworkers^[75] illustrates in figure 3.3(a). The calculations of the electrostatic potential at the halogen atoms show a positive potential cap opposite to the C-Br bond and a ring of negative potential around the bond axis. Accordingly a cyclic intermolecular arrangement, as shown in Figure 3.3(b) for the molecule 1,3,5-tris(4-bromophenyl)benzene (**TBB**), is a favorable binding motif. This interaction is described in literature as a Coulombic donor-acceptor attraction.^[75,76] Not surprisingly, interaction strength varies depending on the organic remainder to which the halogen atom is bound to. For a carbon-halogen bond the chemical environment of the respective carbon atom

influences the electrostatic potential. For instance different types of hybridization of the carbon atom influence the halogen-halogen interaction strength following the order $sp^2 > sp > sp^3$.^[77]

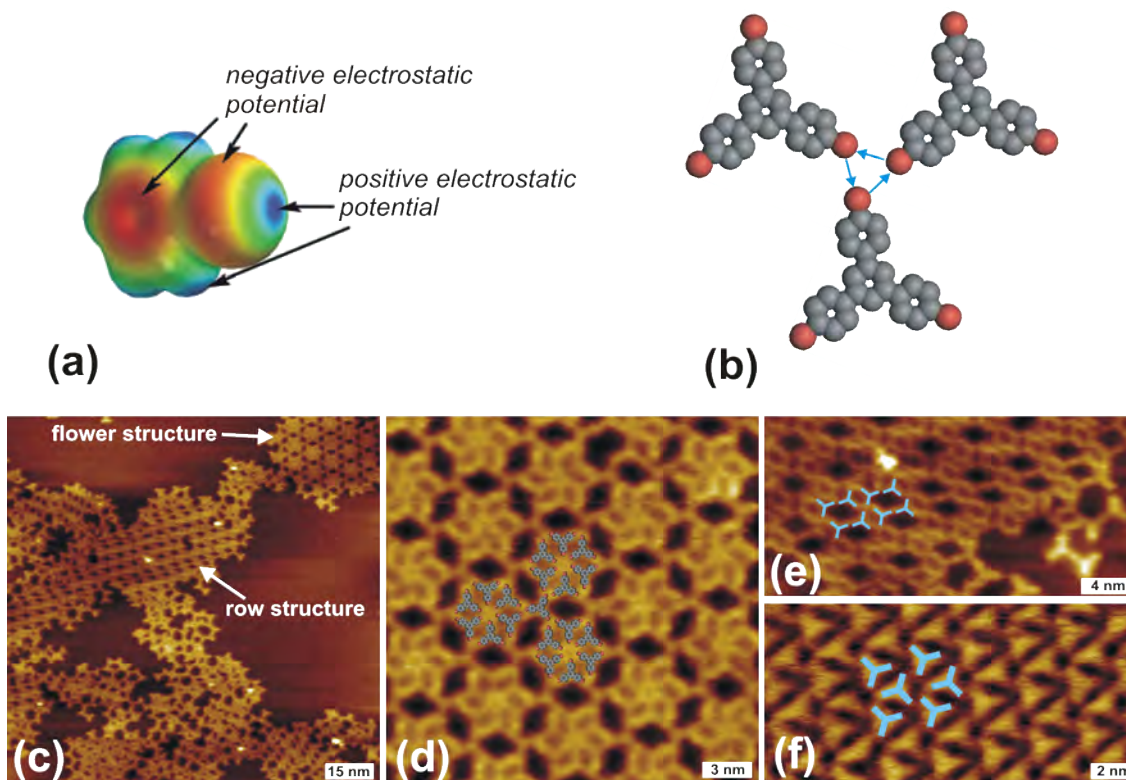


Figure 3.3: (a) Non-spherical charge distribution of iodobenzene.^[75] (b) Triangular interaction motif of TBB molecules. The versatility of halogen-halogen bonds is illustrated in STM topographs of various structures of TBB on Ag(111). (c) Overview image presenting two coexisting ordered phases, namely, a row structure on the upper center part and a hexagonal flower structure in the upper right part. The lower half depicts a disordered phase. (d) Close-up of the flower structure with overlaid molecular model (e),(f) Two oblique phases based on displaced dimers as basic building blocks.

A systematic study of TBB self-assembly in UHV on the rather unreactive substrate Ag(111) underlines the weakness and the low directionality of the bromine-bromine bonds. In a series of experiments the molecules were evaporated onto the substrate at room temperature ensuring sufficient lateral diffusivity, a primary requirement for self-assembly. In contrast to more reactive metal substrates, where C-Br bond cleavage has been observed (which will be discussed in detail later), here, various binding motifs are observed, as the STM topographs in figure 3.3(c)-(f) illustrate. The hexagonal structure in figure 3.3(d) contains six-membered rings of cyclic halogen bonds. Three of those supramolecular hexamers are interconnected via single TBB molecules in a triple Br-Br-Br bond pattern as schematically depicted in figure 3.3(b). Also a slightly

displaced head-to-head geometry enables favorable electrostatic interactions and gives rise to two other polymorphs, a row structure (figure 3.3(e)) and a densely packed structure (figure 3.3(f)). The experimentally observed coexistence of several different polymorphic structures indicates the relative weakness and topological versatility of halogen-halogen interactions.

3.2 Metal-Coordination Bonds

Metal-organic coordination bonds represent a compromise between bond strength and bond reversibility. Generally speaking, a coordination system consists of a coordinating metal atom (or cluster of atoms) with one or more electron rich ligands attached to it. Various examples of metal-organic frameworks (MOFs) with a high degree of order in one, two, and three dimensions exist in literature.^[78-80] The binding energies are relatively strong, ranging between 50 kJ/mol and 200 kJ/mol.^[22] Prominent 3D examples are the isoreticular metal-organic frameworks (IR-MOF) discovered and characterized by Yaghi and coworkers.^[81] These porous structures are considered to be very promising candidates for gas storage applications. Further application of 3D MOFs is for instance conceivable in the field of photovoltaics.^[82] Also a variety of surface-supported molecular architectures from organic molecules and (mostly) transition metal centers have recently been investigated.^[6,83-87] The bonding mechanism is discussed controversially in literature,^[88] but it is by now well established that the coordination bond has both ionic and covalent contributions.^[89] Various theories, which were favored at different times, have been developed - mostly only being able to describe certain aspects of the bond. *Ligand field theory* for instance describes very well spectroscopic properties. Based on *molecular orbital theory* formation of a coordination compound can be described by the following sequence:^[88]

- Removal of electrons from the metal center (i.e. oxidation) in order to provide a cation
- Hybridization of the metal atomic orbitals which provide a set of equivalent hybrid orbitals directed towards the ligands
- If necessary, rearrangement of the metal electrons to ensure that the hybrid orbitals are unoccupied
- Formation of covalent σ -bonds between metal center and ligand by the overlap of metal hybrid orbitals with ligand orbitals containing lone-pair electrons

Hence, the formation of metal-coordination networks is mostly determined by the coordination geometry of the metal center which for transition metals depends on the d-orbital occupation. Under 2D conditions, however, the presence of a metal substrate makes it difficult to predict coordination geometries in comparison to a known 3D analogue. Whereas in 3D the element determines the geometry, in 2D "unusual" motifs can occur. Such deviations can be attributed to charge transfer or substrate

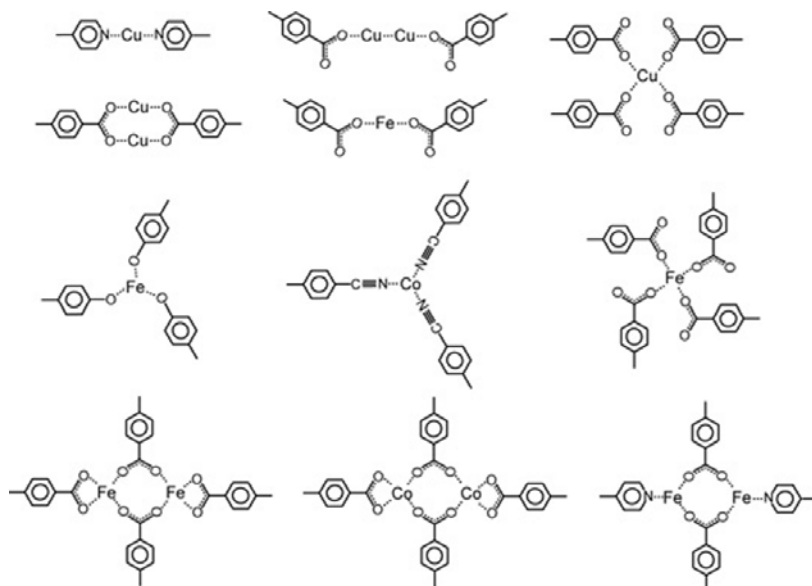


Figure 3.4: Different coordination motifs with coordinating Cu, Co and Fe centers, and various organic groups explored in surface-confined metal-ligand systems.^[23]

screening effects^[83] that severely affect the metal-to-ligand bonding within a 2D network. Some examples of observed coordination geometries in surface supported MOFs are depicted in figure 3.4.

In order to explore novel interlinking chemistry 2D MOFs based on thiolate-copper coordination bonds have successfully been synthesized as a part of this thesis. Due to the pronounced covalent π character of the copper-thiolate bond,^[89] and the high degree of ordering achieved, these types of MOFs are expected to be electronically conjugated, and hence interesting for applications. The organic molecule, 1,3,5-tris(4-mercaptophenyl)benzene (**TMB**) has a similar aromatic backbone as TBB, only the halogen atoms are substituted by thiol groups. Again, the educt molecules were evaporated under UHV conditions onto a clean Cu(111) surface at room temperature resulting in a self-assembled close packed trigonal structure. In accordance with previous studies, the thiol molecules were expected to deprotonate especially on a reactive surface as copper^[90,91] and subsequently form a chemical bond to the substrate.^[92–95] Deprotonated thiols are referred to as thiolates. Thermal annealing at 160°C - 200°C for about 10 minutes converted the initial structure into two morphologically different metal-organic frameworks, a honeycomb and a dimer-row structure. STM images and the corresponding molecular models are shown in figure 3.5. Two effects are responsible for the formation of metal-coordination networks: enhanced lateral mobility of molecules and sufficient supply of copper adatoms, i.e. highly mobile adsorbed atoms, arising from evaporation at atomic step edges (The issue of adatoms will be discussed in more detail in 4.4). Since the initial coverage was always in the submonolayer regime, enhanced diffusion could result in the formation of thermodynamically more stable, but less densely packed structures, with stronger intermolecular bonds, i.e. copper-thiolate bonds. A drastic increase of the 2D adatom concentration in the

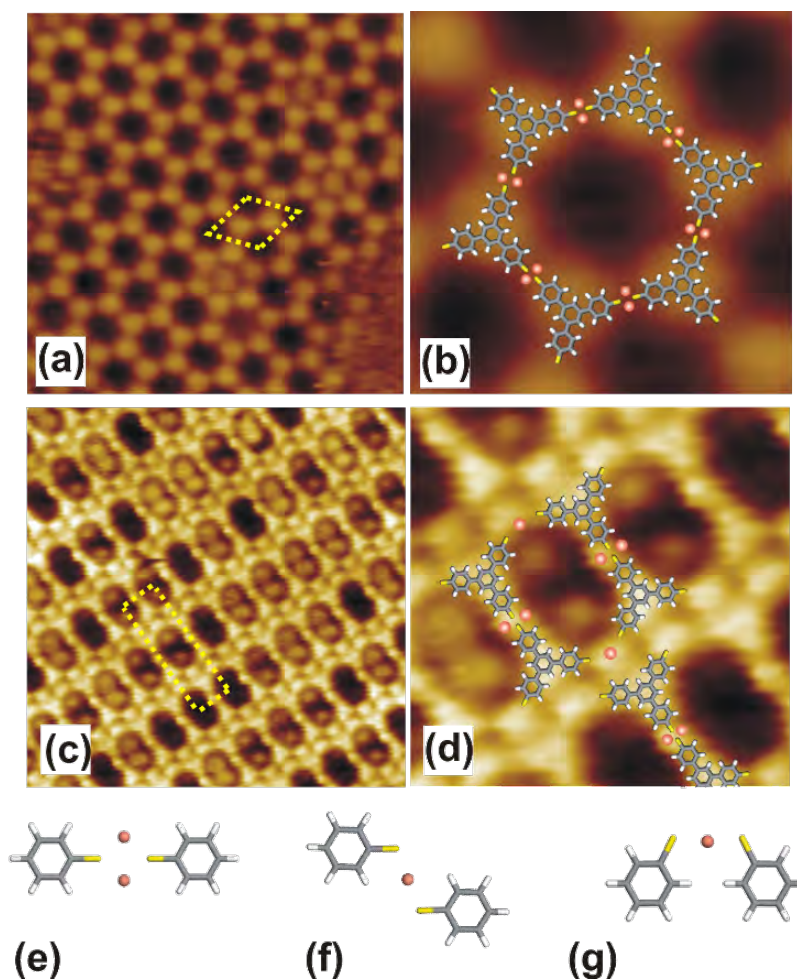


Figure 3.5: (a) STM topograph of honeycomb structure with unit cell indicated (image size 24 nm×24 nm) and (b) close-up of honeycomb structure with molecular model. (c) STM topograph of dimer-row structure with unit cell indicated (image size 18 nm×18 nm) and (d) close-up of dimer-row structure with molecular model. For simplified molecules DFT calculations yield two coordination geometries, either by (e) two adatoms or by one adatom in (f) trans or (g) cis geometry.

temperature range around 200°C is also supported by other studies.^[85,96] The coordination of thiolates with copper centers can occur in two topologically distinct ways, as it was confirmed by density functional theory (DFT) calculations. Accordingly, for a simplified molecule, i.e. a benzene thiolate, three thermodynamically stable conformations exist as figure 3.5(e)-(g) illustrate. Coordination can either occur by two adatoms yielding a straight head-to-head dimer or by one adatom resulting in so called trans and cis geometries as respective figures 3.5(e), 3.5(f), and 3.5(g) depict. A dumb-bell shaped dimer coordinated via two adatoms is the basic building block for both structures as the models in figure 3.5 suggest. With the trithiolates coordinated to their next neighbors exclusively by double coordination, the hexagonal honeycomb

structure emerges. In the less symmetric structure, parallel rows of dimers can be identified where adjacent rows are shifted half a lattice constant with respect to the row direction. Based on structural data and DFT calculations, one-atom coordination in a cis-like geometry is most suitable and responsible for the bonding of dimers. The complete manuscript of this study can be found in 6.5.

3.3 Covalent Bonds

Since the experimental discovery of graphene, a monolayer of sp^2 hybridized carbon atoms covalently interlinked into a 2D honeycomb lattice, in 2004,^[97] a dramatic increase in research efforts and resulting publications on this subject had set in. The reason is that graphene, also named "the rising star on the horizon of materials science",^[98] exhibits outstanding mechanical^[99,100] and electronic^[101–103] properties, and is hence considered to be a very promising new 2D material for various applications. Linking organic molecules into 2D conjugated polymers would be a way to synthesize graphene-like 2D materials. Those might have slightly varying physical properties and are therefore highly desired, because a variety of possible new structures could allow for tuning properties of new synthetic materials.^[24] Especially engineering a band gap that is absent in graphene is of utmost importance for electronic applications. Although various approaches for the synthesis have been discussed,^[26] due to the irreversible nature of covalent bonds, no defect-free continuous polymer sheet has been fabricated so far. Recent examples are for instance the square lattice of tetrakis(bromophenyl)porphyrin on Au(111) by Grill and coworkers^[104] or the honeycomb network of poly(phenylenediboronic anhydride) on Au(111) by Zwaneveld and coworkers.^[105] However, appropriate reactions that allow for reversibility in covalent bonds, which would facilitate ordered structures, are rare. Possible strategies include either a preordered self-assembled molecular array (topochemical reaction) where covalent coupling is achieved in a post-treatment step or a self-repair mechanism (e.g. through a condensation reaction under reversible conditions), in which mislinked units can dissociate again and reconnect to converge into the thermodynamically most stable long range ordered structure.^[24]

Here, covalent coupling of the halogenated species TBB has been studied. Exploiting an Ullmann like reaction,^[106] where halogenated aromatic species dissociatively adsorb on a copper catalyst, cleavage of the carbon-bromine bond could be achieved. Thereby comparatively strong bonds between the resulting radicals and copper atoms supplied by the substrate are formed, leading to aggregates also denoted as *protopolymers*. An STM topograph of TBB-protopolymer networks on Cu(111), i.e., radical-metal coordination complexes, is depicted in Figure 3.6(a). Bright circular protrusions amidst triangular molecular units are clearly discernible, and readily identified as copper atoms. In a sense, protopolymers can be seen as coordination complexes with radical species as ligands. However, an unambiguous experimental indication for protopolymer formation is the center-to-center distance between interlinked molecules. In full agreement with the anticipated value for protopolymers, a distance of 1.50 nm was found. The irregularity and high defect density of these networks is owed to both the

pronounced reactivity of phenyl radicals and the low directionality of coordination bonds. By virtue of a post-annealing step (up to 300°C), it was possible to release the copper atoms and eventually convert metal-coordination bonds into covalent C-C interlinks (figure 3.6(b)). This is accompanied and proven by a 0.25 nm decrease of the center-to-center distance of adjacent interconnected TBB molecules from 1.50 nm to 1.25 nm.^[107,108] As a consequence the hexagonal lattice parameter takes a value of approximately 2.2 nm as the line scan in figure 3.6(d) shows.

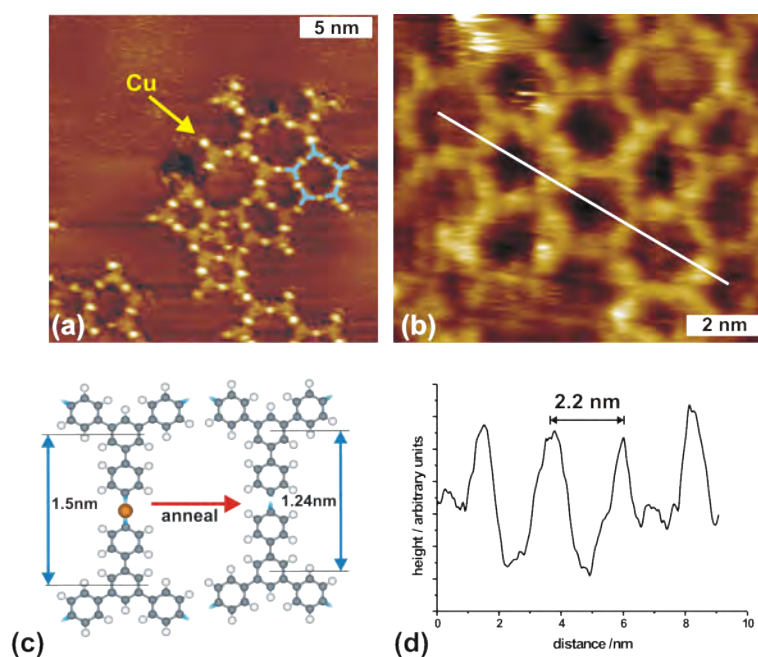


Figure 3.6: (a) TBB protopolymer on Cu(111). The bright spots in between single molecules represent single copper atoms coordinating the TBB radicals. (b) After annealing the sample bright protrusions have disappeared and the center-to-center distance of adjacent molecules has decreased from 1.49 nm to 1.24 nm. (c) Schematic pictures of center-to-center distance shrinking, when protopolymers are converted into covalently coupled TBB molecules. (d) Line-scan providing experimental proof for the hexagonal lattice parameter of 2.2 nm.

4 Molecule-Substrate-Interactions and Reactivity

In this chapter theoretical concepts to describe the bonding of molecules to crystal surfaces are presented. A detailed picture of mechanisms involved is a prerequisite for the understanding of elementary processes such as self-assembly, diffusion, or catalytic reactions. Moreover, structural properties determining surface reactivity are discussed, in particular the concept of active sites. In the last part of this chapter the impact of the two-dimensional adatom gas on metal surfaces interacting with adsorbates is outlined.

4.1 Physisorption

Physisorption generally describes weak bonding situations as a result of attractive long-range interactions and is especially important at low temperatures and/or chemically inert surfaces. The underlying interaction is the van-der-Waals force (between two particles). Physisorption is the analogon to describe adsorption on surfaces mediated by dispersion forces. This type of force is ubiquitous and is e.g. responsible for the condensation of noble gases or molecular adsorption on chemically inert substrates like graphite. Upon physisorption geometrical and electronic structure of adsorbates remain essentially undisturbed as a result of the weakness of the interaction. The term physisorption is not strictly defined in literature, however in the following it will be restricted to adsorption mediated by van-der-Waals forces. Van-der-Waals forces originate from fluctuations in charge distribution generating dynamic dipole moments. This temporary dipole moment can then induce another dipole moment into a molecule and cause an attractive force by electrostatic dipole-dipole interactions. The two-particle problem is described by the Lennard-Jones potential

$$E_{\text{pot}} = E_{\text{rep}}(r) + E_{\text{attr}}(r) = 4\epsilon \left\{ \left(\frac{\sigma}{r} \right)^{12} - \left(\frac{\sigma}{r} \right)^6 \right\} \quad (4.1)$$

where σ corresponds to the distance where the potential is zero and ϵ is the depth of the potential minimum. The attractive contribution scales with r^{-6} whereas the repulsive contribution which is dominant at small distances is approximated to be proportional to r^{-12} . It describes Pauli repulsion and arises from the overlap of occupied atomic

orbitals. Now, in order to describe physisorption of an adsorbate on a surface one has to sum over all possible two-body interactions with all atoms of the solid.^[109]

$$\begin{aligned}
 E_{\text{physisorption}}(\vec{r}) &= \sum_i E_{\text{rep},i}(|\vec{r} - \vec{r}_i|) + E_{\text{attr},i}(|\vec{r} - \vec{r}_i|) \\
 &= \sum_i 4\epsilon \left\{ \left(\frac{\sigma}{|\vec{r} - \vec{r}_i|} \right)^{12} - \left(\frac{\sigma}{|\vec{r} - \vec{r}_i|} \right)^6 \right\}
 \end{aligned}
 \tag{4.2}$$

This approach presumes additivity of pair potentials and neglects interparticle interactions between adsorbates, which are for instance very important when monolayer adsorption is considered. However, it is very intuitive for adsorption of single atoms. For not too small bonding distances, i.e. the repulsive part is neglected, the sum can be replaced by an integral. Introducing the variable z as vertical distance of the adsorbed particle to the infinite surface, it can be shown that integration over the three dimensional half space reduces the attractive r^{-6} dependence between two particles to a z^{-3} dependence.^[109,110] This means that due to the extended surface, a physisorptive interaction decays more slowly than van-der Waals interaction between two isolated atoms. The minimum of the physisorption potential is generally a few Ångströms above the surface (as defined by the nuclei of the topmost surface atoms). Compared to chemisorption with typical binding energies of 100 kJ/mol - 500 kJ/mol physisorption is relatively weak (e.g. 2 kJ/mol - 10 kJ/mol for noble gases). However, for large planar molecules with large contact areas and many atoms, van-der-Waals forces may play a leading role in adsorbate-substrate systems. After the introduction

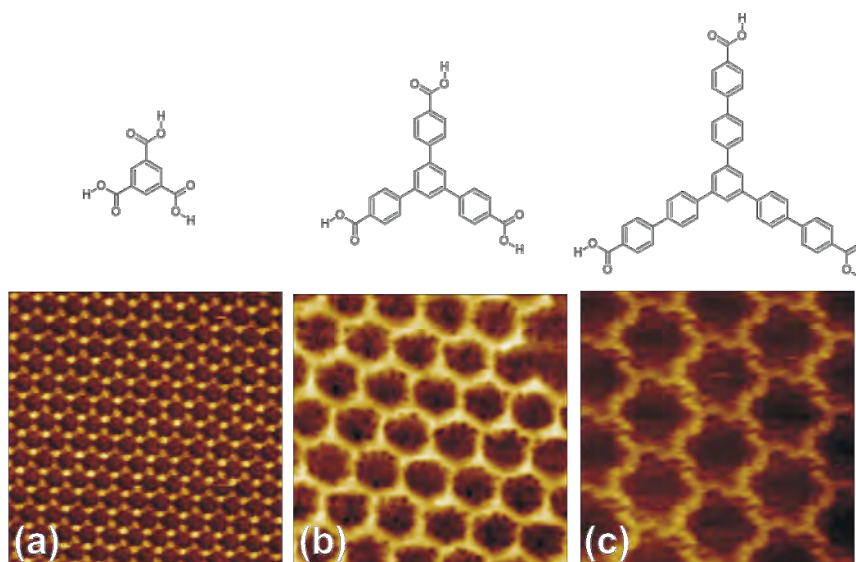


Figure 4.1: (a) Chemical structure of TMA and corresponding STM topograph. (b) Chemical structure of BTB and corresponding STM topograph. (c) Chemical structure of TCBPB and corresponding STM topograph. Images are 15 nm×15 nm in size.

of general concepts this behavior can be illustrated with an example of self-assembly

of 1,3,5-tris[40-carboxy(1,10-biphenyl-4-yl)]benzene (**TCBPB**) on graphite. Similar to the studies of melamine and fatty acids discussed in section 3.1, this system is an example of hydrogen bonded supramolecular networks on a chemically inert substrate. Accordingly, the experiments were conducted at the liquid-solid interface utilizing a suitable solvent. TCBPB, as depicted in figure 4.1(c), is composed of seven phenyl rings, functionalized with carboxylic acid groups in a 3-fold symmetric manner, and gives rise to a large van-der-Waals interaction with the graphite surface due to its large size. As previous studies showed, smaller 3-fold symmetric carboxylic acids as trimesic acid (**TMA**)^[111,112] and 1,3,5-benzenetricarboxylic acid (**BTB**)^[113,114] form 2D nanoporous hexagonal networks under suitable conditions. Intermolecular stabilization is facilitated by double O-H \cdots O hydrogen bonds via carboxylic groups. Molecules and corresponding STM topographs of respective networks are shown in figure 4.1. The aim to use TCBPB was to self-assemble larger isotopological networks with increased pore sizes. However, this goal could not be achieved. Instead of the desired head-to-head interconnection via O-H \cdots O hydrogen bonds (figure 4.2(a)) only structures based on displaced dimers stabilized by energetically inferior C-H \cdots O hydrogen bonds (figure 4.2(b)) were observed. These findings can be rationalized

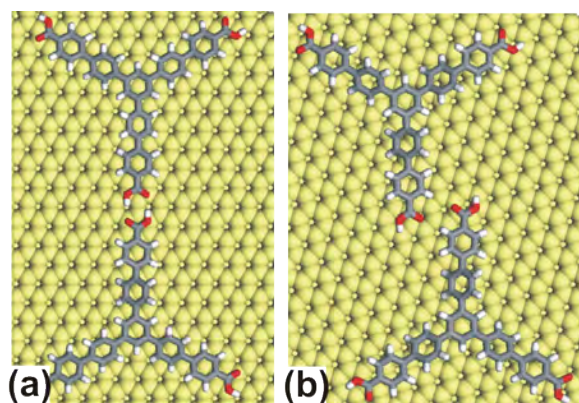


Figure 4.2: Molecular mechanics simulations of a TCBPB dimer stabilized by (a) O-H \cdots O hydrogen bonds in a head-to-head geometry and (b) by C-H \cdots O hydrogen bonds in a displaced geometry.

by simple thermodynamic arguments. Considering two honeycomb polymorphs, one, based on head-to-head interconnection (which is hypothetical) and one based on displaced dimers (which has been observed in experiments), Gibbs free energies can be attributed to the two polymorphs, respectively. It is determined by an enthalpic gain and an entropic cost that arises when molecules self-assemble from the dissolved state in solution into the ordered on-surface crystalline state. Now, the Gibbs free energy for an isolated head-to-head dimer is certainly lower due to the stronger hydrogen bonds, but considering monolayer coverage and the whole liquid-solid system, the higher packing density that is achieved for the displaced dimer structure favors the formation of this structure. This becomes obvious when the Gibbs free energy per surface is taken into account. A detailed discussion of this work is given in the manuscript 6.4.

4.2 Chemisorption

The term chemisorption corresponds to the formation of a chemical bond between atomic or molecular adsorbates and surfaces. The familiar covalent bond picture involving formation of bonding and antibonding orbitals from two atomic orbitals does not strictly apply to the adsorbate-surface bond. In this case the adsorbate states do not only interact with a single state, but rather with a continuum of states. The *Anderson-Grimely-Newns* approach^[115,116] and related theories provide a useful quantitative description.^[117,118] The basic features of this model are illustrated in figure 4.3 for two limiting cases.

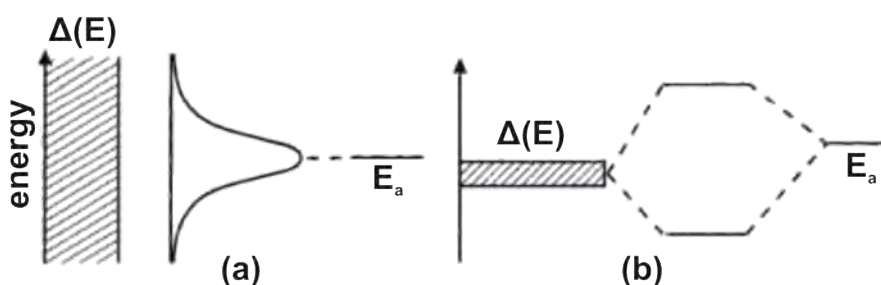


Figure 4.3: Energy levels E and LDOS of the substrate on the left hand side, and the unaffected adsorbate on the right hand side in the Newns-Anderson model. At the center the electronic structure of the adsorbate is depicted. Two limiting cases are discussed: **(a)** A broad band of substrate states gives rise to a resonance with a Lorentzian shaped LDOS of the adsorbate. **(b)** A narrow substrate band creates bonding and antibonding states. Image adapted from Venables.^[119]

In the case of broad bands (sp-band), as it is the case for transition metals,^[120] the metal DOS (projected on the adsorbate state $\Delta(E)^*$) is fairly independent of energy. Upon adsorption a sharp atomic energy level broadens into a Lorentzian shaped distribution $n_a(E)$ and a slight shift in energy occurs. This energetic broadening and shift is referred to as *renormalization*.^[121–123] For narrow bands on the other hand (d-band), the situation resembles more the simple two-level interaction of an ordinary chemical bond, i.e. sharp bonding and antibonding orbitals are formed at energies above and below the initial adsorbate level. This interaction is in particular dominated by the so-called *frontier orbitals*, i.e. HOMO and LUMO or a subset of states close to these orbitals for a molecular adsorbate.^[118] Upon interacting with the metal d-band, both states split into bonding and antibonding states with respect to the surface-molecule bond. The position of the Fermi level now determines the overall energy gain or loss upon interaction, thus strength and character (repulsive or attractive). If the bonding

*The projected density of states (PDOS) is a quantity similar to the LDOS, but weighted with the overlap integral between surface wavefunctions Ψ_i and adsorbate state Φ_a : $\rho_a(E, \vec{r}) = \sum_i \delta(E_i - E) |\langle \Psi_i(\vec{r}) | \Phi_a(\vec{r}) \rangle|^2$.

states of the newly emerged orbitals are occupied and the antibonding states remain empty, the interaction is attractive. If both, bonding and antibonding states are occupied, the interaction is repulsive, because antibonding states exhibit a higher energy shift than bonding states. Chemisorption on transition metals is generally described as a two-step mechanism of renormalization and level splitting as illustrated in figure 4.4.

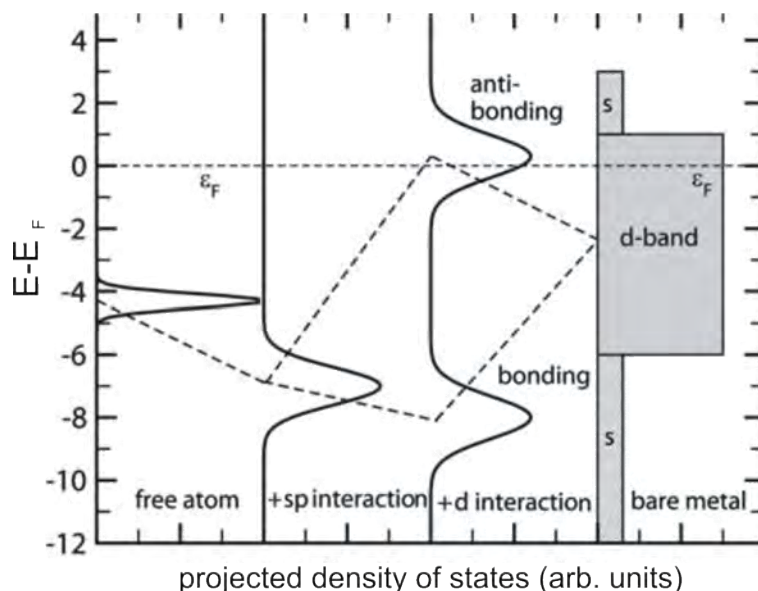


Figure 4.4: Schematic drawing of the interaction of an atomic level with a transition metal surface. Firstly, interaction with the metal sp -band causes level broadening and shift. Subsequent interaction with the d -band leads to level splitting into bonding and antibonding states. The position of the antibonding states with respect to the Fermi level determines whether the overall interaction is attractive or repulsive. Figure adapted from Groß.^[118]

In order to describe adsorption on different transition metal surfaces, Hammer and Nørskov explain the bonding strength through the energetic position of the d -band center E_d with respect to the Fermi level E_F .^[117] This is in line with the *Anderson-Grimely-News* approach^[124] since the sp -bands are broad and comparable for the different transition metals. The d -bands differ in their degrees of filling, and hence the position of the d -band center. By moving from right to left in the periodic table of elements, the d -band center moves up in energy with respect to the Fermi level. Consequently the interaction with an adsorbate yields more and more unoccupied antibonding states and a stronger bond emerges. This is the reason why noble metals as Ag and Au are less reactive than early transition metals.

However, in order to explain reactivity trends of elements with $d^{10}s^1$ electron configuration (i.e. the noble metals Cu, Ag, and Au), one has to take into account that not only relative energies of metal and adsorbate states are important, but also the magnitude of coupling which basically scales with orbital overlap.^[110] The laws of quantum mechanics dictate that newly emerged states need to be orthogonal. The

associated energy cost is called *orthogonalization energy*.^[125] The energetic cost of the orthogonalization is also the reason why interaction of closed-shell atoms such as rare gases with surfaces is usually repulsive except for weak van-der-Waals attraction.^[118] So the orthogonalization energy, i.e. the repulsive contribution, between adsorbate and metal d-states is considerably larger for 5d metals (Au) than for 3d metals (Cu) because of the more pronounced spatial extension of 5d states.^[126] It increases down the groups of the periodic table of elements rendering for instance Au less reactive than Cu.^[125]

Chemisorption of more complex molecules involves more complex subsequent processes. An important aspect in this context is charge transfer from the substrate to the adsorbate. One example is dissociative adsorption, i.e. weakening and finally cleavage of an intramolecular bond as a consequence of interactions (e.g. charge transfer) with the substrate. Dissociative adsorption of TBB adsorbed on coinage metals supports general trends in reactivity, and molecule-surface interaction strength as discussed above. As shown in the previous chapter, C-Br bonds within TBB molecules dissociate upon adsorption on Cu(111) (see section 3.3), whereas on Ag(111) TBB molecules stay intact (see section 3.1). First experiments on Au(111) suggest a qualitatively similar behavior as for Ag(111), i.e. adsorption of intact molecules. Material-dependent dissociative adsorption can be explained by stronger interaction of TBB with Cu surfaces than with Ag and Au surfaces, which also leads to a larger partial filling of antibonding π^* orbital (LUMO). According to the rationale outlined before, this would cause more repulsion since antibonding orbitals are occupied. However, here a two-step mechanism facilitating C-Br bond cleavage is proposed as sketched in figure 4.5. Since the π^* orbital of TBB is mainly localized at the aromatic system,

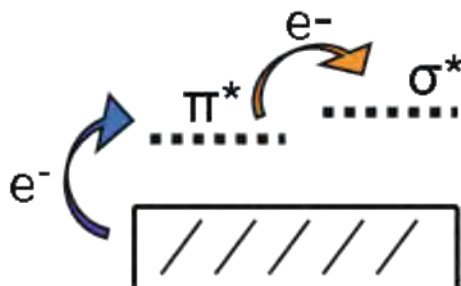


Figure 4.5: Proposed two-step mechanism for the C-Br bond dissociation upon adsorption on reactive surfaces. Occupation of an antibonding π^* orbital is followed by intramolecular charge transfer into the σ^* orbital leading to a destabilization of the bond.

adsorption induced charge transfer can not exclusively explain the observed homolysis of peripheral C-Br bonds. Hence, in a second step thermally activated intramolecular charge transfer from the newly occupied π^* orbital into σ^* orbitals, which are antibonding with respect to the C-Br bond, is proposed. Eventually these bonds destabilize and bond scission is facilitated. A more detailed discussion can be found in the manuscript 6.2.

4.3 Active Sites

In 1925 H.S. Taylor first formulated the idea of active sites on a surface.^[127] It reflects the experimental evidence that the catalytic activity of a surface is not uniformly distributed over a crystal surface but exhibits special sites with enhanced activity. His tentative model relates increased reactivity with coordination numbers of surface atoms, i.e. the number of nearest neighbor atoms. In particular topological features like step edges, kinks, dislocations, or vacancies have lower coordination numbers as compared to terrace atoms. Consequently, active sites give rise to enhanced activity due to their unsaturated valencies. The terrace-step-kink (TSK) model, developed by Burton, Cabrera and Frank in the early 1950s describes the morphological features of a crystal surface on the atomic scale.^[128] It comprises the main defect structures as illustrated schematically in figure 4.6. The basic idea of this model is that the bond energy of an atom on a crystal surface is determined by its number of bonds to neighboring atoms. Transitions simply involve the counting of broken and newly formed bonds. The TSK model can be applied for the description of processes like surface diffusion, crystal growth, or roughening.

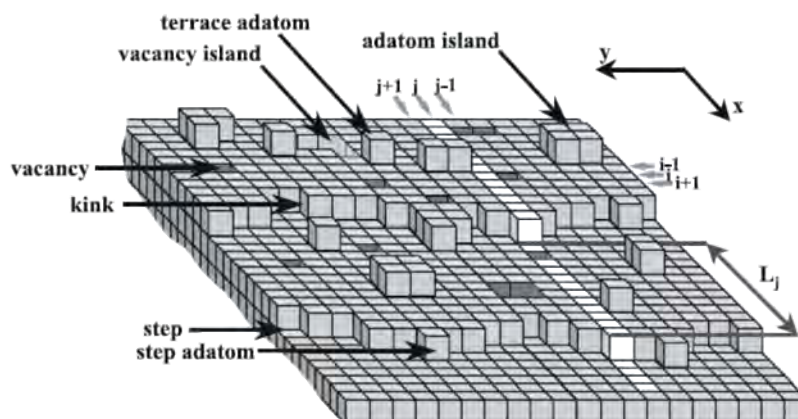


Figure 4.6: Atomic scale morphology of a crystal surface with its defect structures as described in the TSK model. Image taken from Giesen.^[96]

The understanding of atomic structure dependence of surface reactions has progressed enormously since the development of modern surface science and ultrahigh vacuum technology.^[129] Enhanced chemical activity of step sites as compared to close packed surfaces has been demonstrated for instance by Somorjai^[130,131], Yates^[132,133] and coworkers. As a consequence, the reactivity of catalytic surfaces is generally dominated by step edge sites.^[134,135] Besides, not surprisingly most industrial catalysts are comprised of nanoparticles spread over a support exposing a high density of active sites rather than close packed surfaces.

Figure 4.7 illustrates the role of step edges as active sites for molecular adsorption. In this example TBB molecules (are shown) to attach to step edges of a Cu(111) surface. The emergence of chemical bonds between molecules and step site atoms is

avored over bonding to terrace atoms. Strong molecule-molecule interactions give rise to subsequent domain growth, so step edges in this case act as nucleation centers. Accordingly catalytic activity of a surface can also be passivated by pre-occupying all step sites with adsorbates. For instance Zambelli *et al.* have identified steps to be active sites for NO dissociation on Ru(001).^[50] On this surface two different types of steps are present, differing in geometric structure, and hence reactivity. On one type of steps oxygen tends to stably chemisorb upon NO dissociation and block these sites. This causes deactivation of steps inhibiting further NO dissociation. This effect is referred to as self-poisoning of a catalyst.^[135] Now, considering the hypothetical

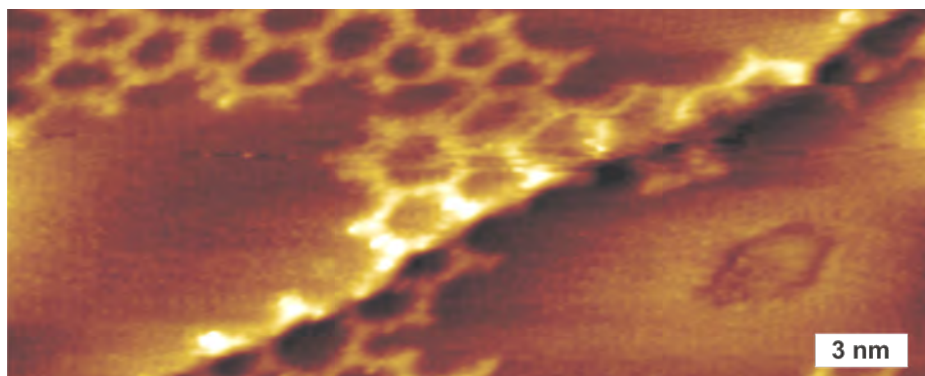


Figure 4.7: TBB molecules decorating a step edge of a Cu(111) surface.

case of a perfectly flat single crystal surface without any defect sites, a dependency of reactivity on coordination number is also present. Figure 4.8 shows low-index surface planes of an fcc crystal: (111), (100), and (110). Respective coordination numbers of topmost surface atoms are 9, 8, and 7. Hence an orientation dependency of reactivity is also to be expected for ideal surfaces. This behavior can be illustrated comparing TBB adsorption on Ag(111) and Ag(110). C-Br bond breaking is present for TBB adsorption on Ag(110) followed by subsequent formation of protopolymers - a qualitatively similar behavior as observed on Cu(111) as discussed in section 3.3. This could be unambiguously proven by the characteristic center-to-center distance of 1.5 nm between two bound molecules. However, on Ag(111), a variety of long-range ordered self-assembled phases were found upon room temperature deposition (see section 3.1). Center-to-center distances between (in this case slightly displaced) dimers within a self-assembled phase are considerably larger (2.0 nm) which is a clear indication for the absence of a dehalogenation reaction. Molecular aggregates are stabilized by halogen-halogen interactions between intact molecules. The fact that a chemical reaction, in particular dissociative adsorption, does occur on lower coordinated (110) planes, and does not on the higher coordinated (111) planes underlines the influence of crystallographic surface orientation and surface atom coordination on reactivity. These findings can accordingly also be explained in terms of interactions with d-bands as discussed in the previous section, since the d-band center also varies with coordination number: The width of the band is directly related to the coordination and the overlap of the orbitals. The smaller the coordination number of a particular atom, the narrower the d-band at this site. In order to maintain constant

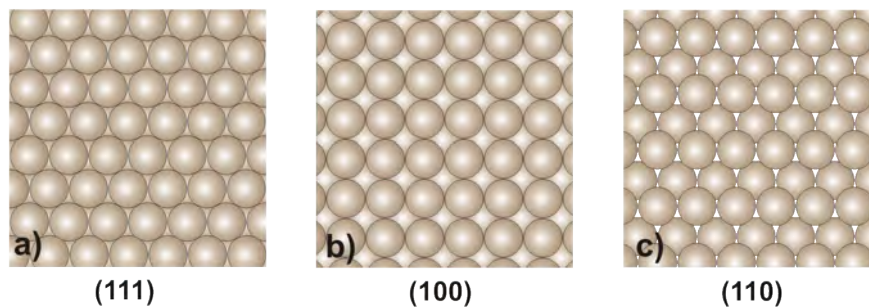


Figure 4.8: Top layer atomic arrangements of ideal low-index surface planes of an fcc crystal

filling, the d-band center then has to move up in energy so that the number of occupied states remains conserved.^[118] Hence also the d-band center shifts up which leads to higher reactivity. The same argument applies for crystallographic orientations with lower Miller indices. The more open a surface the lower the coordination number of surface atoms. Consequently this leads to increased adsorbate-substrate interaction for fcc(110) as compared to fcc(111). A more profound discussion illustrated with STM data is given in the manuscript 6.3.

4.4 2D Adatom Gas

An important property of real surfaces is the presence of a two-dimensional lattice gas of mobile adatoms at finite temperatures. It originates from a temperature-dependent evaporation/condensation equilibrium at step edges. Within the scope of the TSK model introduced in the previous section (see figure 4.6), adatoms can be viewed as dynamic active sites that contribute significantly to the reactivity, thus catalytic behavior of a surface. Adatoms behave like a two-dimensional gas and hence physical properties as pressure, concentration, or temperature (kinetic energy) can be used to describe their behavior. A detailed knowledge of the mechanisms is highly desired since many modern technologies depend on the ability to grow thin films.^[136] The concentration of the adatom gas strongly depends on material, temperature, crystallographic orientation, and surface morphology.^[137] Its diffusion kinetics can be rationalized by hopping processes (of adatoms) from one potential minimum to another in a 2D potential hypersurface. For pronounced anisotropic surfaces as fcc(110) also atomic exchange mechanisms are discussed.^[138] The temperature dependent hopping rate h is characterized by an Arrhenius relation

$$h = h_0 e^{-\frac{E_D}{k_B T}}. \quad (4.3)$$

Herein h_0 is the attempt frequency or pre-exponential factor,^[139] E_D the activation energy or barrier height of the corrugated potential, k_B the Boltzmann constant and

T is temperature. For anisotropic surfaces, of course also a directional dependence - mainly for the activation energy - is important, giving rise to orientation dependent values of E_D . For a given fcc metal the activation energy is generally lowest for diffusion on the (111) plane, due to the small corrugation of the surface potential caused by dense packing. On (111), E_D can be one order of magnitude smaller than for other low index planes.^[140] In the theoretical work of Liu *et al.* activation barriers for various fcc metals in different crystallographic orientations are calculated and compared with experimental data.^[140] For Cu, calculated values for (111), (110)_{||}, (110)_⊥, and (100) are 0.044 eV, 0.28 eV, 0.32 eV, and 0.53 eV, respectively. A possible method to experimentally determine adatom densities is low energy electron microscopy (LEEM).^[141] There, a beam of low energy electrons is directed towards the surface and a real space mapping of diffracted electrons can be obtained. Since the electron reflectivity is sensitive to the adatom density, for instance the temperature dependency of the 2D adatom gas can be studied.^[142]

Adatoms play also an important role for the synthesis of surface-confined MOFs. Generally, 2D metal-coordination networks are prepared either by co-deposition of metal atoms (e.g. Fe, Co)^[143–145] or by coordination of suitable organic building blocks through freely diffusing adatoms.^[85–87] In the latter case the temperature dependence of the adatom concentration is exploited in the same way as in the example of copperthiolate networks in section 3.2. Thermal annealing causes an increase of adatom density which eventually facilitates the formation of coordination networks. Now, the decisive influence of the chemical nature of adatoms could be demonstrated within a series of experiments of TMB on Ag(111). Figure 4.9(a) shows the self-assembled

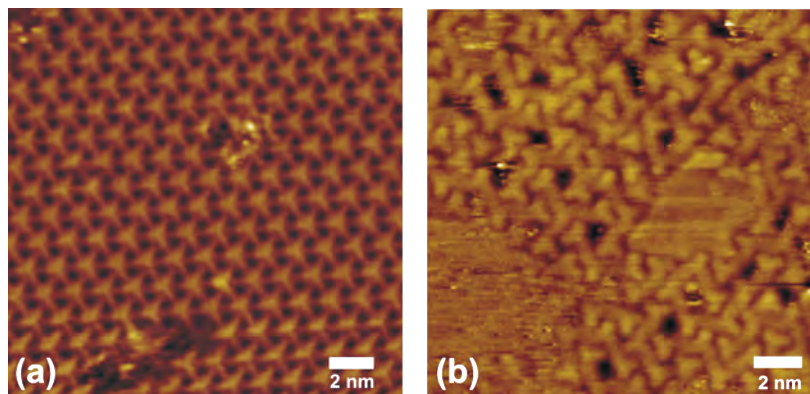


Figure 4.9: TMB on Ag(111). (a) Initial self-assembled close packed structure formed upon room temperature deposition. (b) Onset of polymerization and subsequent degradation at elevated temperatures. TMB molecules tend to randomly bind to neighboring molecules resulting in amorphous films.

close packed trigonal structure of TMB molecules on Ag(111) similar to the structure observed on Cu(111) before thermal annealing. As the STM images in figure 3.5 in section 3.2 showed, metal-coordination networks could be synthesized on Cu(111) in a thermal annealing step, where copper adatoms coordinate the thiolate groups. On Ag(111) this conversion could not be achieved by annealing even when applying

different annealing parameters of temperature and duration. Instead, at some temperature polymerization and deterioration begun, resulting in amorphous molecular films. This degradation has also been observed for TMB on Cu(111) at higher annealing temperatures. However, on Cu(111) for intermediate temperatures highly ordered MOFs formed. Figure 4.9(b) shows an example of such an amorphous film. Single molecules can be identified binding randomly to neighboring molecules. This example underlines the crucial role of the chemical nature of adatoms. Diffusion barriers and adatom densities on Cu(111) and Ag(111) are comparable in magnitude^[140] and accordingly the properties of the 2D adatom gas. Consequently, a major influence through adatom density or mobility can be excluded. A possible explanation for the metal-coordination networks only forming on Cu(111) but not on Ag(111) lies hence in the superiority of copper-thiolate bonds that renders copper-thiolate networks more stable than silver-thiolate networks. Nature confirms this fact since thiolate copper coordination complexes are very common and occur for instance naturally in proteins.^[146]

5 Summary

In summary, this work aimed at the synthesis of surface supported 2D molecular networks from organic molecules as basic building blocks. The still not fully understood hypothesis that emerging structures result from a complex interplay between adsorbate-substrate as well as adsorbate-adsorbate interactions is investigated and exemplified in different systems, where in particular the type and strength of adsorbate-adsorbate interactions was varied. STM images provide precise structural data for the interpretations in this work. Structural data is also used for comparison with theoretical models or as a boundary condition for accompanying theoretical studies. For liquid-solid interface experiments chemically rather inert graphite is used as substrate. The interaction of adsorbates with the substrate is physisorptive, and thus relatively weak. Consequently intermolecular interactions dominate these systems. Based on reversible hydrogen bonds as the intermolecular mediators, for the bimolecular system of melamine and fatty acids, self-assembled highly ordered structures are found. In this system, alkane tails of fatty acid solvent molecules with different chain lengths can be used as linear spacers to tune the lattice parameter of hexagonal bimolecular networks. The dependency of van-der-Waals forces on contact area between adsorbate and substrate is demonstrated in a set of experiments with larger organic molecules. For a tricarboxylic acid comprised of seven phenyl rings, unexpected structures were found, where hydrogen bond energies are not optimized. However, a more dense packing optimizes adsorbate-substrate interactions, resulting in higher thermodynamic stability.

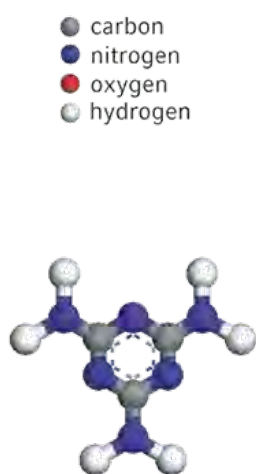
Since hydrogen bonded systems have been extensively studied in the last decades, a strong motivation was also to interlink organic molecules by stronger interactions such as metal-coordination and covalent bonds. Especially with regard to possible applications of organic monolayers, strong intermolecular coupling - mechanically, chemically, and electronically - is a highly desired material property for 2D molecular networks. Whereas covalently coupled long range ordered molecular crystals are a not yet realized challenge in materials science, ordered systems stabilized by metal-coordination bonds have been synthesized in the past. They represent a compromise between weak but reversible hydrogen bonds and strong but irreversible covalent bonds. In this thesis two molecules with similar aromatic backbone, but different functional head groups were studied through adsorption on noble metal substrates. Substrate induced chemical reactions are observed for a halogenated species. Intramolecular C-Br bonds are dissociated upon adsorption on strongly interacting substrates whereas these molecules remain intact on less reactive substrates. This process is shown to be thermally activated since no such reaction occurs at temperatures as low as 80 K, even on reactive substrates. Dissociative adsorption is followed by coordination of organic

radicals with metal adatoms to form so called protopolymers, in some respect a special type of metal coordination with pronounced covalent character. Thermal annealing can release coordinating copper atoms and convert protopolymers into covalent networks. However, a high defect density is observed and related to the irreversible character of covalent bonds. Besides, the question about surface reactivity and thus catalytic activity is also addressed in this context. Theoretical models and concepts are discussed and related to the experimental observations. In line with the Newns-Anderson-Grimely model, hybridization effects between molecular orbitals and metal bands, in particular d-bands of transition metals, can explain these results. Accordingly, reactivity of transition metals increases moving left in the periodic system of elements and decreases moving down, which is in accord with experimental findings. Interaction strength of a specific site also correlates with coordination number, i.e. the number of nearest neighbors of a surface atom. As a consequence one- and zero-dimensional defect structures as step edges, kinks, or dislocations represent sites on a crystal with increased reactivity, so-called active sites. More generally, this characteristic also applies to different crystallographic surface orientations rendering fcc(111) less reactive than fcc(110). The halogenated molecules do accordingly adsorb intactly on Ag(111) whereas on Ag(110) bond scission is observed.

Another important material property of metal surfaces is the two dimensional gas of adatoms. By thermal activation, its concentration can be significantly increased leading to onset of e.g. phase transition in adsorbate layers or surface chemical reactions. For aromatic trithiols self-assembled on Cu(111), an adatom mediated conversion into metal-organic frameworks is observed. Coordination of the molecular building blocks occurs via Cu-S bridges. Due to the strong electronic coupling of Cu-S links, these interlinks exhibit delocalized electronic states and are thus considered very promising with regard to molecular electronics applications. On Ag(111) the MOFs could not be reproduced underlining the fact that the chemical species of an adatom gas is also a crucial parameter for its activity.

6 Publications

6.1 Isotopological Supramolecular Networks from Melamine and Fatty Acids



a)

	ball and stick model	carbon count
pentanoic acid		5
hexanoic acid		6
heptanoic acid		7
octanoic acid		8
nonanoic acid		9
decanoic acid		10
undecanoic acid		11
dodecanoic acid		12
tridecanoic acid		13

b)

J. Phys. Chem. C., **2009**, 113, 1014-1019
Hermann Walch, Anne-Kathrin Maier, Wolfgang M. Heckl, and Markus Lackinger

Isotopological Supramolecular Networks from Melamine and Fatty Acids

Hermann Walch,^{*,†} Anne-Kathrin Maier,[†] Wolfgang M. Heckl,^{†,‡} and Markus Lackinger^{*,†}

Department for Earth and Environmental Sciences and Center for NanoScience (CeNS),
Ludwig-Maximilians-University Munich, Theresienstr. 41, D-80333 München, Germany, and
Deutsches Museum, Museumsinsel 1, D-80538 München, Germany

Received: September 4, 2008; Revised Manuscript Received: October 27, 2008

The formation of bimolecular isotopological monolayers comprised of melamine and members of the homologous series of fatty acids extending from pentanoic through tridecanoic acid was studied at the liquid–graphite interface by scanning tunneling microscopy. In these systems, the fatty acids not only serve as solvents, i.e., provider and transport medium for solute molecules, but are also a structure determining part of the self-assembled monolayers. For all solvents, hexagonal structures were observed where the lattice parameter increases linearly with the chain length of the fatty acid from 2.8 nm for pentanoic acid to 4.1 nm for tridecanoic acid. All bimolecular networks exhibit the same topology: the basic unit consists of a melamine hexamer which is stabilized by internal N···H–N hydrogen bonds and surrounded by 12 radially arranged fatty acid molecules. The *p6* symmetry of the monolayer originates from the melamine core, whereas the lattice parameter is determined by the aliphatic chain length of the fatty acid. For a deeper insight into the relative energetics, all experimentally observed structures were simulated by force-field calculations

Introduction

Isotopological structures share the same building plan, but the size, i.e., in case of crystalline systems the lattice parameter, is variable due to different dimensions of interchangeable constituents. Scalability, as a general, widely encountered concept and principle, has always attracted much attention. Particularly in material science scalability is a very intriguing property since it may allow for the gradual variation of specific material properties. Also, in many cases, the synthesis follows the same pathway for all structures. Prominent examples are the iso reticular–metal organic frameworks (IR-MOFs), discovered and characterized by Yaghi et al.¹ There, a [Zn₄O]⁶⁺ tetraeder serves as a connection point and various deprotonated para-dicarboxylic acids are the interconnecting spokes. Owing to the $\bar{4}3m$ symmetry of the connection points, referred to as secondary building units (SBU), most structures are cubic and the lattice constant ranges from 1.29 to 3.43 nm. The accompanying variation in pore diameter makes these mesoporous structures highly interesting for applications in the field of size selection and gas separation.² In case of IR-MOFs, the SBUs and organic spokes are interconnected through metal coordination bonds. Likewise, two-dimensional isotopological metal coordination networks were observed for cobalt atoms with dicarbonitrile-polyphenyl molecules on Ag(111).³ Here we present a bimolecular system where the dominating interactions are hydrogen bonds. Despite the relative weakness of hydrogen bonds (here ~6–10 kcal/mol for a 2-fold hydrogen bond) as compared to coordination bonds (typically 10–20 kcal/mol), a remarkable scalability of the system was found and the use of aliphatic spacers facilitates fine-tuning of the lattice parameter.

Experimental Section

All experiments were conducted with a home-built STM operated by a commercial RHK SPM-100 control system. Tips were mechanically cut from a Pt/Ir wire (90/10). Chemicals were used as received from Sigma-Aldrich without further purification. Saturated solutions were prepared by adding melamine to fatty acids (~5 mL) until precipitation occurs. A small droplet (~10 μ L) of solution was then applied to the freshly cleaved basal plane of highly oriented pyrolytic graphite (HOPG) substrates. Topographs were obtained in the constant current mode of operation with the tip immersed into solution. Since fatty acids from decanoic acid on are already solid at room temperature, a heatable sample holder was used which enables imaging at sample temperatures up to ~60 °C. The heating stage consists of a resistance wire embedded into thermally conducting epoxy resin and is thermally well isolated from the instrument. Careful shielding and a high electrical resistance of the heating wire (diameter 0.045 mm), i.e. low driving currents (typically ~30 mA), minimize cross-talk with the signal. The graphite sample is directly attached to the heating stage and a dc heating power of ~0.3 W is sufficient to maintain surface temperatures around ~50 °C. For decanoic through tridecanoic acid, solutions were saturated at ~50 °C and directly applied to the preheated sample holder. Before the coarse approach, the tip is immersed into solution and allowed to thermally equilibrate for ~10 min. This procedure is necessary to reduce lateral and vertical thermal drift. In order to exclude artifacts due to thermal drift and nonideal piezo behavior, adsorbate lattice parameters were precisely determined by means of calibration images, where both the monolayer and the underlying graphite were imaged within one frame.

Results and Discussion

Melamine is a heterocyclic aromatic molecule and consists of a triazine ring endowed with three amine groups at the 2, 4, and 6 positions. Melamine is well functionalized for intermo-

* To whom correspondence should be addressed. E-mail: hermann.walch@physik.unimuenchen.de; markus@lackinger.org.

[†] Ludwig-Maximilians-University Munich.

[‡] Deutsches Museum.

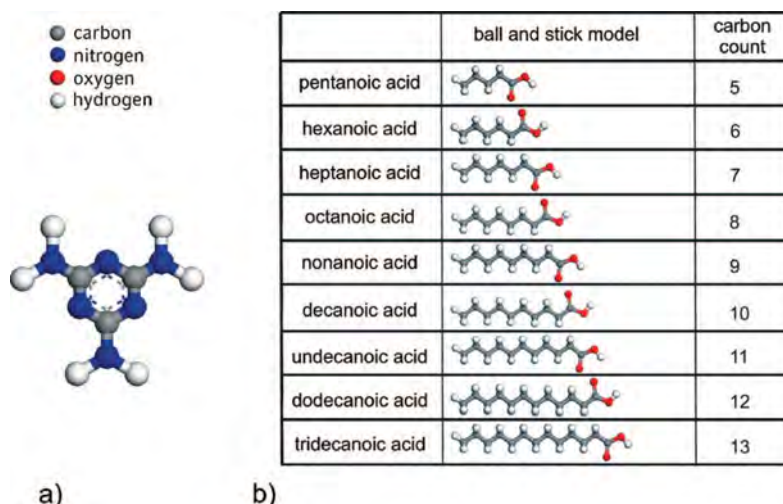


Figure 1. Chemical structures of (a) melamine and (b) the homologous series of 1-fatty acids used in this study.

lecular hydrogen bonds: amine groups can act as proton donors whereas the nitrogen atoms in the triazine ring can be proton acceptors through their lone pair electrons. In addition, its planar geometry and the aromatic system can give rise to planar adsorption on various substrates, a prerequisite for studying the formation of two-dimensional hydrogen bonded networks.

On surfaces, melamine shows a high affinity to cocrystallize with other organic compounds. Several stable bimolecular structures were found upon coadsorption with PTCDI (perylene-tetracarboxylic-diimide) depending on mixing ratios and post deposition annealing procedures. After the observation of a hexagonal honeycomb network by Theobald et al.,⁴ Silly et al. discovered parallelogram structures,⁵ and a similarly hexagonal “pinwheel” structure.⁶ Experiments with PTCDA (3,4,9,10-perylene-tetracarboxylic-dianhydride) instead of PTCDI yielded row-like structures.⁷ Also cyanuric acid has been found to be a very suitable coadsorbant for melamine.^{8,9} Both cyanuric acid and melamine were observed to self-assemble into stable monolayers by themselves.^{10,11} For melamine, chiral and non-chiral monolayer structures were found, all based on 2-fold hydrogen bonds between adjacent molecules. The chiral structure is comprised of cyclically hydrogen bonded melamine hexamers where perpendicularly adsorbed melamine guest molecules were observed at the center.¹² Yet, all studies above were carried out under ultrahigh vacuum conditions with samples prepared by vapor deposition whereas the results presented here have been obtained at the liquid–solid interface. In contrast, molecules adsorbed at the liquid–solid interface can be in equilibrium with dissolved molecules and growth is often thermodynamically controlled, which renders the preparation of bimolecular networks more challenging.¹³ Similar to melamine, fatty acids can also act as acceptors and donors for hydrogen bonds through their carboxylic functionality.¹⁴ Moreover, their total length can be varied in increments of ~ 0.13 nm by adding further CH_2 groups to the alkane tail. In this work, all members of the homologous series between pentanoic and tridecanoic acid were found to cocrystallize with melamine at the solution–graphite interface.

An example of a well ordered hexagonal structure obtained with melamine in octanoic acid is depicted in Figure 2. The lattice parameter accounts to 3.3 nm and the contrast exhibits a hexagonal arrangement of 1.8 nm wide dark circular depressions separated by elevated (bright) walls. Similar topographs of

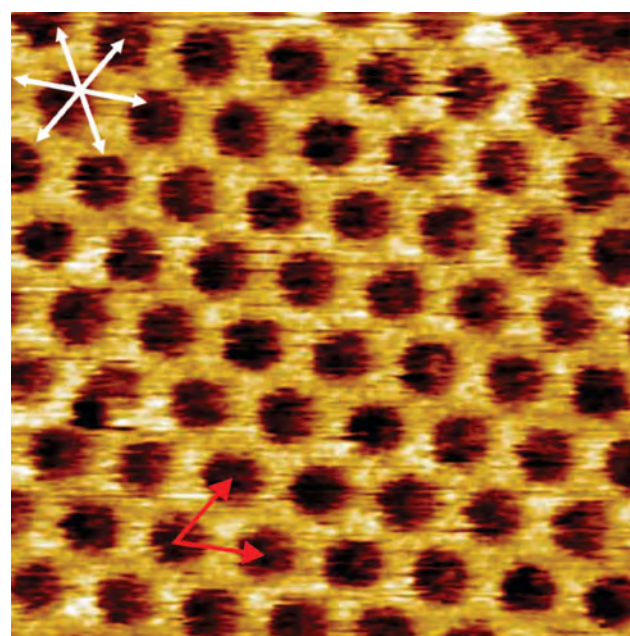


Figure 2. STM topograph obtained from melamine dissolved in octanoic acid at room temperature ($25 \times 25 \text{ nm}^2$) with $U_T = 1.0 \text{ V}$, $I_T = 70 \text{ pA}$. The structure is hexagonal with a lattice parameter of 3.3 nm, adsorbate lattice vectors are marked by red arrows. The white arrows in the upper left corner indicate the main axes of the underlying graphite substrate as deduced from calibration images.

hexagonal structures were obtained for all nine fatty acids investigated (cf. Supporting Information for a full set of topographs). For pentanoic through nonanoic acid, experiments were performed at room temperature, whereas for decanoic acid through tridecanoic acid, a sample temperature above the melting point of the respective solution was maintained by means of the heatable sample holder. Interestingly, as illustrated in Figure 3, a linear relation between the number of carbon atoms in the fatty acid solvent (referred to as carbon count) and the lattice parameter of the interfacial hexagonal monolayer was found.

A linear fit resulted in a slope of $0.15 \text{ nm}/(\text{carbon count})$ which corresponds to the increment of the lattice parameter from one fatty acid to the next higher one. Since the lattice parameter is a function of applied solvent and both contrast and symmetry

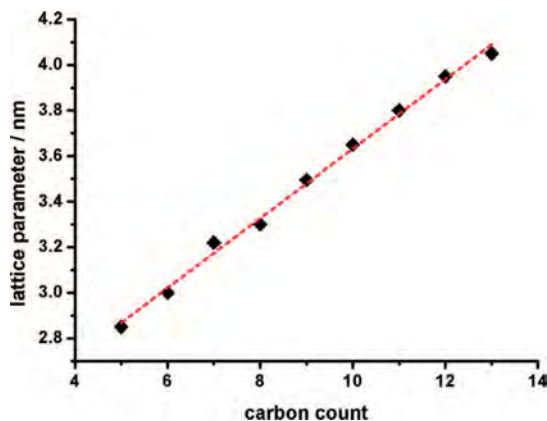


Figure 3. Dependency of experimentally determined lattice parameters of the hexagonal networks on the number of carbon atoms in the fatty acid solvent (carbon count). Lattice parameters were deduced from calibrated STM images and averaged over independent experimental runs. They range from (2.8 ± 0.1) nm for pentanoic acid to (4.1 ± 0.1) nm for tridecanoic acid. The slope of the linear fit ($R^2 = 0.995$), i.e., the increase of lattice parameter per additional carbon atom in the alkane tail of the solvent, corresponds to (0.15 ± 0.01) nm/(carbon count).

of the monolayer are entirely different from the row like structure of pure fatty acid monolayers,^{15–17} the formation of bimolecular networks comprised of melamine and solvent molecules can be concluded. Because the overall length of the fatty acid molecules also increases linearly with carbon count, it is very likely that the solvent accounts for the scalability of the network. Consequently, the symmetry of the monolayer is related to the trigonal symmetry of melamine possibly in combination with the hexagonal symmetry of the substrate. Surprisingly, with phenyloctane used as solvent no pure melamine monolayers could be observed, despite the molecule's capability to form extended hydrogen bonded sheets as observed on Au(111).¹¹ Also with iso-alcohols (nonanol, decanol, and undecanol) as solvents, only pure solvent monolayers were observed but no coadsorption with melamine. Apparently, the stabilizing influence of an additional compound with a relatively strong bond to melamine is required for melamine monolayer formation at the liquid–graphite interface. For two reasons fatty acids are very appropriate: first, they can form two hydrogen bonds ($O \cdots H-N$ and $O-H \cdots N$) per molecule with melamine and not only one as alcohols; second, the almost perfect registry between the alkane backbone and the graphite substrate leads to high adsorption energies for fatty acids which increase linearly with chain length. Remarkably, fatty acids which usually serve as a standard solvent for self-assembly of carboxylic acids at the liquid–solid interface have now become a structure determining part of a bimolecular self-assembled system.^{18,19}

Proposing a structural model for the monolayer based on the STM contrast is a crucial task, especially when the unit cell is rather large and contains more, possibly different molecules. Normally, the contrast is interpreted based on the geometry, size, and electronic structure of the adsorbed molecules, but high resolution images are required. In this study, we reproducibly observe different STM contrasts rather dependent on the specific tip than systematically on applied tunneling bias. Representative images obtained in nonanoic acid are depicted in Figure 3a–c; similar observations were made with the whole homologous series of fatty acids. For a given system, the lattice parameters are similar for all contrast types.

In analogy to the structure of previously observed bimolecular networks, an open pore structure with a periodic arrangement

of supramolecular cavities might be concluded from contrast I. However, it is significant that the walls which separate the putative cavities appear relatively thick compared to other open-pore networks. Contrast II is inverted with respect to I. Instead of apparent depressions, hexagonally arranged, 1.8 nm wide bright patches with a distinct 6-fold internal symmetry are observed. It is noteworthy that the size of both the dark features in contrast I and the bright features in II does not vary for the homologous row of solvents. Contrast III also consists of hexagonally arranged apparent depressions. However, as opposed to contrast I, the separating walls are better resolved and reveal internal features. As indicated in Figure 3c, each apparent depression is bordered by six bright bars. Again, these larger bars are comprised of four clearly discernible bright parallel elongated features, about 1 nm long for the nonanoic acid system. The internal parts are not as well resolved as in the case of contrast II, but still exhibit fine structure.

As the size of the putative cavities remains constant for all systems it is reasonable to assume that this part of the structure consists of the invariable compound, namely melamine. Size and symmetry is consistent with a melamine hexamer (1.8 nm in diameter) which is stabilized by 12 cyclical internal $N \cdots H-N$ hydrogen bonds and commonly found as a structure defining unit both in pure melamine monolayers¹¹ and bimolecular networks.⁶

Since the increment of the lattice parameter within the experimental error is similar to the length increment of the fatty acids it is reasonable to assume that the alkane tail is nearly aligned with the adsorbate lattice vector. Also, the size of the bright elongated features in contrast III corresponds to the size of the respective fatty acid for different structures.

A molecular model considering all requirements stated above is presented in Figure 5a. The basic unit is star shaped and consists of six internally hydrogen bonded melamine molecules which form a hexagonal core. Six pairs of fatty acid molecules are radially attached to this core via hydrogen bonds, while the $p6$ symmetry of the melamine core is preserved. The main contribution for the interaction between adjacent basic units arises from van der Waals interaction of aligned fatty acid molecules. The excellent agreement between the proposed model and the observed image contrast III is verified by the superposition depicted in Figure 5b. The respective orientation to the substrate is determined by alignment of all alkane backbones with the underlying graphite which further stabilizes the structure.²⁰

Recently, a very similar “pinwheel” structure was reported for coadsorption of melamine with PTCDI in a 4:3 ratio on Au(111).⁶ Likewise, a hydrogen bonded melamine hexamer is surrounded by six PTCDI molecules attached via hydrogen bonds. However, in the melamine + PTCDI “pinwheel” structure, PTCDI molecules are arranged nearly tangential to the melamine hexamer, whereas here the fatty acids point away radially from the center.

Also, the proposed model is consistent with the observed scaling behavior of the lattice parameter and explains the occurrence of the different contrasts: depending on the tip either the aromatic system of the melamine core (contrast II) or the aliphatic alkane tails of the fatty acids (contrast III) are observed. While normally in combined aliphatic and aromatic monolayers the aromatic moieties appear higher in constant current STM topographs,²¹ here, depending on the tip condition either melamine or fatty acid molecules are observed, but never both at the same time. Contrast I is also dominated by the fatty acid molecules, but due to poorer tip quality they cannot be resolved

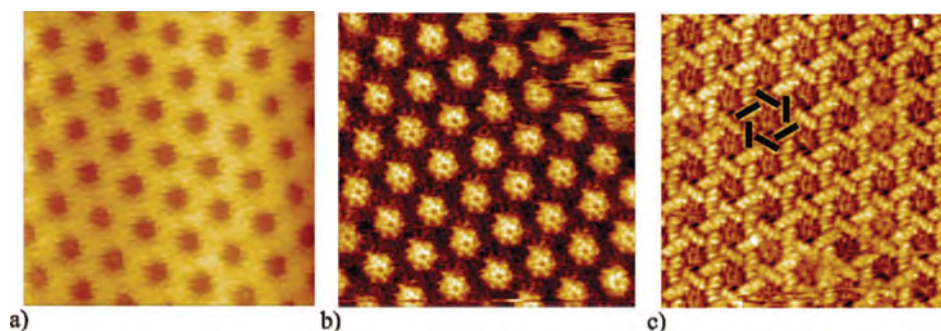


Figure 4. Three types of repeatedly observed contrasts, exemplified with the system melamine in nonanoic acid (all images $20 \times 20 \text{ nm}^2$): (a) type I was observed in most experimental runs ($U_T = 0.7 \text{ V}$, $I_T = 80 \text{ pA}$). (b) This particular tip or tip condition causes an apparent inversion, referred to as contrast II: instead of dark depressions a hexagonal arrangement of bright features with internal hexagonal symmetry is resolved ($U_T = 1.1 \text{ V}$, $I_T = 100 \text{ pA}$). (c) Contrast III provides higher resolution of the walls and reveals bright bars arranged in a “pinwheel” structure. Six of those bright bars border one dark depression as marked in the image ($U_T = 1.0 \text{ V}$, $I_T = 110 \text{ pA}$).

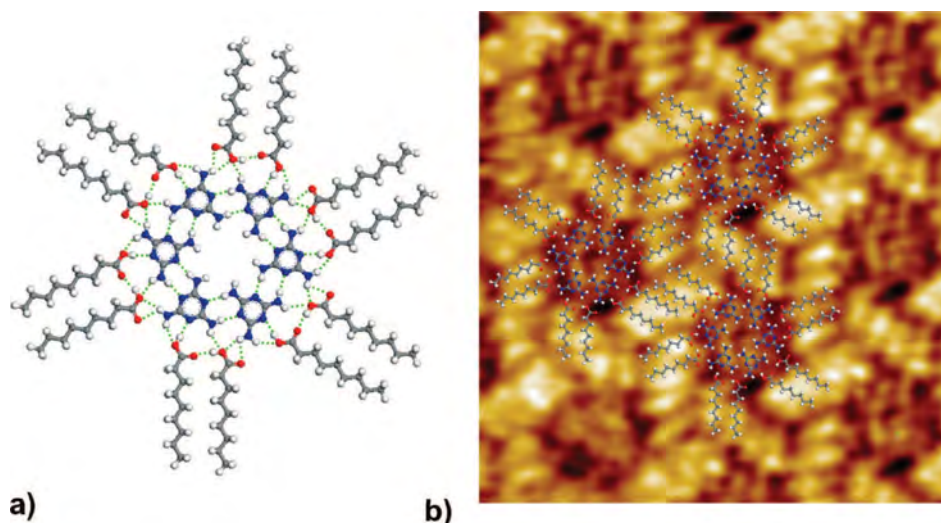


Figure 5. (a) Proposed molecular model of the bimolecular network of melamine and nonanoic acid. The symmetry defining connection point is composed of an internally hydrogen bonded melamine hexamer. Twelve fatty acid molecules are radially attached likewise via hydrogen bonds in six parallel pairs and account for the scalability of the system. Hydrogen bonds are indicated by dashed lines (b) full-scale overlay of the proposed model with the STM topograph (image size $13.8 \times 13.8 \text{ nm}^2$, $U_T = 1.0 \text{ V}$, $I_T = 110 \text{ pA}$).

individually as in case of contrast III. No systematic dependency of the contrast on tunneling parameters could be established. Bias dependent imaging with voltages from 0.1 to 1.2 V does not yield different contrasts, while at higher voltages the tunneling current becomes unstable. Yet, erratic switching between contrast I and II frequently occurs, thereby indicating that tip termination is more decisive for the contrast than tunneling voltage.

Although force-field calculations neglect and oversimplify important interactions, they are still a valuable method to compare and discuss the relative energetics, particularly for these isotopological networks where similar molecules and interactions are involved. For the calculation experimentally determined unit cells serve as a constraint and due to the explicit treatment of hydrogen bonds, the Dreiding force-field was used.²² In order to apply periodic boundary conditions, all unit cells were assumed to be commensurate and convergence could be achieved for all systems. The graphite substrate was approximated by two layers with the atomic positions in the lower layer fixed. An example for an energy optimized melamine + nonanoic acid structure is depicted in Figure 6 (cf. Supporting Information for all other systems). The melamine–melamine and melamine–fatty acid interactions are dominated by hydrogen bonds and obviously remain constant in all systems. In contrast, the fatty acid–fatty acid and fatty acid–graphite interac-

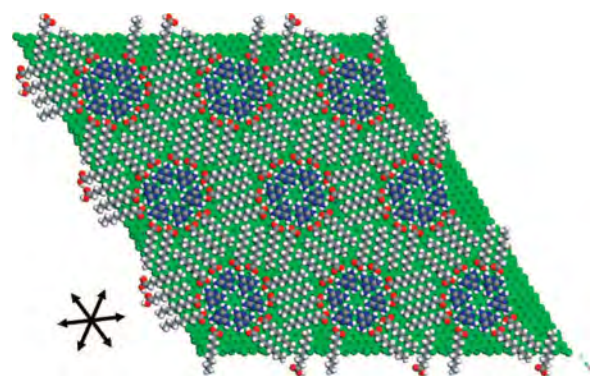


Figure 6. Force-field simulation of the system melamine and nonanoic acid, the cut-out depicts 3×3 unit cells. Experimentally determined unit cell parameters serve as a constraint and are approximated by a commensurate superstructure matrix in order to facilitate periodic boundary conditions. The main axes of the graphite substrate are indicated in the lower left corner.

tions which are mainly van der Waals type are chain length dependent. Consequently, as can be seen in Figure 7a, the total binding energy per unit cell (E_{UC}) increases linearly with carbon count. This behavior can be understood by decomposing the total binding energy into its various contributions: the number of melamine molecules per unit cell, thus their contribution to

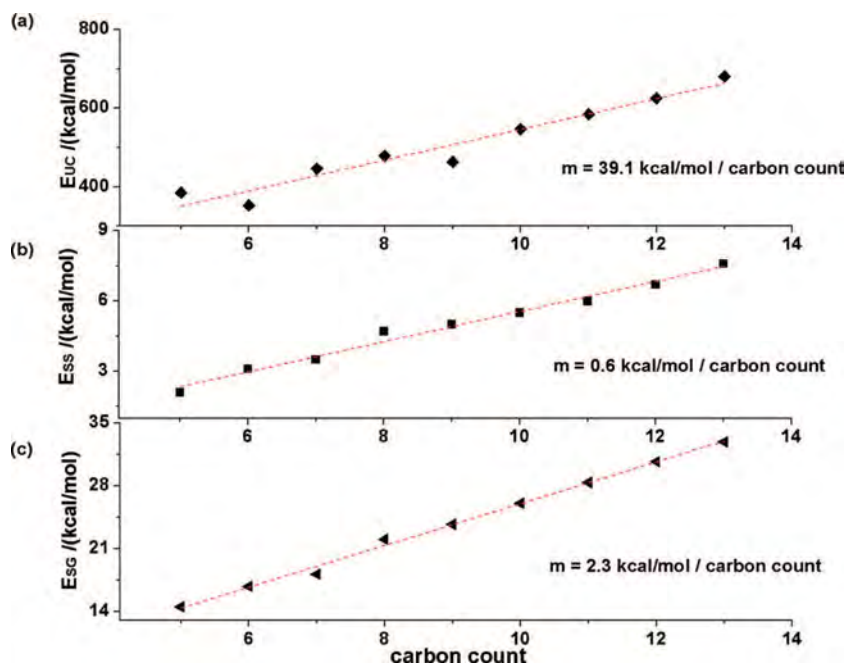


Figure 7. Absolute binding energies derived by force-field calculations as a function of fatty acid chain length (carbon count). Dashed red lines represent linear fits and respective slopes are denoted. (a) Total binding energy per unit cell E_{UC} , i.e., the sum of all molecule–substrate and molecule–molecule interactions, of the melamine + fatty acid system per unit cell. Only the contributions analyzed in more detail in (b) and (c) are dependent on carbon count and account for the linear increase. Melamine related contributions remain constant for all systems. (b) Interaction energy of two geometry optimized solvent molecules E_{SS} in head-to-tail arrangement. The pure van der Waals interaction also exhibits a linear increase with a slope of 0.6 kcal/mol/carbon count. (c) Adsorption energy E_{SG} of a single, geometry optimized fatty acid molecule on graphite. The increase per carbon count was determined to be 2.3 kcal/mol

the adhesion energy and the number of hydrogen bonds does not depend on the specific solvent applied. However, both the intermolecular binding energy and the adsorption energy of the fatty acid molecules increase linearly with chain length. Therefore, the linear increase in total binding energy is caused by the fatty acid molecules. In order to verify this hypothesis, the interaction energy of two parallel aligned fatty acid molecules (E_{SS}) and the adsorption energies of a single fatty acid molecule (E_{SG}) were calculated as a function of carbon count as well, results are depicted in Figure 7, panels b and c. From the calculation it becomes clear that the adsorption energies of the fatty acid molecules are significantly larger than the intermolecular van der Waals binding energies. However, as illustrated in Figure 5a, the fatty acids are also stabilized through a network of hydrogen bonds with the melamine hexamers. The respective binding energy of a pair of fatty acids to the melamine core accounts to 10 kcal/mol. This value is still higher than the 7.8 kcal/mol stabilization energy reported for a melamine dimer by Xu et al.⁹ This strong binding between the radial pairs of fatty acids and the melamine hexamer is likely to drive and cause self-assembly of a binary system.

In summary, the total binding energy can be divided into solvent dependent and independent contributions: Independent contributions are melamine–melamine, melamine–substrate, and melamine–fatty acid interactions and remain virtually constant for all solvents. Dependent contributions are fatty acid–fatty acid and fatty acid–substrate interactions and increase linearly with carbon count. Because the lattice parameters and the binding energies per unit cell increase linearly, the binding energies per unit area decrease with one over carbon count, which should render these bimolecular networks thermodynamically unstable for increasing carbon count relative to competing structures such as pure fatty acid monolayers.

In this study the formation of similar bimolecular monolayers of melamine with members of the homologous series of fatty

acids from pentanoic through tridecanoic acid was observed at the liquid-graphite interface. All systems yielded hexagonal structures where the lattice parameter increases linearly with the number of carbon atoms in the fatty acid. The structures are isotopological in the sense that they follow the same building plan: invariant connection points comprised of melamine hexamers account for the hexagonal symmetry. Interconnects of variable length are realized by groups of four fatty acid molecules, where two molecules are hydrogen bonded to the respective connection point and the pairs are held together by van der Waals interaction.

It would be highly interesting to investigate whether the scaling behavior holds for even longer fatty acid molecules. However, their melting point also increases with chain length and stable tunneling conditions could not be achieved for higher fatty acids. Since the melamine hexamers represent a hexagonal arrangement of equally sized aromatic patches in an aliphatic matrix where the next nearest neighbor distance can be fine-tuned in steps of 0.15 nm, it might stimulate further experiments: through selective adsorption of appropriately functionalized nanoparticles, these isotopological networks may act as a structured template which allows for instance to investigate particle–particle interaction as a function of distance with high resolution.

Acknowledgment. We gratefully acknowledge financial support by the Deutsche Forschungsgemeinschaft (SFB 486), the Bayerische Forschungsförderung, and the Nanosystems Initiative Munich (NIM).

Supporting Information Available: Experimental details, STM topographs, unit cell parameters, and force-field calculations of all nine isotopological networks. This material is available free of charge via the Internet at <http://pubs.acs.org>.

References and Notes

- (1) Eddaoudi, M.; Kim, J.; Rosi, N.; Vodak, D.; Wachter, J.; O'Keeffe, M.; Yaghi, O. M. *Science* **2002**, 295 (5554), 469–472.
- (2) Yaghi, O. M.; O'Keeffe, M.; Ockwig, N. W.; Chae, H. K.; Eddaoudi, M.; Kim, J. *Nature* **2003**, 423 (6941), 705–714.
- (3) Schickum, U.; Decker, R.; Klappenberger, F.; Zoppellaro, G.; Klyatskaya, S.; Ruben, M.; Silanes, I.; Arnau, A.; Kern, K.; Brune, H.; Barth, J. V. *Nano Lett.* **2007**, 7 (12), 3813–3817.
- (4) Theobald, J. A.; Oxtoby, N. S.; Phillips, M. A.; Champness, N. R.; Beton, P. H. *Nature* **2003**, 424 (6952), 1029–1031.
- (5) Silly, F.; Shaw, A. Q.; Porfyrakis, K.; Briggs, G. A. D.; Castell, M. R. *Appl. Phys. Lett.* **2007**, 91 (25), 251101.
- (6) Silly, F.; Shaw, A. Q.; Castell, M. R.; Briggs, G. A. D. *Chem. Commun.* **2008**, (16), 1907–1909.
- (7) Silly, F.; Weber, U. K.; Shaw, A. Q.; Burlakov, V. M.; Castell, M. R.; Briggs, G. A. D.; Pettifor, D. G. *Phys. Rev. B* **2008**, 77 (20), 200401.
- (8) Perdigo, L.; Champness, N.; Beton, P. *Chem. Commun.* **2006**, (5), 538–540.
- (9) Xu, W.; Dong, M. D.; Gersen, H.; Rauls, E.; Vazquez-Campos, S.; Crego-Calama, M.; Reinhoudt, D. N.; Stensgaard, I.; Laegsgaard, E.; Linderoth, T. R.; Besenbacher, F. *Small* **2007**, 3 (5), 854–858.
- (10) Kannappan, K.; Werblowsky, T. L.; Rim, K. T.; Berne, B. J.; Flynn, G. W. *J. Phys. Chem. B* **2007**, 111 (24), 6634–6642.
- (11) Silly, F.; Shaw, A. Q.; Castell, M. R.; Briggs, G. A. D.; Mura, M.; Martsinovich, N.; Kantorovich, L. *J. Phys. Chem. C* **2008**, 112 (30), 11476–11480.
- (12) Zhang, H. M.; Xie, Z. X.; Long, L. S.; Zhong, H. P.; Zhao, W.; Mao, B. W.; Xu, X.; Zheng, L. S. *J. Phys. Chem. C* **2008**, 112 (11), 4209–4218.
- (13) Kampschulte, L.; Werblowsky, T. L.; Ravuri, S. K. K.; Schmittel, M.; Heckl, W. A.; Lackinger, M. *J. Am. Chem. Soc.* **2008**, 130 (26), 8502–8507.
- (14) Etter, M. C.; Admond, D. A. *Chem. Commun.* **1990**, (8), 589–591.
- (15) Cai, Y. G.; Bernasek, S. L. *J. Am. Chem. Soc.* **2004**, 126 (43), 14234–14238.
- (16) Zhang, H. M.; Yan, J. W.; Xie, Z. X.; Mao, B. W.; Xu, X. *Chem.–Eur. J.* **2006**, 12 (15), 4006–4013.
- (17) Yang, T.; Berber, S.; Liu, J. F.; Miller, G. P.; Tomanek, D. *J. Chem. Phys.* **2008**, 128 (12), 124701.
- (18) Tahara, K.; Furukawa, S.; Uji-I, H.; Uchino, T.; Ichikawa, T.; Zhang, J.; Mamdouh, W.; Sonoda, M.; De Schryver, F. C.; De Feyter, S.; Tobe, Y. *J. Am. Chem. Soc.* **2006**, 128 (51), 16613–16625.
- (19) Mamdouh, W.; Uji-i, H.; Ladislav, J. S.; Dulcey, A. E.; Percec, V.; De Schryver, F. C.; De Feyter, S. *J. Am. Chem. Soc.* **2006**, 128 (1), 317–325.
- (20) Yin, S. X.; Wang, C.; Xu, Q. M.; Lei, S. B.; Wan, L. J.; Bai, C. L. *Chem. Phys. Lett.* **2001**, 348 (3–4), 321–328.
- (21) Lei, S. B.; Yin, S. X.; Wang, C.; Wan, L. J.; Bai, C. L. *Chem. Mater.* **2002**, 14 (7), 2837–2841.
- (22) Mayo, S. L.; Olafson, B. D.; Goddard, W. A. *J. Phys. Chem.* **1990**, 94 (26), 8897–8909.

JP8078474

Supporting Information:

Isotopological supramolecular networks from melamine and fatty acids

Hermann Walch¹, Anne-Kathrin Maier¹, Wolfgang M. Heckl^{1,2}, and Markus Lackinger¹

¹Ludwig-Maximilians-University Munich, Department for Earth and Environmental Sciences and
Center for NanoScience (CeNS), Theresienstr. 41, D-80333 München, Germany;

²Deutsches Museum, Museumsinsel 1, D-80538 München, Germany

**RECEIVED DATE (to be automatically inserted after your manuscript is accepted if required
according to the journal that you are submitting your paper to)**

Table 1: Lattice parameters of the bimolecular melamine + fatty acid monolayers on graphite for all investigated members of the homologous series from pentanoic acid through tridecanoic acid; fatty acids marked with asterisks are solid at room temperature.

fatty acid	experiment		calculation	
	a (nm)	γ	a (nm)	γ
pentanoic	2.85	120.9°	2.98	120.0°
hexanoic	3.00	119.1°	2.99	120.0°
heptanoic	3.22	119.0°	3.23	120.0°
octanoic	3.30	121.2°	3.44	120.0°
nonanoic	3.50	118.9°	3.47	120.0°
decanoic*	3.65	121.2°	3.69	120.0°
undecanoic*	3.80	120.8°	3.79	120.0°
dodecanoic*	3.95	121.1°	3.94	120.0°
tridecanoic*	4.05	121.9°	4.09	120.0°

2nd and 3rd column: experimental lattice parameters as deduced from STM calibration images;

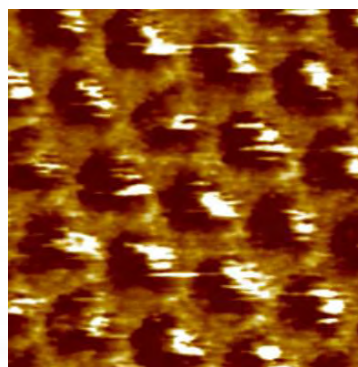
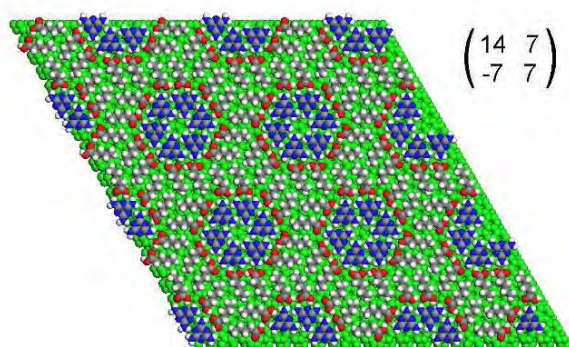
4th and 5th column: lattice parameters as applied for the force-field calculations;

In order to facilitate periodic boundary conditions for the force-field calculations the experimental unit cells are approximated by hexagonal commensurate super structures, i.e. all superstructure matrix elements are integers, while the orientation of the adsorbate lattice vectors with respect to the graphite lattice was maintained within $\pm 3^\circ$.

Fig. S1: Force-field calculations and STM topographs of all bimolecular melamine + fatty acid monolayers investigated;

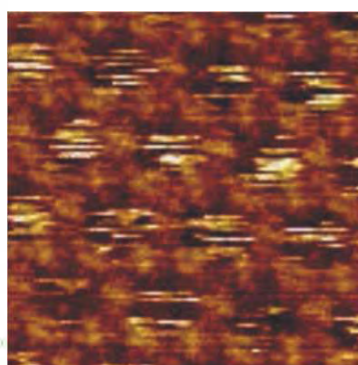
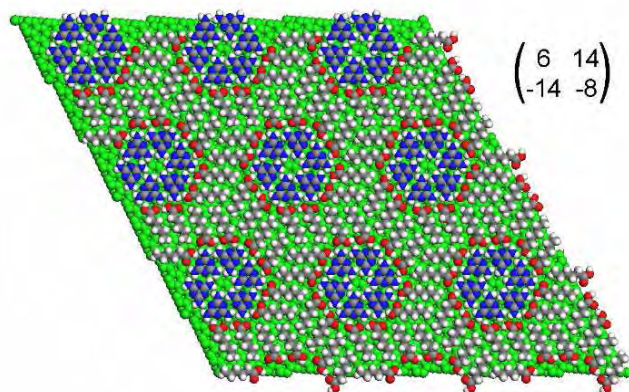
left hand side: energy minimized structures according to force-field calculations with periodic boundary conditions and the Dreiding II force-field. Values in parenthesis state the corresponding superstructure matrix with the graphite lattice as basis. All unit cells contain in total 18 molecules (6 melamine + 12 fatty acid molecules) **right hand side:** STM topographs of the respective bimolecular monolayers (all images 12 x 12 nm²)

(a) melamine + pentanoic acid



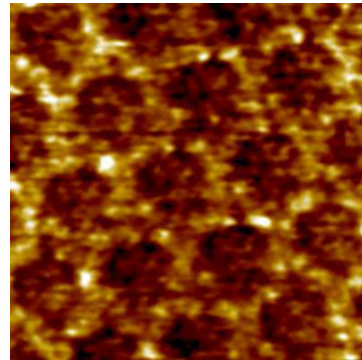
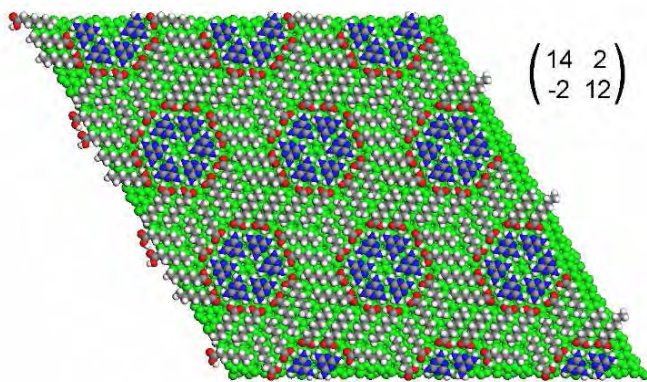
tunneling parameters: $U_T=1.0$ V, $I_T=70$ pA

(b) melamine + hexanoic acid



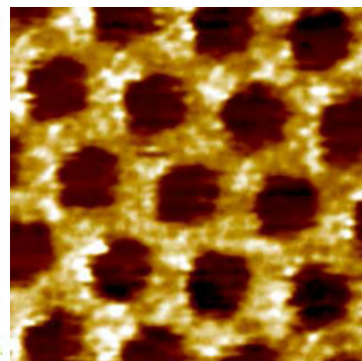
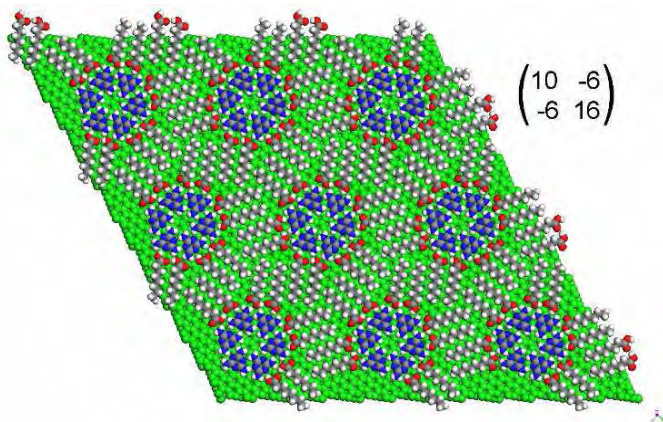
tunneling parameters: $U_T=0.80$ V, $I_T=80$ pA

(c) melamine + heptanoic acid



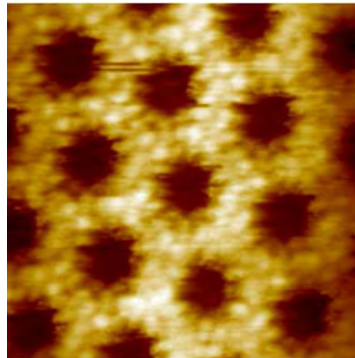
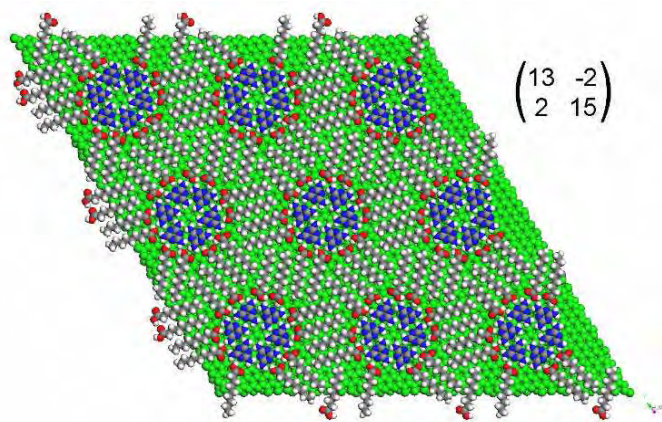
tunneling parameters: $U_T=0.70$ V, $I_T=150$ pA

(d) melamine + octanoic acid



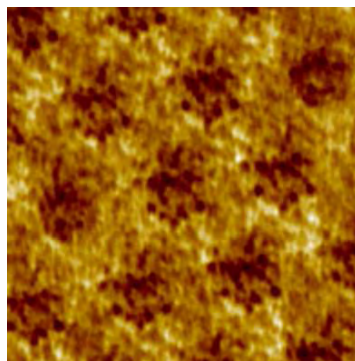
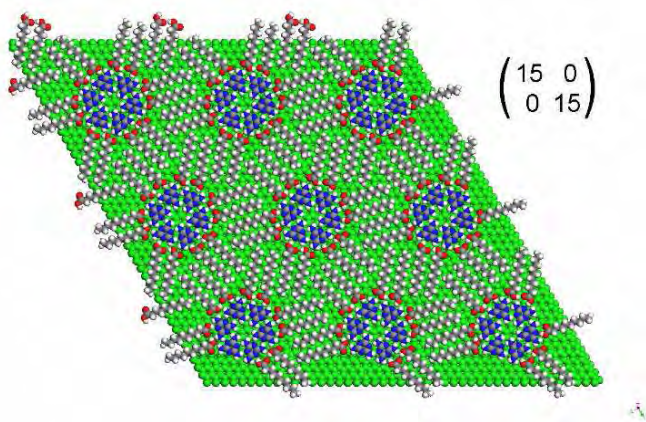
tunneling parameters: $U_T=1.0$ V, $I_T=65$ pA

(e) melamine + nonanoic acid



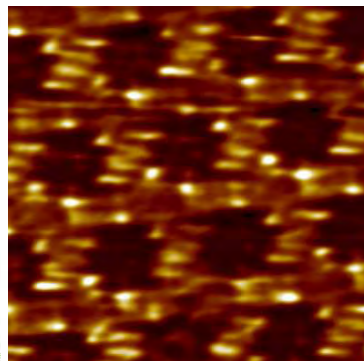
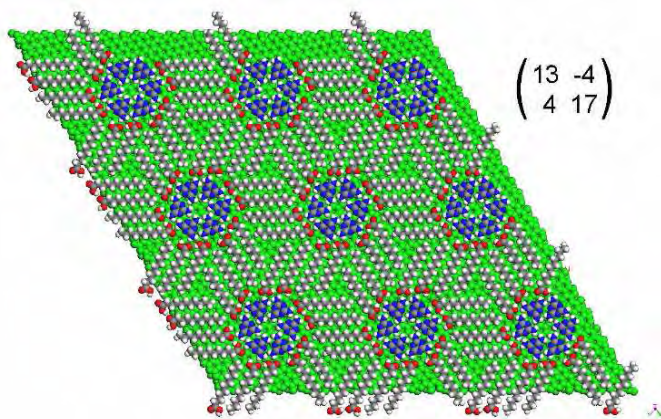
tunneling parameters: $U_T=0.70$ V, $I_T=80$ pA

(f) melamine + decanoic acid



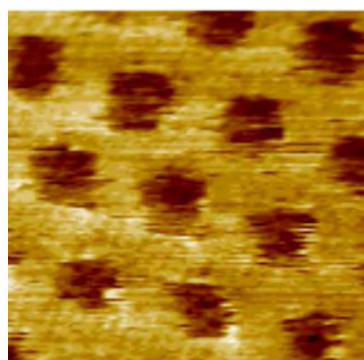
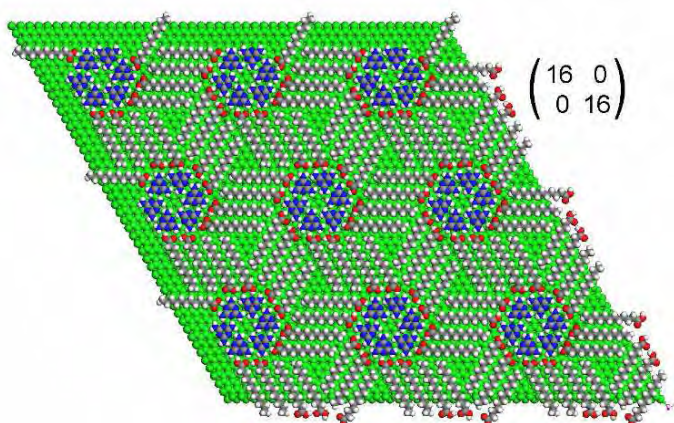
tunneling parameters: $U_T=0.80$ V, $I_T=90$ pA

(g) melamine + undecanoic acid



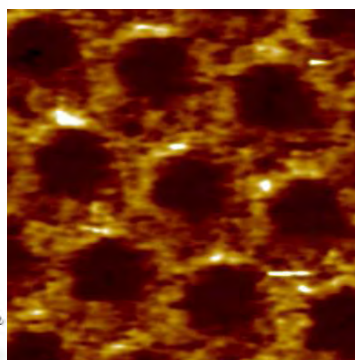
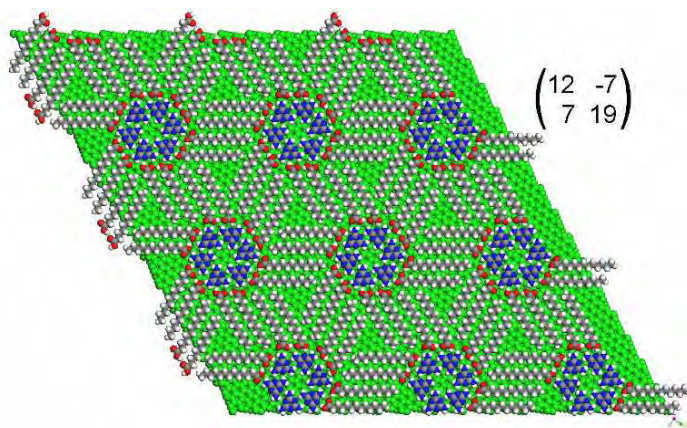
tunneling parameters: $U_T=0.80$ V, $I_T=75$ pA

(h) melamine + dodecanoic acid



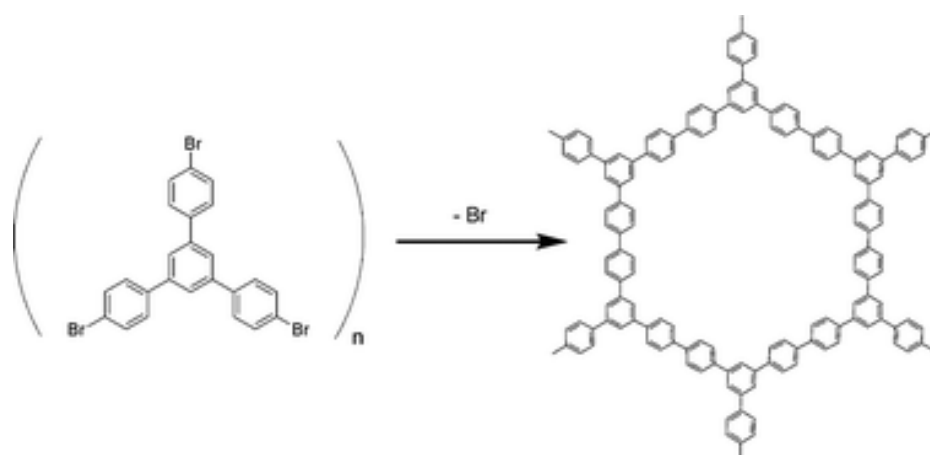
tunneling parameters: $U_T=0.90$ V, $I_T=40$ pA

(i) melamine + tridecanoic acid



tunneling parameters: $U_T=0.50$ V, $I_T=100$ pA

6.2 Surface mediated synthesis of 2D covalent organic frameworks:
1,3,5-tris(4-bromophenyl)benzene on
graphite(001), Cu(111), and Ag(110)



Chem. Commun., **2009**, 4456 - 4458

Rico Gutzler, Hermann Walch, Georg Eder, Stephan Kloft, Wolfgang M. Heckl and Markus Lackinger

Surface mediated synthesis of 2D covalent organic frameworks: 1,3,5-tris(4-bromophenyl)benzene on graphite(001), Cu(111), and Ag(110)†

Rico Gutzler,^{*a} Hermann Walch,^a Georg Eder,^a Stephan Kloft,^a Wolfgang M. Heckl^{ab} and Markus Lackinger^{*a}

Received (in Cambridge, UK) 7th April 2009, Accepted 28th May 2009

First published as an Advance Article on the web 12th June 2009

DOI: 10.1039/b906836h

The on surface synthesis of a two-dimensional (2D) covalent organic framework from a halogenated aromatic monomer under ultra-high vacuum conditions is shown to be dependent on the choice of substrate.

The synthesis of 2D covalent organic frameworks (COF) on surfaces has recently gained much attention.¹ Commonly, these novel polymers are built by sublimation of appropriate monomers onto metallic substrates under ultra-high vacuum (UHV) conditions and subsequent annealing.^{2–6} Many other studies investigated the formation of covalent structures from smaller building blocks and demonstrated the importance of the substrate both for the confinement of molecular motion in two dimensions and as a catalyst for activation.^{7–10}

Here, we report on the reticular synthesis of 2D COFs built up from conjugated subunits (phenyl rings) only. The halogen substituted polyaromatic monomer is thermally sublimed onto various substrates under UHV conditions at room temperature. Without providing additional activation energy, the formation of radicals is observed on Cu(111) and Ag(110). Deposition of the same compound on graphite(001) results in non-covalent self-assembly of well ordered networks stabilized by halogen–hydrogen bonds. These results demonstrate the decisive role of the substrate for homolysis of covalent carbon–halogen bonds at room temperature and subsequent association of radicals.

Our strategy for the synthesis of 2D COFs consists of the deposition of a suitable organic compound and its subsequent substrate mediated homolysis. Intermolecular colligation occurs through radical addition at elevated temperatures. For formation of 2D open-pore networks from a single kind of molecule the building block must at least be a triradical, *i.e.* exhibit three potential binding sites. Comparatively weak carbon–halogen bonds are well suited as predetermined breaking points and from solution chemistry Cu catalysts are known to facilitate homolysis.¹¹ The molecule of choice is 1,3,5-tris(4-bromophenyl)benzene (TBB, *cf.* Fig. 1a). TBB is an appropriate candidate because the homolytic bond dissociation

energy of its C–Br bonds (3.2 eV) is substantially lower than that of the C–C link between phenyl rings (4.8 eV).^{12,13}

Evaporation of a TBB monolayer on graphite(001) results in an ordered structure (*cf.* Fig. 1b and c). Although no submolecular resolution is achieved, the long range order and the mutual arrangement of molecules within the monolayer indicate non-covalent self-assembly of intact TBB molecules.

In agreement with molecular mechanics simulations, molecules arrange in chains of dimers which are stabilized by Br···H–C hydrogen bonds. Similar binding motifs have been reported for comparable systems^{14–16} and also stabilize the bulk structure of TBB.¹⁷ The contrast modulation, *i.e.* every other row appears brighter, is caused by different adsorption sites on the graphite lattice. Annealing of the graphite sample to ~320 °C for 10 min results in complete desorption of the TBB monolayer, thereby demonstrating the inferior stability of this non-covalent network.

Open-pore networks can clearly be identified in the STM topographs obtained for submonolayer coverage of TBB on Cu(111) (Fig. 2) and Ag(110) (*cf.* Fig. S1, ESI†). These

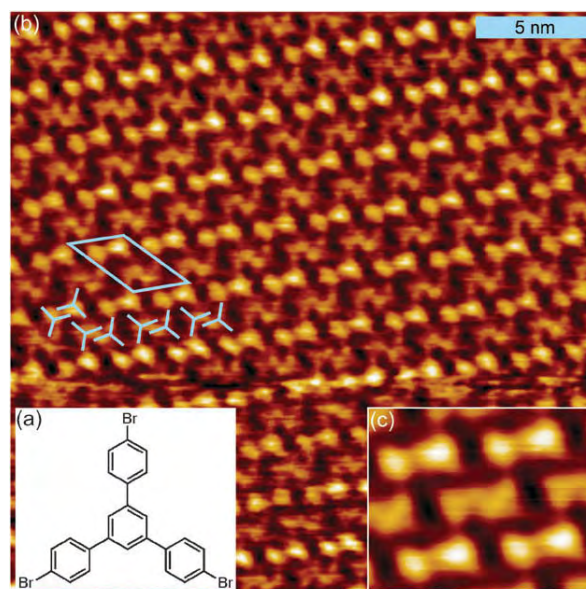


Fig. 1 (a) Structure of 1,3,5-tris(4-bromophenyl)benzene (TBB). (b) STM topograph of a TBB monolayer on graphite ($V = 1.9$ V, $I = 76$ pA). Unit cell is indicated by blue lines ($a = 3.4$ nm, $b = 2.5$ nm, $\alpha = 44^\circ$) and accommodates four molecules, symbolized by blue tripods. (c) Mesh-averaged image (4.1×5.0 nm²) of (b).

^a Department of Earth and Environmental Sciences and Center for NanoScience (CeNS), Ludwig-Maximilians-University, Theresienstrasse 41, 80333, Munich, Germany.

E-mail: rico.gutzler@lrz.uni-muenchen.de, markus@lackinger.org; Tel: +49 89 21804317

^b Deutsches Museum, Museumsinsel 1, 80538, Munich, Germany

† Electronic supplementary information (ESI) available: Experimental details, calculations, thermogravimetric analysis, additional STM data, and UV/Vis spectra. See DOI: 10.1039/b906836h

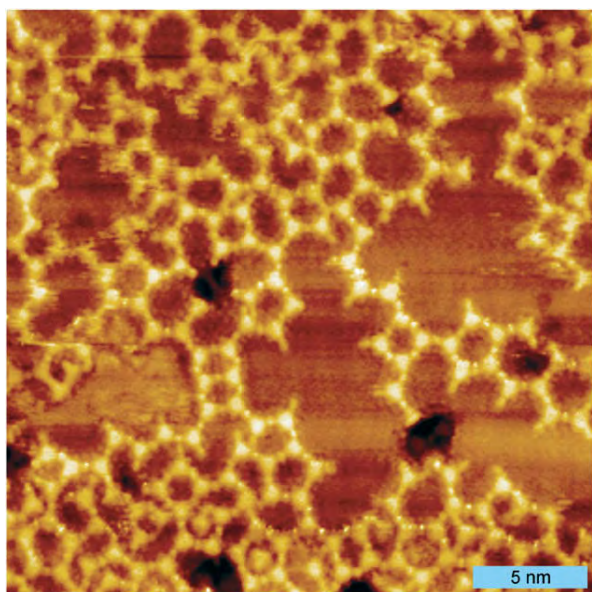


Fig. 2 TBB protopolymer on Cu(111) before annealing ($V = -1.85$ V, $I = 248$ pA). Spherical protrusions between radicals are clearly observable.

networks are composed of polygons, predominantly hexagons and pentagons but also heptagons, octagons and other polygons. The experimentally determined values for the center-to-center distance between adjacent molecules for room temperature deposition are $1.49 \text{ nm} \pm 0.10 \text{ nm}$ for Cu(111) and $1.57 \text{ nm} \pm 0.06 \text{ nm}$ for Ag(110) and are equal for both substrates within the error margin. These values are somewhat larger than anticipated for a covalent C–C link between adjacent molecules. In the topograph of the TBB network on Cu(111) (Fig. 2), bright protrusions can clearly be discerned between adjacent molecules. These spherical features are attributed to single copper atoms which coordinate two or occasionally three radicals. Similar systems based on halogenated benzene derivatives were reported to assemble in a first step into so-called protopolymers where two radicals are linked *via* a metal atom.^{7,18} This preceding formation of a metal coordination complex between on surface-generated radicals and substrate atoms is also likely to be observed here. Coordinating atoms could not be resolved on Ag(110), but the spacing clearly indicates formation of protopolymers as well. In this respect, no difference between the two metal substrates was found, although (110) surfaces exhibit a pronounced anisotropy. In most cases the network structures are attached to step edges, hence it is probable that growth is initiated by attachment of a free radical to a step edge (Fig. S1, ESI†).

In order to verify whether protopolymers can eventually be converted into COFs, annealing experiments have been carried out with the Cu(111) surface. Fig. 3a depicts an STM topograph of a tempered sample. After annealing to $300 \text{ }^\circ\text{C}$ the distance between two interconnected molecules is reduced to $1.24 \text{ nm} \pm 0.06 \text{ nm}$ (Fig. 3a). Accordingly, the linescan in Fig. 3b yields a size of 2.2 nm for each hexagon. The STM contrast of the network after annealing at $300 \text{ }^\circ\text{C}$ (Fig. 3a) is very different from the network before annealing (Fig. 2). The bright features in between two molecules are absent in the

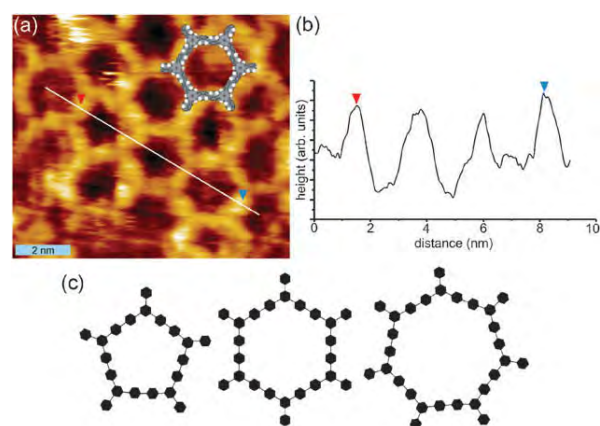


Fig. 3 TBB covalent organic framework on Cu(111) (a) evaporation temperature of $140 \text{ }^\circ\text{C}$ for 8 minutes ($V = +3.2$ V, $I = 233$ pA) and subsequent annealing to $300 \text{ }^\circ\text{C}$. A scaled hexagonal ring is overlaid. (b) Linescan as indicated in (a) across three rings yielding a center-to-center distance of 2.2 nm for a single ring. (c) Principally encountered binding motifs: pentagon, hexagon and heptagon. Bonds between phenyl rings are distorted by $\Delta\alpha$.

post-annealing topograph, indicating a physical change in the monolayer. More importantly, the reduced size (both the lattice constant and the spacing of adjacent molecules) upon annealing indicates the transition from a protopolymer to a 2D COF. Lipton-Duffin *et al.* found for polymerization experiments with *p*-diiodobenzene that the phenyl–phenyl spacing is reduced by 0.12 nm upon transition from a protopolymer to an actual covalent linkage.⁷ This value is consistent with our observations. The necessity of an additional annealing step to finally induce covalent linkage was also experienced by other groups for comparable systems.^{7,19}

The distance between two monomers in the post-annealing network is also in accordance with both DFT and molecular mechanics simulations of an infinite layer of TBB molecules covalently linked at the 4'-position (1.28 nm , experimental: $1.24 \text{ nm} \pm 0.06 \text{ nm}$). A hypothetical hexagonal network based on intact TBB subunits pointing head-to-head with their bromine atoms would necessarily result in a considerably larger center-to-center distance of $\sim 1.75 \text{ nm}$ as estimated by molecular mechanics calculations and can thus be excluded.

The high defect density, that is the frequent occurrence of polygons different from hexagons, can be explained by considering the energy necessary to bend one bond between two phenyl groups: due to the threefold symmetry of TBB, a hexagonal ring comprising six molecules would yield the lowest-energy geometry because all newly formed links exhibited an ideal bonding angle of 180° . All other polygons experience slightly higher stress due to distortion of the bond angle. Assuming regularity and rigid phenyl rings, each bond between two phenyl rings in the polygon is distorted from its optimal equilibrium angle on average by $\Delta\alpha = 60^\circ(6 - N)/(3N)$, where N is the number of molecules in the ring (Fig. 3c). The change $\Delta\alpha$ is small and accounts to 4° , 0° , and -2.9° for pentagon, hexagon, and heptagon, respectively, yielding only a small additional energy contribution. This small deviation from the equilibrium geometry is responsible for the high number of polygons different from hexagons. Since colligation of free

radicals is virtually barrier free and only diffusion limited, kinetic effects can result in suboptimal binding geometries where the binding angle can deviate from 180°. This leads to a reduced order and high defect densities.

Interestingly, the chemical activity of the substrate has a major contribution to cleavage of the C–Br bond. The activation of TBB molecules, that is generation of triple radicals by cleavage of all three covalent C–Br bonds, requires a metallic substrate. In general, the binding energy of halides chemisorbed to metal surfaces is particularly strong and was found to be in the order of 1.5 eV. Thus, a low free energy of the final state certainly promotes homolytic fission of C–Br bonds in TBB. Physisorption of halides on graphite would render homolysis strongly endothermic. In some STM topographs on metal surfaces, circular features appear after deposition of TBB and can be attributed to adsorbed Br atoms.

For the likewise covalently linked structures prepared from Br substituted tetraphenyl porphyrins and dibromoterfluorene on catalytically less active Au(111) surfaces, significantly higher temperature thresholds of 315 °C and 250 °C for thermal activation are reported.^{2,20} The first compound is much heavier than TBB and the temperature for bond cleavage is in the regime of the sublimation temperature, thus activation can already occur in the crucible. In contrast, for TBB thermal evaporation of non-activated species is easily possible. The distinct substrate dependence clearly demonstrates that homolysis takes place on the surface and not in the crucible as observed for other systems.^{2,6} Furthermore, UV/Vis spectroscopy independently confirms that the TBB molecules are intact prior to sorption on the surface and do not dissociate at the sublimation temperatures of 140–160 °C (*cf.* ESI†).

Thermal stability of the COFs on Cu(111) has been verified by further annealing experiments and subsequent STM characterization. Annealing of the Cu(111) sample at 400 °C caused degradation of the networks and STM images no longer exhibit open-pore structures (see Fig. S2, ESI†, for a degraded network). Thermogravimetric analysis of pure TBB reveals an onset for decomposition at a temperature of around 250 °C (*cf.* ESI†), which is somewhat lower than for the COF. Its higher thermal stability can be attributed to the absence of comparatively weak C–Br bonds in the monolayer, strong intermolecular bonds, and interaction with the substrate.

In this work, we demonstrate the formation of substrate supported 2D COFs by addition of on surface-generated triple radicals. Experiments on different surfaces unveil the important role of the substrate for the main activation step, homolytic fission of C–Br bonds. On metal substrates where the split-off Br-atoms are stabilized by strong chemisorption, homolysis takes place without providing additional activation

energy. Chemically inert graphite surfaces cannot promote homolysis, thus cannot initiate formation of covalent bonds. However, due to preceding formation of a protopolymer through metal coordination of radicals, an additional thermal activation is required to transfer the networks eventually into COFs. In this respect it would be highly interesting to find either a system, a method, or conditions where on one hand the substrate is catalytically effective for homolysis but on the other hand formation of protopolymers is suppressed. The immediate formation of covalent bonds would definitely change the association kinetics and will thus possibly also influence the ordering.

Financial support by Deutsche Forschungsgemeinschaft (SFB 486) and Nanosystems Initiative Munich (NIM) is gratefully acknowledged. Georg Eder acknowledges support by the Hanns-Seidel-Stiftung.

Notes and references

- 1 D. F. Perepichka and F. Rosei, *Science*, 2009, **323**, 216–217.
- 2 L. Grill, M. Dyer, L. Lafferentz, M. Persson, M. V. Peters and S. Hecht, *Nat. Nanotechnol.*, 2007, **2**, 687–691.
- 3 M. Treier, N. V. Richardson and R. Fasel, *J. Am. Chem. Soc.*, 2008, **130**, 14054–14055.
- 4 M. In't Veld, P. Iavicoli, S. Haq, D. B. Amabilino and R. Raval, *Chem. Commun.*, 2008, 1536–1538.
- 5 S. Weigelt, C. Busse, C. Bombis, M. M. Knudsen, K. V. Gothelf, E. Laegsgaard, F. Besenbacher and T. R. Linderth, *Angew. Chem., Int. Ed.*, 2008, **47**, 4406–4410.
- 6 N. A. A. Zwaneveld, R. Pawlak, M. Abel, D. Catalin, D. Gignes, D. Bertin and L. Porte, *J. Am. Chem. Soc.*, 2008, **130**, 6678–6679.
- 7 J. A. Lipton-Duffin, O. Ivasenko, D. F. Perepichka and F. Rosei, *Small*, 2009, **5**, 592–597.
- 8 M. Matena, T. Riehm, M. Stöhr, T. A. Jung and L. H. Gade, *Angew. Chem., Int. Ed.*, 2008, **47**, 2414–2417.
- 9 S. Weigelt, C. Bombis, C. Busse, M. M. Knudsen, K. V. Gothelf, E. Laegsgaard, F. Besenbacher and T. R. Linderth, *ACS Nano*, 2008, **2**, 651–660.
- 10 S. Weigelt, J. Schnadt, A. K. Tuxen, F. Masini, C. Bombis, C. Busse, C. Isvoranu, E. Ataman, E. Laegsgaard, F. Besenbacher and T. R. Linderth, *J. Am. Chem. Soc.*, 2008, **130**, 5388–5389.
- 11 S. V. Ley and A. W. Thomas, *Angew. Chem., Int. Ed.*, 2003, **42**, 5400–5449.
- 12 R. J. Kominar, M. J. Krech and S. J. W. Price, *Can. J. Chem.*, 1978, **56**, 1589–1592.
- 13 M. Szwarc, *Nature*, 1948, **161**, 890–891.
- 14 G. R. Desiraju and R. Parthasarathy, *J. Am. Chem. Soc.*, 1989, **111**, 8725–8726.
- 15 H. F. Lieberman, R. J. Davey and D. M. T. Newsham, *Chem. Mater.*, 2000, **12**, 490–494.
- 16 O. Navon, J. Bernstein and V. Khodorkovsky, *Angew. Chem., Int. Ed. Engl.*, 1997, **36**, 601–603.
- 17 L. M. C. Beltran, C. Cui, D. H. Leung, J. Xu and F. J. Hollander, *Acta Crystallogr., Sect. E*, 2002, **58**, O782–O783.
- 18 G. S. McCarty and P. S. Weiss, *J. Am. Chem. Soc.*, 2004, **126**, 16772–16776.
- 19 M. Xi and B. E. Bent, *Surf. Sci.*, 1992, **278**, 19–32.
- 20 L. Lafferentz, F. Ample, H. Yu, S. Hecht, C. Joachim and L. Grill, *Science*, 2009, **323**, 1193–1197.

Supporting Information

Substrate Mediated Synthesis of 2D Covalent Organic Frameworks

Rico Gutzler^{*a}, Hermann Walch^a, Georg Eder^a, Stephan Kloft^a, Wolfgang M. Heckl^{a,b}, and Markus Lackinger^a

Department of Earth and Environmental Sciences and Center for NanoScience (CeNS), Ludwig-Maximilians-University, Theresienstrasse 41, 80333 Munich, Germany; Deutsches Museum, Museumsinsel 1, 80538 Munich, Germany

Contents

- I. Experimental procedures**
- II. Additional STM data**
- III. Forcefield and DFT calculations**
- IV. Thermo gravimetric analysis**
- V. UV/Vis Spectra**

I. Experimental procedures

All experiments are carried out under UHV conditions (base pressure $<5.0 \times 10^{-10}$ mbar) at room temperature with two different STMs. One instrument is a commercial STM from Omicron whereas the other one a home-built beetle type STM as described elsewhere.¹ Both STMs are laterally calibrated by atomically resolved graphite images. 1,3,5-Tris(4-bromophenyl)benzene (TBB) is supplied by Sigma-Aldrich with a purity of 97% and extensively (>48 h) outgassed in UHV at 140°C. TBB is deposited from Knudsen cells with a crucible temperature in the range from 140 °C to 160 °C. The graphite surface is cleaned prior to experiments by annealing up to 500 °C for 30 minutes. Ag(110) and Cu(111) surfaces are cleaned by repeated cycles of sputtering and annealing. Cleanliness of the substrate is checked prior to evaporation by STM. During deposition, the substrate is held at room temperature. Thermal stability of 2D COFs is verified by annealing of a previously characterized sample and subsequent repeated STM measurements.

II. Additional STM data

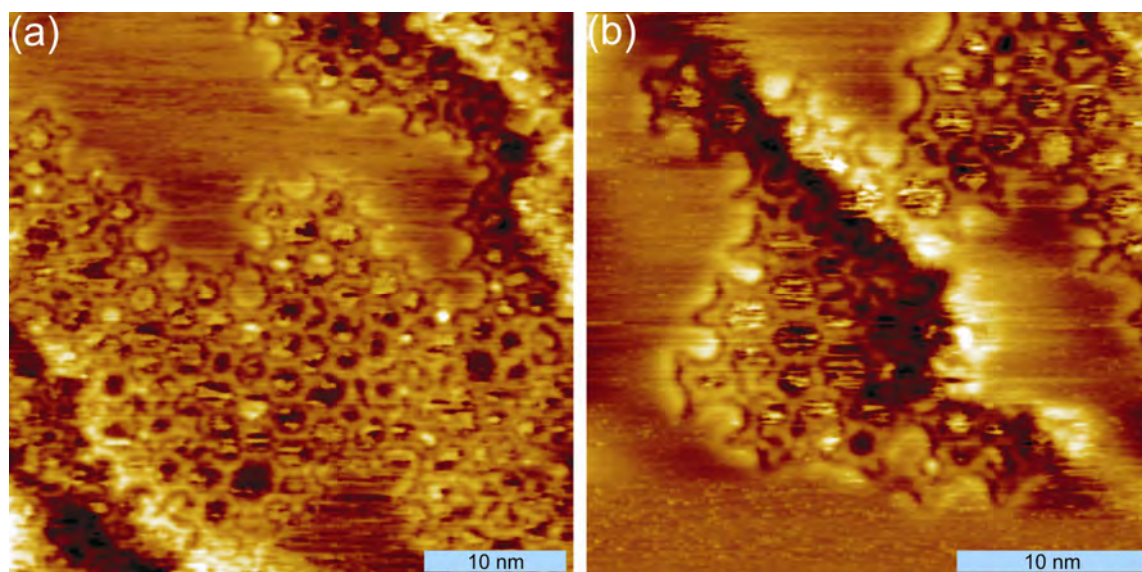


Figure S1. TBB evaporated on Ag(110) at 140 °C for 10 min **(a)** $V = 1.2$ V, $I = 110$ pA **(b)** $V = 1.2$ V, $I = 123$ pA. Both topographs show open-pore structures with high defect density.

The contrast within the cavities can be attributed to coadsorbed molecules or split-off bromine atoms.

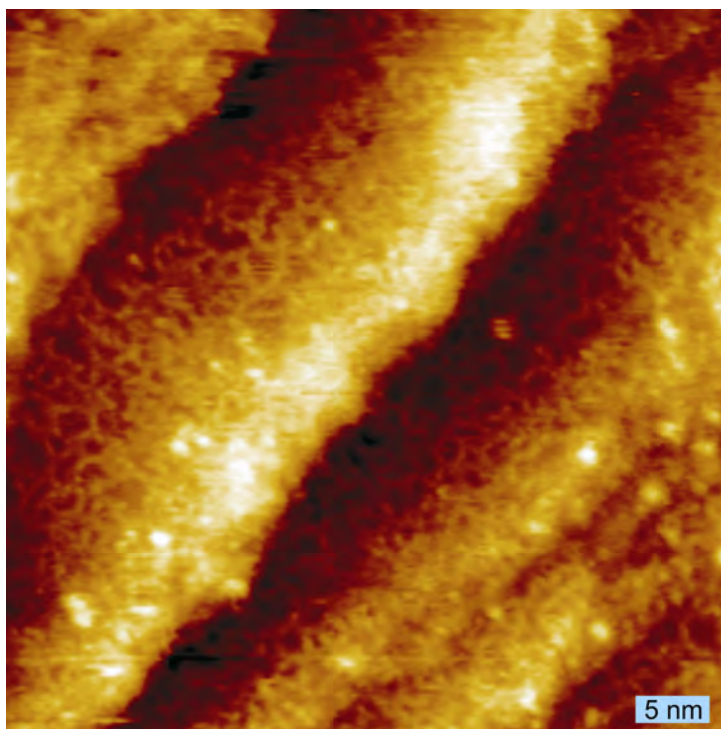


Figure S2. TBB evaporated on Cu(111) and annealed to 400 °C for 20 min ($V = 1.3$ V, $I = 170$ pA). The formerly covalent network is degraded and no ordered structure can be observed.

III. Forcefield and DFT calculations

The geometry of covalent organic frameworks is optimized by means of molecular mechanics simulations, conducted with the Cerius² (Version 4.5, MSI) software package and the Dreiding forcefield.² Periodic boundary conditions are applied to a hexagonal lattice with p6 symmetry and the lattice parameter is varied in order to find the minimum energy configuration. Free standing monolayers, i.e. without substrate influence are simulated. An energy difference of $< 2 \times 10^{-5}$ kcal/mol between single steps serves as a convergence criteria in all calculations.

The minimum energy is found for a lattice parameter of 2.21(2) nm (cf. Fig. S3) in agreement with the experimentally deduced value of 2.2 nm. Fig. S3 depicts the calculated values for the total energy as a function of lattice parameter. This lattice parameter corresponds to a distance of 1.28 nm between adjacent molecules.

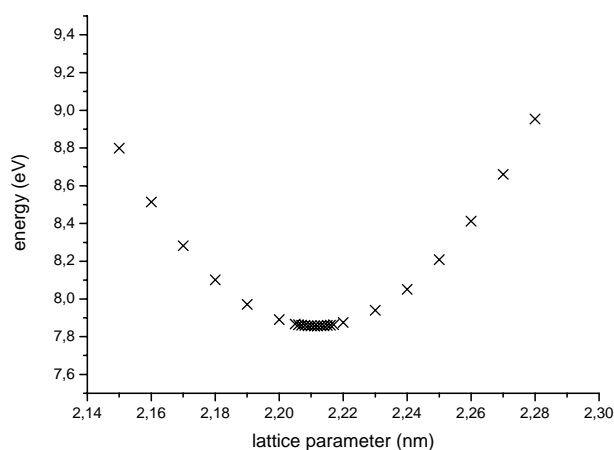


Figure S3. Calculated energy per unit cell for the geometry optimized framework as a function of lattice parameter according to molecular mechanics simulations. The isolated monolayer is fixed to p6 symmetry. A lattice parameter of 2.21(2) nm yields the minimum energy.

The geometry of an ideal hexagonal 2D COF is also optimized by density functional theory (DFT) calculations implemented in the Gaussian03 software package.³ For this purpose, the B3LYP functional with 6-31G(d) basis set is used. Periodic boundary conditions are employed, the substrate is neglected. The input geometry is that of the previously force-field optimized geometry with p6 symmetry. Lattice parameter and angle are allowed to vary. Standardized convergence criteria as preset in Gaussian03 are used. The structure optimization yields lattice parameter of 2.245 nm and 2.243 nm and an angle of 120.02°. Adjacent phenyl rings are tilted by $\sim 60^\circ$ with respect to each other because of steric hindrance. Since the rotational barrier for a biphenyl is relatively low, interaction with the substrate is likely to cause planar adsorption as experimentally observed in the STM topographs.

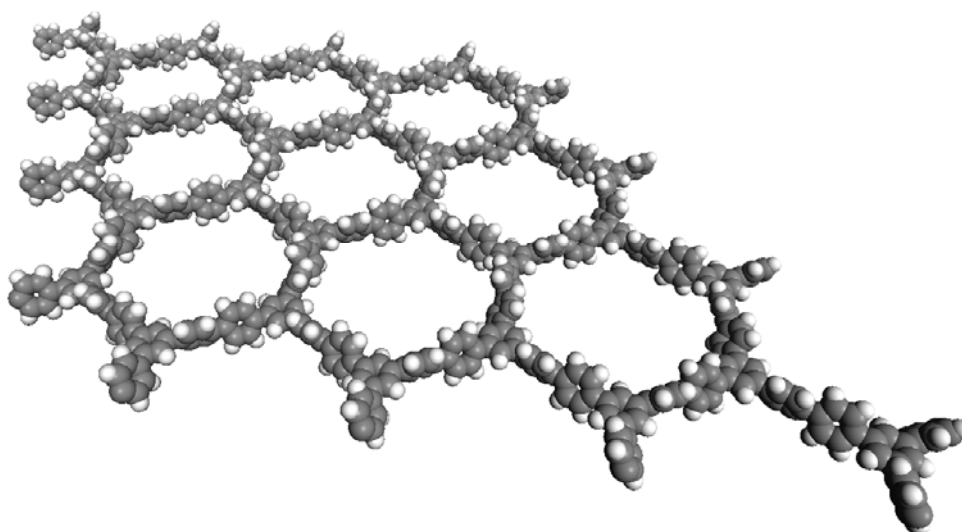


Figure S4. Model of an ideal hexagonal covalent organic framework. The geometry corresponds to the output of the DFT calculation with the above stated lattice parameters.

Phenyl rings are tilted by about 60° with respect to each other.

IV. Thermogravimetric analysis

In an inert atmosphere, approximately 50 mg of TBB are heated with a rate of 1 °C per minute and the weight loss recorded. Degradation sets in at about 250 °C and is largely completed at ~375 °C. A residual of 4% of the original weight of sample remains. The temperature range for deposition by means of vacuum sublimation is 140° - 160°C as indicated by the colored bar in Fig S5 and is significantly lower than the decomposition temperature. Thus, the conclusion that intact molecules arrive at the surface can be drawn.

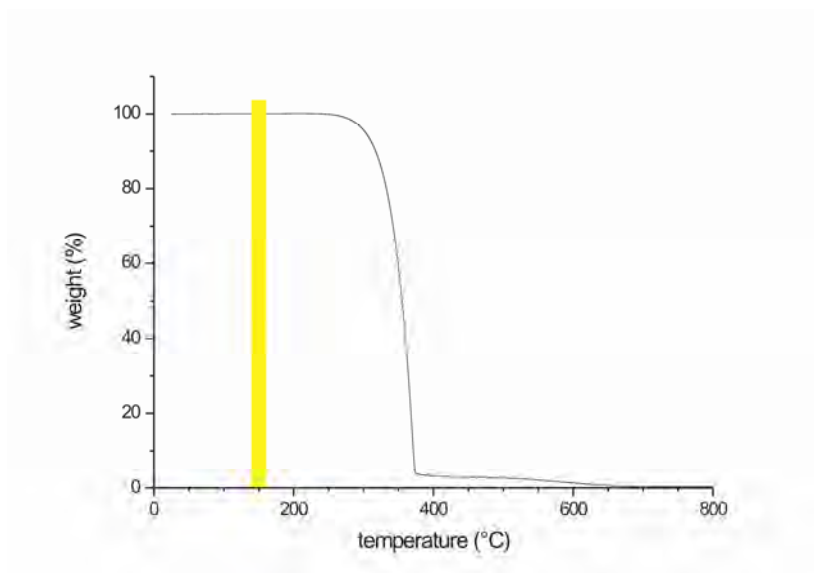


Figure S5. Thermogravimetric analysis of TBB. The colored area indicates the temperature range applied for thermal sublimation.

V. UV/Vis spectra

In order to support the hypothesis that TBB molecules remain intact upon vacuum sublimation, UV/Vis spectroscopy is conducted with n-hexane as solvent. A quartz glass cuvette with an optical path length of 1 mm is used. Unsubstituted 1,3,5-triphenylbenzene (TPB) serves as a control substance. Because of its significantly higher solubility, TPB solutions are diluted by a factor 30, whereas for TBB saturated solutions are used. Three different TBB solutions are prepared and compared: TBB as provided, TBB sublimated once onto the shutter, TBB residuals from the crucible of the Knudsen cell.

In the wavelength range from 200 nm to 500 nm, all absorption spectra exhibit two main peaks (see Fig. S6). For all three TBB solutions these two peaks are centered at the same wavelength, namely $\lambda_1=206$ nm and $\lambda_2=260$ nm. While for unsubstituted TPB the peak at longer wavelength is slightly blue-shifted and centered at $\lambda_2=250$ nm, thereby demonstrating the influence of the Br substitution. Because for all three TBB solutions the shape of the spectra and the peak positions remain the same, we conclude that both thermally sublimed molecules and molecules from the crucible which were held at a temperature of 140 °C - 160 °C for extended amounts of time remain intact.

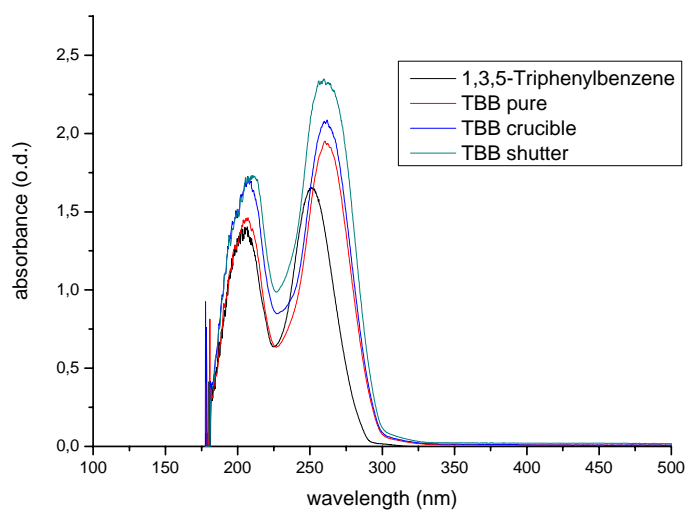
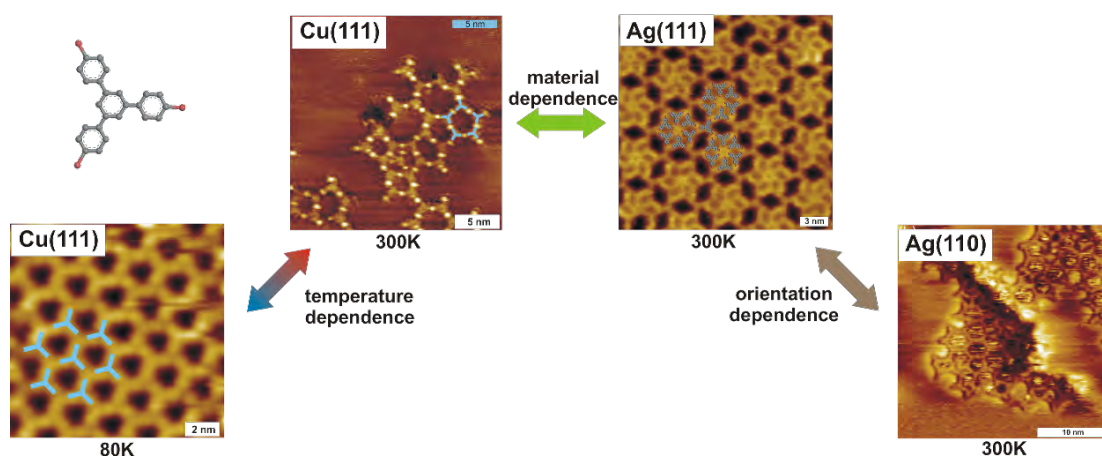


Figure S6. UV/Vis absorption spectra of TBB (saturated solutions) and 1,3,5-Triphenylbenzene (1:30 diluted solutions) in n-hexane

- (1) Stipe, B. C.; Rezaei, M. A.; Ho, W. *Rev. Sci. Instrum.* **1999**, *70*, 137-143.
- (2) Mayo, S. L.; Olafson, B. D.; Goddard, W. A. *J. Phys. Chem.* **1990**, *94*, 8897-8909.
- (3) Frisch, M. J.; Trucks, G. W.; Schlegel, H. B.; Scuseria, G. E.; Robb, M. A.; Cheeseman, J. R.; Montgomery, J., J. A.; Vreven, T.; Kudin, K. N.; Burant, J. C.; Millam, J. M.; Iyengar, S. S.; Tomasi, J.; Barone, V.; Mennucci, B.; Cossi, M.; Scalmani, G.; Rega, N.; Petersson, G. A.; Nakatsuji, H.; Hada, M.; Ehara, M.; Toyota, K.; Fukuda, R.; Hasegawa, J.; Ishida, M.; Nakajima, T.; Honda, Y.; Kitao, O.; Nakai, H.; Klene, M.; Li, X.; Knox, J. E.; Hratchian, H. P.; Cross, J. B.; Bakken, V.; Adamo, C.; Jaramillo, J.; Gomperts, R.; Stratmann, R. E.; Yazyev, O.; Austin, A. J.; Cammi, R.; Pomelli, C.; Ochterski, J. W.; Ayala, P. Y.; Morokuma, K.; Voth, G. A.; Salvador, P.; Dannenberg, J. J.; Zakrzewski, V. G.; Dapprich, S.; Daniels, A. D.; Strain, M. C.; Farkas, O.; Malick, D. K.; Rabuck, A. D.; Raghavachari, K.; Foresman, J. B.; Ortiz, J. V.; Cui, Q.; Baboul, A. G.; Clifford, S.; Cioslowski, J.; Stefanov, B. B.; Liu, G.; Liashenko, A.; Piskorz, P.; Komaromi, I.; Martin, R. L.; Fox, D. J.; Keith, T.; Al-Laham, M. A.; Peng, C. Y.; Nanayakkara, A.; Challacombe, M.; Gill, P. M. W.; Johnson, B.; Chen, W.; Wong, M. W.; Gonzalez, C.; Pople, J. A. *Gaussian, Inc., Wallingford CT 2004*.

6.3 Material and Orientation dependent activity for heterogeneously catalyzed carbon-bromine bond homolysis



J. Phys. Chem. C., **2010**, 114, 12604-12609

Hermann Walch, Rico Gutzler, Thomas Sirtl, Georg Eder, and Markus Lackinger

Material- and Orientation-Dependent Reactivity for Heterogeneously Catalyzed Carbon–Bromine Bond Homolysis

Hermann Walch,^{*,†} Rico Gutzler,[†] Thomas Sirtl,[†] Georg Eder,[†] and Markus Lackinger^{*,†,‡}

Department for Earth and Environmental Sciences and Center for NanoScience (CeNS), Ludwig-Maximilians-University, Theresienstrasse 41, 80333 Munich, Germany, and Deutsches Museum, Museumsinsel 1, 80538 Munich, Germany

Received: March 25, 2010; Revised Manuscript Received: June 18, 2010

Adsorption of the brominated aromatic molecule 1,3,5-tris(4-bromophenyl)benzene on different metallic substrates, namely Cu(111), Ag(111), and Ag(110), has been studied by variable-temperature scanning tunneling microscopy (STM). Depending on substrate temperature, material, and crystallographic orientation, a surface-catalyzed dehalogenation reaction is observed. Deposition onto the catalytically more active substrates Cu(111) and Ag(110) held at room temperature leads to cleavage of carbon–bromine bonds and subsequent formation of protopolymers, i.e., radical metal coordination complexes and networks. However, upon deposition on Ag(111) no such reaction has been observed. Instead, various self-assembled ordered structures emerged, all based on intact molecules. Also sublimation onto either substrate held at ~ 80 K did not result in any dehalogenation, thereby exemplifying the necessity of thermal activation. The observed differences in catalytic activity are explained by a combination of electronic and geometric effects. A mechanism is proposed, where initial charge transfer from substrate to adsorbate, followed by subsequent intramolecular charge transfer, facilitates C–Br bond homolysis.

Introduction

Heterogeneous catalysis provides the basis for the economic synthesis of the majority of compounds produced worldwide and is thus of utmost importance for the chemical industry. In relation to its importance, however, the atomistic understanding of the underlying processes lags behind. The “surface science approach”, which was introduced by Ertl, i.e., the use of atomically flat and clean single crystal surfaces under ultrahigh vacuum (UHV) conditions as model catalysts,^{1,2} has stimulated a lot of effort in this field. Among other techniques, scanning tunneling microscopy (STM) has been taking a major role as a tool to reveal catalytic phenomena by high-resolution real space imaging,^{3–6} in particular for the dissociative adsorption of molecules.^{7,8}

Here we report on the heterogeneously catalyzed dehalogenation of the comparatively large aromatic compound 1,3,5-tris(4-bromophenyl)benzene (TBB, cf. Fig. 1 for structure) on coinage metal surfaces. TBB is also a well-suited candidate monomer for the synthesis of surface supported two-dimensional polymers. For the synthesis of two-dimensional polymers, different strategies are proposed to cleave the C–Br σ -bonds, an activation step which creates free radicals that can subsequently form covalent bonds through addition reactions. Recently, we could show that for the on-surface polymerization the substrate does not merely serve as support, but takes a vital chemical role.⁹ An inert substrate like graphite(001) does not catalyze the surface-mediated homolysis and hence leaves the molecules intact upon physisorption, whereas on Cu(111) and Ag(110) the dehalogenation reaction readily occurs. Yet, instead of directly forming covalent intermolecular bonds, the on-surface

generated radicals coordinate to surface supplied metal atoms in an intermediate reaction step. Thereby coordination complexes introduced as “protopolymers” by Weiss and co-workers are formed¹⁰ through a surface-mediated reaction that has meanwhile also been observed for other systems.^{11–13} The first reaction step is dissociative adsorption of halogenated aromatic species on a copper catalyst, a reaction scheme that resembles the coupling chemistry described by Ullmann in 1901.¹⁴ Cleavage of carbon–halogen bonds followed by the formation of comparatively strong bonds¹⁵ of the resulting radicals to copper atoms is also an intermediate step in the Ullmann coupling reaction. In the original Ullmann reaction the bidentate radical–copper complex is a short-lived reaction intermediate, while for the surface variant the radical–copper complexes are metastable at room temperature. Subsequent thermal annealing releases the coordinating copper atoms and induces covalent C–C coupling of the aromatic species. The initially split-off bromine species binds to the surface and thermally activated diffusion results in island formation at ~ 600 K,¹⁶ whereas desorption takes place at about 950 K.¹⁷ In STM topographs adsorbed bromine atoms appear as depressions on Cu(111), which was explained by quenching of the surface state.¹⁷ In accordance with these findings we also occasionally observe these depressions in the vicinity of protopolymers (see yellow arrow in Figure 1a), which we attribute to split-off bromine atoms, although we cannot unambiguously prove it.

In order to study the role of the metal support in more detail and shed light on the homolysis mechanism, further experiments were conducted on Ag(111), Ag(110), and Cu(111). The substrate temperature during deposition was introduced as an additional parameter. In this study, TBB was deposited on each substrate held at either room temperature or cooled down to ~ 80 K. Subsequently, STM was applied to study the intermolecular bonding schemes and to identify products of a possible dehalogenation reaction.

* To whom correspondence should be addressed. E-mail: hermann.walch@physik.uni-muenchen.de (H.W.), markus@lackinger.org (M.L.).

[†] Ludwig-Maximilians-University.

[‡] Deutsches Museum.

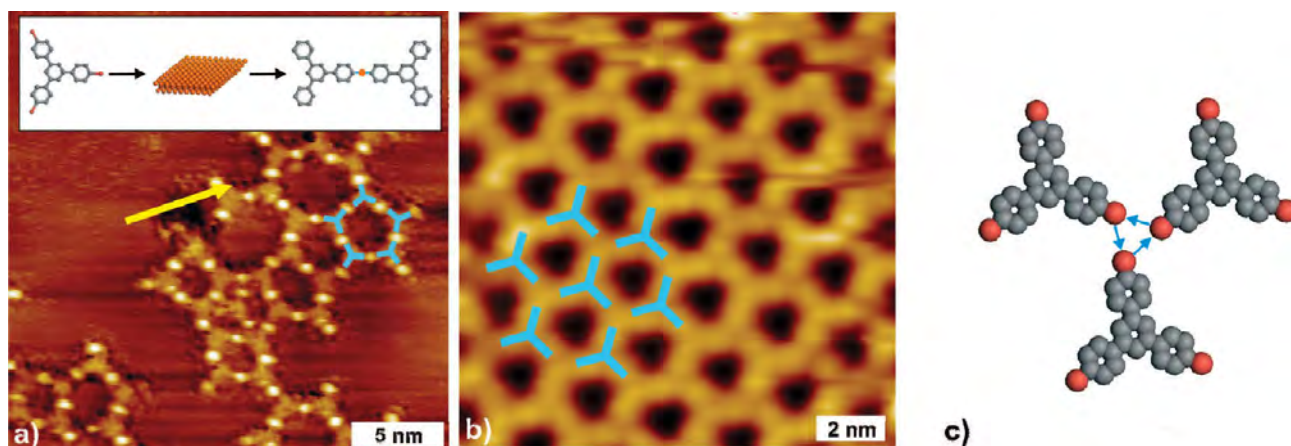


Figure 1. STM topographs of TBB deposited onto Cu(111) with the substrate held at (a) room temperature and (b) ~ 80 K, respectively. (a) Room-temperature deposition readily induces the dehalogenation reaction and subsequent formation of protopolymers ($U_T = 1.50$ V, $I_T = 85$ pA; inset, reaction scheme). (b) Deposition onto Cu(111) at ~ 80 K leads to noncovalent self-assembly of a highly ordered structure ($U_T = -1.98$ V, $I_T = 90$ pA). Due to their size and symmetry, the 3-fold bright features are assigned to single intact TBB molecules as shown in the overlay. (c) Tentative model of the intermolecular arrangement based on STM data. As a consequence of a nonspherical charge distribution around the halogen substituents an electrostatic stabilization known as a halogen–halogen bond becomes feasible.

Results and Discussion

Cu(111). Deposition of TBB onto Cu(111) at room temperature leads to the spontaneous formation of protopolymers, in accordance with previous experiments on brominated aromatic molecules.^{11,12,17} Coordinating copper atoms are either extracted from terraces¹⁸ or supplied by the free adatom gas that originates from a temperature-dependent condensation/evaporation equilibrium at step edges.¹⁹ An STM topograph of TBB–protopolymer networks on Cu(111), i.e., radical–metal coordination complexes, is depicted in Figure 1a. Bright circular protrusions midst the triangular molecular units are clearly discernible, and readily identified as copper atoms. However, an unambiguous experimental indication for protopolymer formation is the center-to-center distance between interlinked molecules. In full agreement with the anticipated value for protopolymers, a distance of ~ 1.50 nm was found. The irregularity and high defect density of these networks is owed to both the pronounced reactivity of phenyl radicals and the low directionality of coordination bonds. By virtue of a postannealing step (up to 300 °C), it was possible to release the copper atoms and eventually convert metal-coordination bonds into covalent C–C interlinks. This is accompanied and proven by a ~ 0.25 nm decrease of the center-to-center distance of adjacent interconnected TBB molecules from ~ 1.50 nm to ~ 1.25 nm.^{9,12}

In order to gain deeper insight into the dissociation mechanism, the present study also takes the influence of the substrate temperature during deposition into account. In the case of Cu(111), a prominent difference arises depending on the substrate temperature: Deposition of TBB onto Cu(111) held at ~ 80 K leads to the formation of highly ordered, virtually defect-free self-assembled structures which are comprised of intact molecules. A representative STM topograph and the corresponding structural model are depicted in Figure 1b,c. Single molecules are clearly resolved and appear as 3-fold symmetric features in accordance with the molecular structure. The structure is based on a hexagonal lattice with $a = 2.05 \pm 0.06$ nm and contains one molecule per unit cell. Both, the high degree of ordering and the unit cell dimensions substantiate the conclusion that molecules remain intact and self-assemble due to relatively weak noncovalent interactions. The halogen substituents cannot be distinguished from the aromatic backbone in the submolecular STM contrast, because the frontier molec-

ular orbitals equally have contributions from the aromatic system and the peripheral halogen substituents, respectively. A comparable cyclic bonding pattern among three halogen atoms has previously been observed in bulk crystals of halogenated phenyls.²⁰ The underlying interaction is of electrostatic origin and attributed to a nonspherical charge distribution around the bromine substituents. Calculations of the electrostatic potential at the halogen atoms propose a positive cap opposite to the C–Br bond and a ring of negative potential around the bond axis.²¹ A cyclic intermolecular arrangement as shown in Figure 1c thus optimizes electrostatic interactions and can be described as Coulombic “donor–acceptor” attraction.²⁰

Warming up the well-ordered TBB layer on Cu(111) to room temperature also induces the formation of protopolymers, similar to those observed for room-temperature deposition. These experimental findings illustrate that dissociation of C–Br bonds on Cu(111) requires thermal activation and that the thermal energy supplied at 300 K is sufficient.

Ag(110). Regarding the dissociation of C–Br bonds upon room temperature deposition, Ag(110) shows a qualitatively similar behavior as Cu(111): formation of protopolymers was readily observed (Figure 2a). For low-temperature deposition, however, TBB molecules do not form ordered structures; instead, adsorption of isolated, apparently immobile single molecules has been observed, as illustrated in Figure 2b. This result is explained by a more corrugated surface potential on Ag(110) as compared to Cu(111). For face-centered cubic (fcc) metals, the potential energy landscape for adsorbates exhibits higher corrugation on (110) than on (111) surfaces. Consequently, thermally activated surface diffusion is more easily suppressed at lower temperatures on (110) surfaces. In addition, surface diffusion is more anisotropic on (110) surfaces than on densely packed (111). In many cases this results in quasi-one-dimensional diffusion, which also hampers self-assembly of two-dimensional islands. Similar to Cu(111), warming up the low-temperature deposited Ag(110) sample to room temperature results in dehalogenation and spontaneous formation of protopolymers.

In summary, only at room temperature are Cu(111) and Ag(110) sufficiently reactive to catalyze homolysis of C–Br bonds in TBB. For low-temperature deposition, differences concerning the mutual arrangement arose: on the densely packed

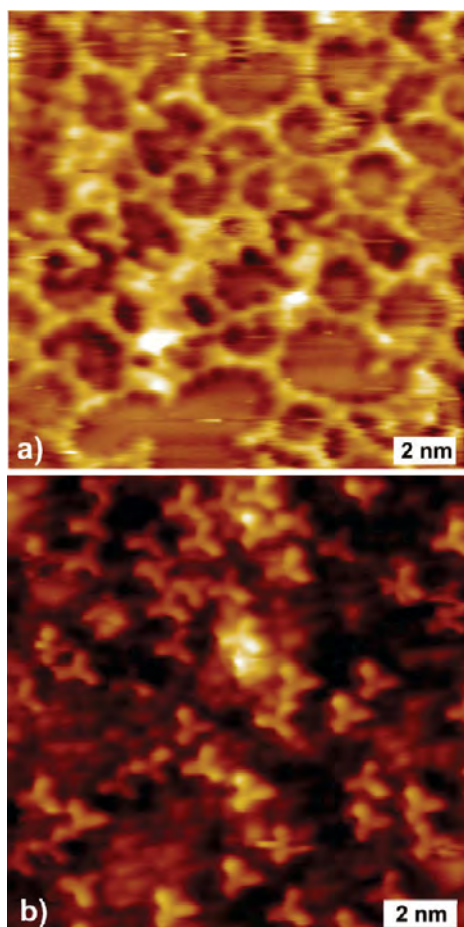


Figure 2. STM topographs of TBB deposited on Ag(110) (a) after warming up the sample to room temperature ($U_T = 1.76$ V, $I_T = 41$ pA) and (b) at ~ 80 K ($U_T = -1.50$ V, $I_T = 110$ pA). Low-temperature deposition results in disordered arrangements of single molecules without any indication of ordered self-assembly due to suppressed lateral mobility on the (110) face; warming up the sample to room temperature leads to dehalogenation and the formation of protopolymers similar to the case for Cu(111). Albeit adatoms are not resolved in this case, the measured center-to-center distances of 1.50 nm between interlinked molecules clearly indicates formation of protopolymers.

Cu(111) surface the lateral mobility of TBB is sufficient to facilitate self-assembly into ordered monolayers, while on Ag(110) the lack of surface mobility leads to adsorption of isolated molecules.

Ag(111). In order to gain deeper insight into the relevant parameters for the catalytic activity of coinage metal surfaces for this particular homolysis reaction, further experiments were conducted on Ag(111). Low-temperature deposition onto Ag(111) results in self-assembly of a monolayer structure similar to the Cu(111) case. The arrangement of molecules, the symmetry of the monolayer, and within the experimental error, the lattice parameter are identical for low-temperature deposition on Cu(111) and Ag(111). Most importantly, similar to the aforementioned cases, for low-temperature deposition TBB molecules also stay intact upon adsorption on Ag(111). Yet, qualitatively different observations in comparison to Cu(111) were made when TBB was evaporated onto Ag(111) at room temperature. Instead of protopolymers—a clear indication of dehalogenation—a variety of distinct self-assembled phases based on intact molecules was observed. All structures are stabilized by weak noncovalent interactions between intact molecules. Representative STM topographs of the various phases on Ag(111) are

presented in Figure 3.²² It is noteworthy that low-temperature deposition followed by warming up the sample resulted in the same morphologies as deposition directly at room temperature. In the overview image of Figure 3a, two coexisting phases, namely, a hexagonal and a row structure with oblique unit-cell, can be distinguished. Furthermore, in the lower part of the image molecules that are “frozen” in a disordered state can be identified. We attribute the emergence of this phase to rapid surface diffusion at room temperature, which kinetically traps molecules in the disorder state.

A detailed analysis of the intermolecular distances in the disordered phase does not indicate any formation of protopolymers or covalently interlinked aggregates. Close ups of the ordered phases are presented in Figure 3b,c. Similar to the low-temperature polymorphs observed on Cu(111) and Ag(111), the well-ordered structures are likewise stabilized by electrostatic interactions between nonspherical charge distributions of halogen substituents. Yet, the structures of these polymorphs are more complex, and in addition to the triple halogen–halogen bonds, the hexagonal structure also contains six-membered rings of cyclic halogen bonds, as shown in Figure 3b. Three of those supramolecular hexamers are interconnected via single TBB molecules in a triple Br–Br–Br bond pattern similar to those observed in the low-temperature structure. As illustrated by the overlaid symbolic representations of the molecules, attractive halogen–halogen interactions are topologically very versatile and not restricted to three or six membered rings. Also a slightly displaced head-to-head geometry enables favorable electrostatic interactions, as exemplified in Figure 3c, and gives rise to another polymorph, the row structure. The measured center-to-center distances of halogen–halogen bond associated dimers (2.05 nm) is significantly larger than for metal-coordinated (1.50 nm) or covalently interlinked dimers (1.25 nm)⁹ and clearly indicates noncovalent interaction. Figure 4 illustrates the three different types of intermolecular bonding schemes and the corresponding center-to-center distances. For the halogen–halogen interaction, the molecules exhibit a slight lateral displacement and significantly larger center-to-center distance as compared to the covalent and metal coordination case. The substantial differences in center-to-center distance allow for a clear distinction of the interaction type solely based on intermolecular distances as measured in STM topographs.

A displaced halogen–halogen bonded dimer is also the basic unit of the structure depicted in Figure 3d, another occasionally observed polymorph that features a rather high packing density. The experimentally observed coexistence of all structures in Figure 3 indicates the relative weakness and topological versatility of halogen–halogen interactions. In any case, it can be stated that for Ag(111) different noncovalent self-assembled structures were observed dependent on the deposition temperature without any indication of dehalogenation either for room temperature or for low temperature deposition.

In brief, the experiments described above reveal a clear dependency of the catalytic activity on the material [Cu(111) vs Ag(111)], but also on the crystallographic surface orientation [Ag(110) vs Ag(111)].

The experimental findings as summarized in Table 1 give rise to the question about the origin and the detailed mechanism of the catalytic activity of the investigated metal surfaces for the dehalogenation reaction. In particular, we want to address the question of which parameters influence the TBB dehalogenation on coinage metal surfaces. Irrespective of substrate material and orientation, for low-temperature deposition we have never observed dehalogenation, a clear indication of a thermally

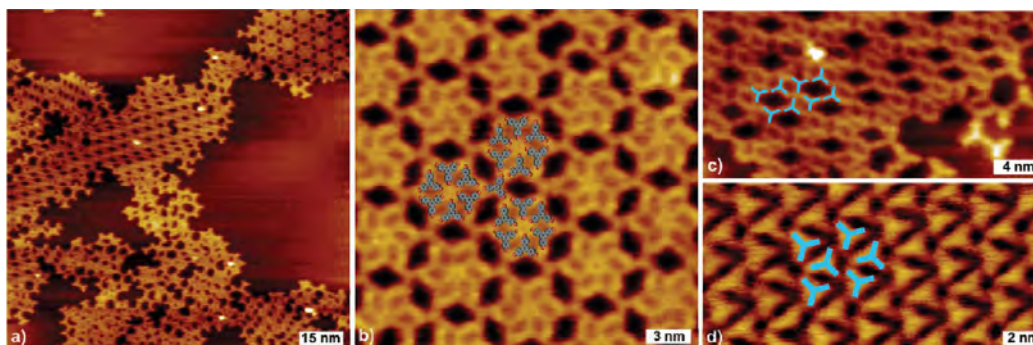


Figure 3. STM topographs of different self-assembled TBB phases on Ag(111). Molecules were deposited at room temperature, while for improved drift stability STM images were acquired at ~ 80 K. (a) Overview image presenting two coexisting ordered phases, namely, a row structure on the upper center part and a hexagonal flower structure in the upper right part. The lower half depicts a disordered phase ($U_T = -1.11$ V, $I_T = 102$ pA). (b) Close up of the flower structure with overlaid molecular model ($U_T = -1.11$ V, $I_T = 90$ pA). (c) Close up of the row structure ($U_T = -1.11$ V, $I_T = 112$ pA). (d) Close up of a third, densely packed structure ($U_T = 1.77$ V, $I_T = 94$ pA).

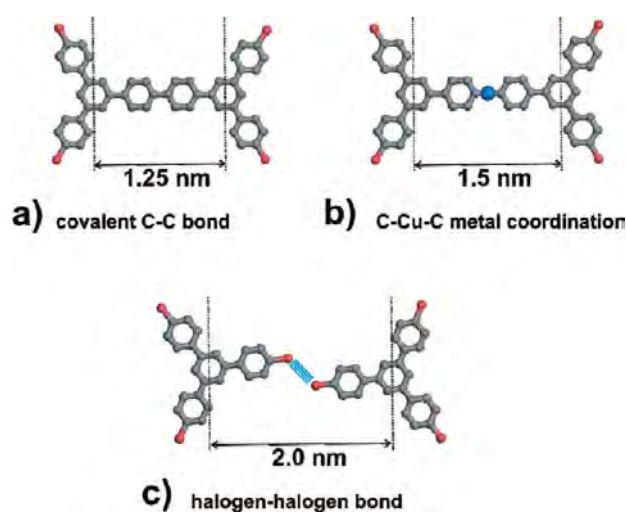


Figure 4. Three possible intermolecular bonding schemes and corresponding center-to-center distances of interlinked molecules. (a) Covalent coupling of TBB molecules leads to the shortest center-to-center distance of ~ 1.25 nm. (b) Metal coordination yields a notably higher center-to-center distance of ~ 1.50 nm. (c) In addition to cyclic triple halogen–halogen–halogen bonds, also a dimeric arrangement with a center-to-center distance of ~ 2.0 nm was observed.

TABLE 1: Summary of Experimentally Observed Intermolecular Bonding Schemes Dependent on Both Substrate Material and Crystallographic Orientation, as Well as Deposition Temperature

	surface @ 80K	surface @ RT
Cu (111)	triple halogen bond	protopolymer
Ag (110)	no ordering	protopolymer
Ag (111)	triple halogen bond	various halogen bond schemes

activated reaction step. TBB molecules do not react and stay intact on the two densely packed Ag(111) and Cu(111) surfaces, where ordered structures were observed. In contrast, on Ag(110) no self-assembly into ordered structures takes place, due to suppressed surface mobility.

In order to understand the substrate dependency of the room-temperature dehalogenation, reactivity is discussed in the framework of heterogeneous catalysis and molecule–metal interactions. Alternatively, an adatom-based surface chemical

approach can also explain the experimental findings. Yet, a significant contribution from step edges as active sites for the dehalogenation can be excluded.

Grounded on DFT results, Christensen and Nørskov state that for an accurate description of surface reactivity one has to differentiate between geometrical and electronic effects.²³ In the following, based on their argumentation, we also want to formally distinguish between electronic and geometric effects, where the former can explain the material and the latter the orientation dependency.

The geometrical effect can be explained by means of the active sites concept, which implies that bond cleavage of adsorbates occurs preferentially at low-coordinated surface atoms,^{24,25} in particular, at vacancies, kinks, step edges, or dislocations.⁸ The literature is rich with examples, where dissociative adsorption favorably occurs at step edges, where reactions rates can be orders of magnitude enhanced as compared to terraces.^{26,27}

However, since on Ag(111) dehalogenation has been observed neither for low-temperature nor for room-temperature deposition, it is concluded that the (mostly densely packed) step edges on this surface are not active sites for cleavage of carbon–halogen bonds. Yet, in general, the reactivity of step edges will depend on their crystallographic direction, which determines both the step edge atom coordination and density of kink or ledge sites, giving rise to substantial differences.

Although overview topographs clearly show that many protopolymers are anchored at step edges, we nevertheless exclude a dominant contribution from step edges for the following reason. If the reaction could exclusively proceed at step edges, only step-edge decoration would be observable but not structures extending into terraces. Protopolymers that are bound to step edges would block these active sites and passivate them, resulting in a quenching of the reaction. Such a self-poisoning effect has, for instance, been observed for the dissociation of ethylene on Ni(111) step edges.²⁸ In conclusion, a dominant contribution from step edges can be ruled out for the dehalogenation reaction.

In the following it is argued that the reactivity differences might originate already in the different atomic arrangement of ideal surfaces and no special active sites are required. While the (111) surfaces of fcc metals are densely packed, the (110) surfaces consist of alternating atomic rows and troughs running along the $[\bar{1}10]$ direction. In some respect the (110) surfaces can be seen as a dense stringing of step edges, thereby exposing a large area density of low coordinated surface atoms that

promote the catalytic activity. For comparison, the coordination number of a topmost surface atom in an ideal fcc (111) surface is 9 while for an ideal fcc (110) surface the coordination number is only 7. The coordination number can directly affect the energy of the d-band center and thus the reactivity of the respective sites.²⁹

A more direct electronic aspect of the catalytic activity comes into play for understanding the observed differences between Cu(111) and Ag(111). Adsorption of aromatic molecules on transition-metal surfaces leads to significant changes in their electronic structure, as concluded for instance from ultraviolet photoelectron spectroscopy (UPS),³⁰ scanning tunneling spectroscopy (STS),³¹ and density functional theory (DFT) studies.^{32–34} Depending on the interaction strength, level shifts, level broadening, or emergence of new electronic states due to hybridization are common and most seriously affect frontier molecular orbitals.³⁵ For instance, Thygesen and Rubio show that the HOMO–LUMO gap of adsorbed molecules shrinks with increasing interaction strength.³⁶ For the aromatic molecule 3,4,9,10-perylenetetracarboxylic acid dianhydride (PTCDA), it has been shown that fully or partly filled LUMO-derived interface states are created upon adsorption on Cu(111) and Ag(111), respectively, rendering the organic layers semiconducting or metallic. On Au(111), on the other hand, only “soft chemisorption” is reported, where energy levels do not shift significantly because of a relatively weak interaction.³⁷ These findings are in accordance with the proposed trend of decreasing reactivity for the d10s1 transition metals when moving down this group in the periodic table of the elements from Cu over Ag to Au.³⁸ This reactivity order was also confirmed by UPS measurements of PTCDA³⁷ and pentacene³⁵ on noble metal surfaces. Both compounds serve as model systems for interaction of large π -conjugated molecules with metal surfaces. Since the underlying processes are fundamental and by no means specific for PTCDA or pentacene, it is proposed that this reactivity order can be generalized for other planar π -conjugated aromatic adsorbates. In both cases the newly formed hybridized orbitals originate from interaction of the π -electrons with the metal s- and d-states, in line with the Newns–Anderson model.^{30,39} Adsorption of aromatic molecules on transition-metal surfaces is also accompanied by charge transfer between adsorbate and substrate as a consequence of the aforementioned adjusting of the frontier molecular orbitals.^{35,37} This can lead to partial filling of mainly the π^* orbital, where the degree of occupancy increases with increasing interaction strength and is thus largest on copper surfaces. Since the π^* orbital is mainly localized at the aromatic system, adsorption induced charge transfer can still not explain the observed homolysis of peripheral C–Br bonds. In order to explain the bond cleavage, we propose that thermally activated charge transfer from the newly occupied π^* into σ^* orbitals, which are antibonding with respect to the C–Br bond, eventually destabilizes these bonds and facilitates homolysis. A similar two-step mechanism for C–X bond dissociation in solution was found by Kimura and Takamuku, who studied halogen scission in aryl halides⁴⁰ and benzyl halides⁴¹ by means of low-temperature pulse radiolysis. First, an additional electron is captured by the π^* orbital and then in a second step transferred into the C–halogen σ^* orbital. This results in destabilization and dissociation of the C–Br bond. Moreover, a comparable two-step mechanism is also discussed for photodissociation of dibromobenzene and tribromobenzene, where the initially excited singlet (π, π^*) state in the phenyl ring decays into the repulsive triplet (n, σ^*) state located at the C–Br bond.⁴² On

the basis of these findings we conclude that the dehalogenation of TBB on densely packed noble metal surfaces can only occur when the interaction strength is sufficiently strong. Evidently, this criterion is fulfilled for Cu(111), but not for Ag(111). For higher corrugated (110) surfaces, however, the reactivity of Ag(110) becomes sufficient to catalyze the dehalogenation reaction. Along the lines of heterogeneous catalysis research, the higher reactivity of Ag(110) as compared to Ag(111) is explained with the higher surface corrugation leading to a lower coordination and thus higher reactivity of surface atoms. Again, Zou and co-workers have confirmed this trend for the adsorption of PTCDA on Ag(111) and Ag(110), where the more corrugated (110) face exhibits stronger interaction.³⁰

As already stated above, a decisive influence of adatom chemistry would also be consistent with our experimental observations and cannot be fully excluded. It is well-known that for metal surface chemistry adatoms can be important mediators or reaction partners for various types of reactions.²⁹ Consequently, both the temperature and surface dependent density of the adatom gas as well as the adatom reactivity can explain reactivity differences. For instance, a face-specific dependency for the adsorption geometry of benzoate molecules has been attributed to the availability of metal adatoms, being significantly higher on Cu(110) as compared to Cu(111).⁴³ It has also been reported that the deprotonation of carboxylic groups in trimesic acid molecules does not take place on pristine Ag(111) at room temperature but can be triggered by an additional supply of more reactive copper atoms.¹⁹ Especially the latter example exemplifies the importance of adatom chemistry for the formation of metal-coordination complexes on surfaces. In this picture, the temperature dependence can be explained by suppression of the adatom gas at lower temperature, while the orientation dependence can be explained by different binding energies of atoms in step edges. However, since we do not observe any formation of protopolymers on Ag(111), a dominant contribution from adatoms for the dehalogenation reaction seems unlikely. Even though the density of adatoms on fcc(111) surfaces is substantially lower than on (110) surfaces, as rationalized by a model based on the change of coordination number for the detachment process,⁴³ at least a few coordination complexes should also be observable on Ag(111), if the reaction was exclusively driven by adatoms. However, a plain consideration of merely the adatom density is not satisfying, and also the adatom reactivity has to be considered. Since the coordination number of adatoms is also surface-dependent, it is conceivable that Ag adatoms behave chemically distinctly on (111) than on (110) surfaces. In order to obtain a detailed and quantitative understanding of the dehalogenation reaction, theoretical studies that address the electronic structure of the chemisorbed molecule–substrate complex and tackle conceivable reactivity differences of adatoms are very desirable.

Conclusions

In summary, studies of a heterogeneously catalyzed dehalogenation reaction, namely full debromination of the aromatic compound TBB, on single crystal metal surfaces revealed interesting reactivity differences. Since the reaction only proceeds on Cu(111), but not on Ag(111), the catalytic capability of the substrate for this reaction is clearly material dependent. On the other hand, the dehalogenation reaction took place on Ag(110), thereby exemplifying that also the specific surface orientation can be decisive. Third, in variable-temperature experiments it was found that the dehalogenation reaction cannot proceed at low substrate temperatures (~ 80 K) irrespective of

the substrate, thereby proving the necessity of thermal activation. In order to explain the occurrence of the reaction as a function of different experimental parameters, we propose a two-step mechanism, where initial charge transfer upon adsorption provides the basis for occupation of an antibonding orbital. Besides the recognized role of active sites, this comparative series of experiments elucidates that the overall reactivity of a catalytically active surface originates from a combination of atomic arrangement and electronic structure.

For future experiments, it would also be enlightening to study the role of the organic compound and its respective electronic structure. For instance, the HOMO–LUMO gap can be altered by means of decreasing or increasing the size of the aromatic system, thereby also affecting the level alignment and magnitude of charge transfer. The strength of the carbon–halogen bond is another accessible parameter worthy of study. This bond can be weakened by substituting bromine with iodine, but it can also be strengthened by substituting bromine with chlorine.

Methods

All samples were prepared and characterized in an ultrahigh vacuum chamber (base pressure $<5 \times 10^{-10}$ mbar) equipped with a scanning tunneling microscope (STM). Metal single crystals [Cu(111), Ag(111), and Ag(110)] were prepared by repeated cycles of Ne⁺ ion sputtering and annealing. 1,3,5-Tris(4-bromophenyl)benzene was obtained from a commercial source (Sigma Aldrich) and vacuum sublimed from a home-built Knudsen cell with crucible temperatures between 150 and 160 °C.⁴⁴ Samples were deposited in the microscope, which is a home-built beetle-type STM mounted on a flow cryostat and thus able to operate at variable temperatures. During deposition the STM and the substrates were held either at room temperature or at ~80 K. Typically, images were acquired at ~80 K (also for room temperature deposition), because of improved drift stability of the instrument at low temperatures.

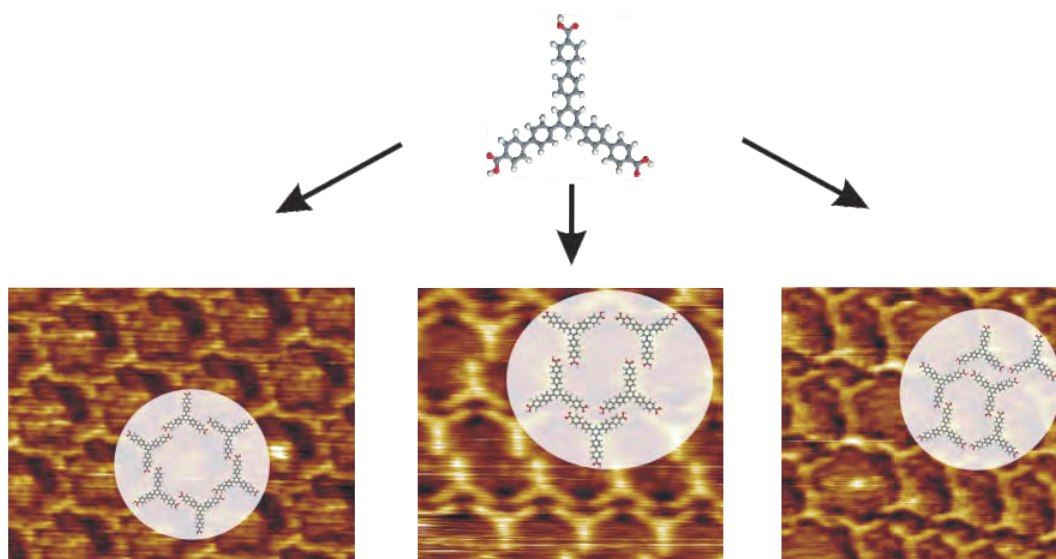
Acknowledgment. Financial support by the Deutsche Forschungsgemeinschaft (SFB 486) and the Nanosystems Initiative Munich (NIM) is gratefully acknowledged. G.E. acknowledges support by the Hanns-Seidel-Stiftung.

References and Notes

- Ertl, G.; Freund, H. J. *Phys. Today* **1999**, *52*, 32–38.
- Ertl, G. *J. Vac. Sci. Technol., A* **1983**, *1*, 1247–1253.
- Bowker, M. *Surf. Sci.* **2009**, *603*, 2359–2362.
- Bowker, M. *Chem. Soc. Rev.* **2007**, *36*, 1656–1673.
- Vang, R. T.; Lauritsen, J. V.; Laegsgaard, E.; Besenbacher, F. *Chem. Soc. Rev.* **2008**, *37*, 2191–2203.
- Leibslle, F. M.; Murray, P. W.; Francis, S. M.; Thornton, G.; Bowker, M. *Nature* **1993**, *363*, 706–709.
- Africh, C.; Comelli, G. *J. Phys.: Condens. Matter* **2006**, *18*, R387–R416.
- Zambelli, T.; Winterlin, J.; Trost, J.; Ertl, G. *Science* **1996**, *273*, 1688–1690.
- Gutzler, R.; Walch, H.; Eder, G.; Kloft, S.; Heckl, W. M.; Lackinger, M. *Chem. Commun.* **2009**, 4456–4458.
- Sykes, E. C. H.; Han, P.; Kandel, S. A.; Kelly, K. F.; McCarty, G. S.; Weiss, P. S. *Acc. Chem. Res.* **2003**, *36*, 945–953.
- McCarty, G. S.; Weiss, P. S. *J. Am. Chem. Soc.* **2004**, *126*, 16772–16776.
- Lipton-Duffin, J. A.; Ivasenko, O.; Perepichka, D. F.; Rosei, F. *Small* **2009**, *5*, 592–597.
- Xi, M.; Bent, B. E. *J. Am. Chem. Soc.* **1993**, *115*, 7426–7433.
- Ullmann, F.; Bielecki, J. *Ber. Dtsch. Chem. Ges.* **1901**, *34*, 2174–2185.
- Migani, A.; Illas, F. *J. Phys. Chem. B* **2006**, *110*, 11894–906.
- Nanayakkara, S. U.; Sykes, E. C. H.; Fernandez-Torres, L. C.; Blake, M. M.; Weiss, P. S. *Phys. Rev. Lett.* **2007**, *98*, 206108.
- Blake, M. M.; Nanayakkara, S. U.; Claridge, S. A.; Fernandez-Torres, L. C.; Sykes, E. C. H.; Weiss, P. S. *J. Phys. Chem. A* **2009**, *113*, 13167–13172.
- Pai, W. W.; Bartelt, N. C.; Peng, M. R.; Reuttobroy, J. E. *Surf. Sci.* **1995**, *330*, L679–L685.
- Lin, N.; Payer, D.; Dmitriev, A.; Strunskus, T.; Woll, C.; Barth, J. V.; Kern, K. *Angew. Chem., Int. Ed.* **2005**, *44*, 1488–1491.
- Bosch, E.; Barnes, C. L. *Cryst. Growth Des.* **2002**, *2*, 299–302.
- Awwadi, F. F.; Willett, R. D.; Haddad, S. F.; Twamley, B. *Cryst. Growth Des.* **2006**, *6*, 1833–1838.
- In order to improve the drift stability of the microscope, measurements were performed at ~80 K, also for samples where molecules were deposited at room temperature.
- Christensen, C. H.; Norskov, J. K. *J. Chem. Phys.* **2008**, *128*, 182503.
- Taylor, H. S. *Proc. R. Soc. London, Ser. A* **1925**, *108*, 105–111.
- Norskov, J. K.; Bligaard, T.; Hvolbaek, B.; Abild-Pedersen, F.; Chorkendorff, I.; Christensen, C. H. *Chem. Soc. Rev.* **2008**, *37*, 2163–2171.
- Gambardella, P.; Sljivancanin, Z.; Hammer, B.; Blanc, M.; Kuhnke, K.; Kern, K. *Phys. Rev. Lett.* **2001**, *87*, 056103.
- Liu, Z. P.; Hu, P. *J. Am. Chem. Soc.* **2003**, *125*, 1958–1967.
- Vang, R. T.; Honkala, K.; Dahl, S.; Vestergaard, E. K.; Schnadt, J.; Laegsgaard, E.; Clausen, B. S.; Norskov, J. K.; Besenbacher, F. *Nat. Mater.* **2005**, *4*, 160–162.
- Hammer, B. *Top. Catal.* **2006**, *37*, 3–16.
- Zou, Y.; Kilian, L.; Scholl, A.; Schmidt, T.; Fink, R.; Umbach, E. *Surf. Sci.* **2006**, *600*, 1240–1251.
- Kilian, L.; Hauschild, A.; Temirov, R.; Soubatch, S.; Scholl, A.; Bendounan, A.; Reinert, F.; Lee, T. L.; Tautz, F. S.; Sokolowski, M.; Umbach, E. *Phys. Rev. Lett.* **2008**, *100*, 136103.
- Bilic, A.; Reimers, J. R.; Hush, N. S.; Hoft, R. C.; Ford, M. J. *J. Chem. Theory Comput.* **2006**, *2*, 1093–1105.
- Toyoda, K.; Nakano, Y.; Hamada, I.; Lee, K.; Yanagisawa, S.; Morikawa, Y. *J. Electron Spectrosc. Relat. Phenom.* **2009**, *174*, 78–84.
- Romaner, L.; Nabok, D.; Puschnig, P.; Zojer, E.; Ambrosch-Draxl, C. *New J. Phys.* **2009**, *11*, 053010.
- Yamane, H.; Kanai, K.; Ouchi, Y.; Ueno, N.; Seki, K. *J. Electron Spectrosc. Relat. Phenom.* **2009**, *174*, 28–34.
- Thygesen, K. S.; Rubio, A. *Phys. Rev. Lett.* **2009**, *102*, 046802.
- Duhm, S.; Gerlach, A.; Salzmann, I.; Broker, B.; Johnson, R. L.; Schreiber, F.; Koch, N. *Org. Electron.* **2008**, *9*, 111–118.
- Hammer, B.; Norskov, J. K. *Nature* **1995**, *376*, 238–240.
- Tautz, F. S. *Prog. Surf. Sci.* **2007**, *82*, 479–520.
- Kimura, N.; Takamuku, S. *J. Am. Chem. Soc.* **1995**, *117*, 8023–8024.
- Kimura, N.; Takamuku, S. *Bull. Chem. Soc. Jpn.* **1993**, *66*, 3613–3617.
- Kadi, M.; Davidsson, J. *Chem. Phys. Lett.* **2003**, *378*, 172–177.
- Perry, C. C.; Haq, S.; Frederick, B. G.; Richardson, N. V. *Surf. Sci.* **1998**, *409*, 512–520.
- Gutzler, R.; Heckl, W. M.; Lackinger, M. *Rev. Sci. Instrum.* **2010**, *81*, 015108.

JP102704Q

6.4 On the Scalability of Supramolecular Networks - High Packing Density vs Optimized Hydrogen Bonds in Tricarboxylic Acid Monolayers



Langmuir, **2010**, 26(13), 10708-10716

Jürgen F. Dienstmaier, Kingsuk Mahata, Hermann Walch, Wolfgang M. Heckl,
Michael Schmittl, and Markus Lackinger

On the Scalability of Supramolecular Networks – High Packing Density vs Optimized Hydrogen Bonds in Tricarboxylic Acid Monolayers

Jürgen F. Dienstmaier,^{*,†} Kingsuk Mahata,[‡] Hermann Walch,[†] Wolfgang M. Heckl,^{§,⊥}
Michael Schmittel,[‡] and Markus Lackinger^{*,†}

[†]Department for Earth- and Environmental Sciences and Center for NanoScience (CeNS), Ludwig-Maximilians-University, Theresienstrasse 41, D-80333 Munich, Germany, [‡]Center of Micro and Nanochemistry and Engineering, Organische Chemie I, Universität Siegen, Adolf-Reichwein-Strasse 2, D-57068 Siegen, Germany, [§]Deutsches Museum, Museumsinsel 1, D-80538 Munich, Germany, and [⊥]Department of Physics, TUM School of Education, Technical University Munich, Schellingstrasse 33, D-80333 Munich, Germany

Received October 21, 2009

We present a scanning tunneling microscopy (STM) based study of 1,3,5-tris[4'-carboxy(1,1'-biphenyl-4-yl)]benzene (TCBPB) monolayers at the liquid–solid interface. In analogy to smaller aromatic 3-fold symmetric tricarboxylic acids, this compound was aimed to yield two-dimensional nanoporous networks with large cavities. Depending on the solute concentration, three crystallographically distinct phases with pores of different size and shape were observed on graphite (001) with heptanoic acid as solvent. All three phases have the same dimer motif as basic building block in common. Yet, as opposed to other carboxylic acid assemblies, these dimers are not interconnected by 2-fold O–H···O hydrogen bonds as anticipated, but by two energetically inferior C–H···O hydrogen bonds. Instead of the common head-to-head arrangement, this bonding pattern results in displaced dimers, which allow for higher packing density, and due to their lower symmetry give rise to chiral polymorphs. In accordance with studies of comparable systems, a positive correlation between solute concentration and average surface packing density is identified and rationalized by thermodynamic arguments.

1. Introduction

Scalability of structures is an interesting and intriguing aspect of material science, and isoreticular metal organic frameworks (IRMOFs) represent a particularly nice and well-known example thereof.¹ A widely open and definitely system-specific question is to what extent building blocks can be scaled up, while the underlying structure is still retained. In the case of porous systems, up-scaling of building blocks may lead to increased pore size which opposes nature's affinity for dense packing. The strength of directional interactions as hydrogen or coordination bonds remains nearly independent of molecular size, whereas the omnipresent van der Waals interactions gain in magnitude with increasing sizes of molecules. As a consequence, up-scaling definitely alters the balance of interactions. For that very reason, the existence of an upper limit for the pore size is predicted for surface supported 2D nanoporous supramolecular systems.² The present study aims to expand the pore size as compared to those of previously studied hexagonal open pore networks formed by 3-fold symmetric aromatic tricarboxylic acids. The smallest representative is trimesic acid (TMA, Figure 1a) which consists of a central phenyl ring, symmetrically substituted with three carboxylic groups. Already for this comparatively small building block, different polymorphic structures were revealed at the liquid-

graphite interface depending on the solvent applied.^{3,4} Moreover, a whole series of systematically varying TMA monolayer structures with increasing packing density was reported on Au(111).⁵ These observations already indicate that self-assembly is not exclusively dictated by the building block, but depends to a large extent on the type of surface, conditions, and environment.^{3,6–8} This apparent drawback, however, can be turned into the advantage of having a handle on self-assembly, provided that underlying processes are understood on a molecular level. The next larger tricarboxylic acid investigated is 1,3,5-benzenetri-carboxylic acid (BTB, Figure 1b), where three phenyl rings have been added as conformationally rigid spacers between the central phenyl ring and each peripheral carboxylic group. Similar to TMA, BTB also exhibits polymorphism both at the liquid–solid interface⁷ and under vacuum conditions.⁹ Moreover, for BTB, reversible temperature dependent phase transitions have been observed at the liquid–solid interface, and are explained by a thermodynamic model.¹⁰ With phenylethyne units as even larger spacers (Figure 1c), either complete methylation of the inner phenyl ring or use of aprotic aromatic solvents were required to obtain planar adsorption of molecules followed by self-assembly into hexagonal networks.¹¹ Herein, we would like to present our

*Corresponding authors. E-mail: (M.L.) markus@lackinger.org.

(1) Doonan, C. J.; Morris, W.; Furukawa, H.; Yaghi, O. M. *J. Am. Chem. Soc.* **2009**, *131*, 9492.

(2) Weber, U. K.; Burlakov, V. M.; Perdigão, L. M. A.; Fawcett, R. H. J.; Beton, P. H.; Champness, N. R.; Jefferson, J. H.; Briggs, G. A. D.; Pettifor, D. G. *Phys. Rev. Lett.* **2008**, *2008*, 156101.

(3) Lackinger, M.; Griessl, S.; Heckl, W. M.; Hietschold, M.; Flynn, G. W. *Langmuir* **2005**, *21*, 4984.

(4) MacLeod, J. M.; Ivasenko, O.; Perepichka, D. F.; Rosei, F. *Nanotechnology* **2007**, *18*, 424031.

(5) Ye, Y.; Sun, W.; Wang, Y.; Shao, X.; Xu, X.; Cheng, F.; Li, J.; Wu, K. *J. Phys. Chem. C* **2007**, *111*, 10138.

(6) Yang, Y.; Wang, C. *Curr. Opin. Colloid. Interface Sci.* **2008**, *14*, 135.

(7) Kampschulte, L.; Lackinger, M.; Maier, A.; Kishore, R. S. K.; Griessl, S.; Schmittel, M.; Heckl, W. M. *J. Phys. Chem. B* **2006**, *110*, 10829.

(8) Leigh, D. F.; Nörenberg, C.; Cattaneo, D.; Owen, J. H. G.; Porfyrakis, K.; Li Bassi, A.; Ardavan, A.; Briggs, G. A. D. *Surf. Sci.* **2007**, *601*, 2750.

(9) Ruben, M.; Payer, D.; Landa, A.; Comisso, A.; Gattinoni, C.; Lin, N.; Collin, J.; Sauvage, J.; De Vita, A.; Kern, K. *J. Am. Chem. Soc.* **2006**, *128*, 15644.

(10) Gutzler, R.; Sirtl, T.; Dienstmaier, J. F.; Mahata, K.; Heckl, W. M.; Schmittel, M.; Lackinger, M. *J. Am. Chem. Soc.* **2010**, *132*, 5084.

(11) Gutzler, R.; Lappe, S.; Mahata, K.; Schmittel, M.; Heckl, W. M.; Lackinger, M. *Chem. Commun.* **2009**, *2009*, 680.

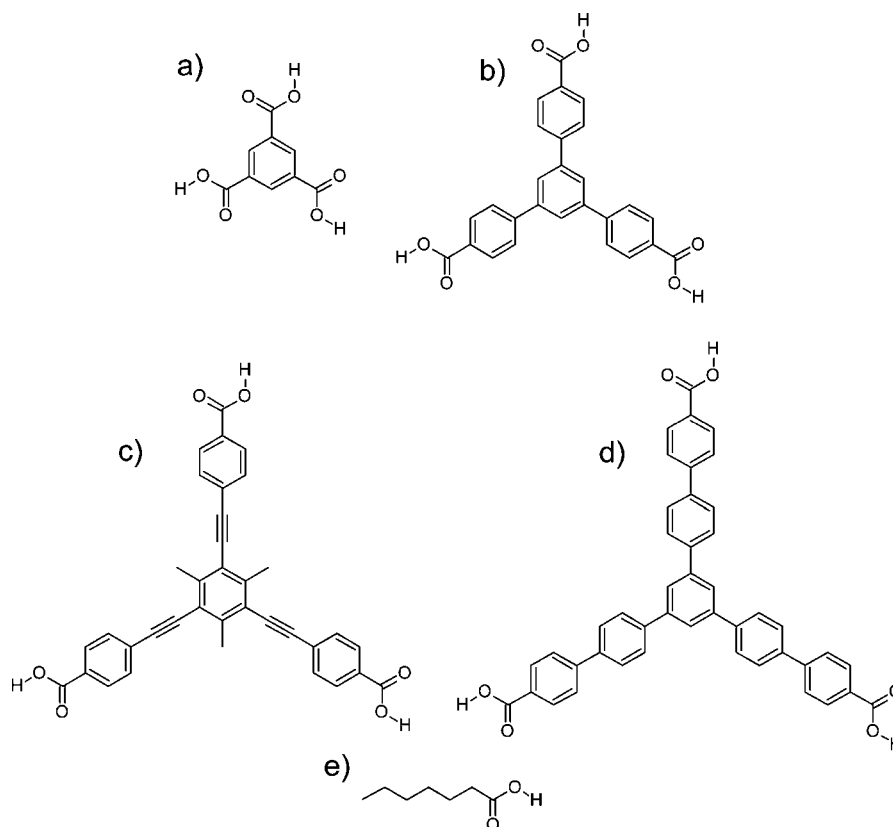


Figure 1. Chemical structures of tricarboxylic acids investigated in the present and previous studies: (a) trimesic acid (TMA), (b) 1,3,5-benzenetribenzoic acid (BTB), (c) 4-{2-[(3,5-bis[2-(4-carboxyphenyl)-1-ethynyl]-2,4,6-trimethyl-phenyl)-1-ethynyl]}-1,1'-biphenyl-4-yl]benzoic acid (TCBPB), and (d) 1,3,5-tris[4'-carboxy(1,1'-biphenyl-4-yl)]benzoic acid (TCBPB), and (e) heptanoic acid, utilized as solvent.

results on the next larger homologue, the 1,3,5-tris[4'-carboxy(1,1'-biphenyl-4-yl)]benzoic acid (TCBPB, Figure 1d), which contains a biphenyl spacer. The results reveal that the enlarged tricarboxylic acid does not yield the anticipated well-known isotopological hexagonal networks, but other monolayer structures with nonideal intermolecular hydrogen bond patterns.

2. Experimental Section

TCBPB (1,3,5-tris[4'-carboxy(1,1'-biphenyl-4-yl)]benzoic acid) was synthesized in two steps via trimerization of 1-(4'-bromobiphenyl-4-yl)ethanone followed by carboxylation using *n*-BuLi/CO₂ (cf. Supporting Information).¹² Prior to dissolving TCBPB, the hygroscopic compound was desiccated at 150 °C for 48 h in high vacuum in order to completely remove residual water. Heptanoic acid (Fluka, purity ≥99%, Figure 1e), nonanoic acid (Aldrich, purity 96%), 1-nonanol (Merck, purity ≥98%), 1-undecanol (Sigma-Aldrich, purity ≥99%), dodecane (Fluka, purity ≥99%) were used as solvents without further purification. Saturated solutions served as stock solutions for successive dilutions. Those were prepared by dissolving the solute until sedimentation, sonication for 15 min, and subsequent centrifugation for 15 min at 5000 rpm. The solubility of TCBPB in heptanoic acid was determined by UV–vis absorption spectroscopy conducted with a USB4000 UV–vis spectrometer from Ocean Optics and amounts to $49.3 \pm 5.3 \mu\text{M}$.

Molecular monolayers were imaged *in situ* at the liquid–solid interface under ambient conditions with a home-built STM operated by an ASC 500 Scanning Probe Microscopy Controller from attocube systems AG. For all experiments, STM tips were mechanically cut from a Pt/Ir (90/10) wire and used without

further insulation. Constant current topographs were obtained with tunneling voltages around +0.8 V applied to the tip and set point currents in the order of 50 pA for fatty acid solvents, and 200–800 pA for alcohols. Prior to the STM experiments, small droplets (~5 μL) of the respective solution were applied to the freshly cleaved basal plane (5 × 5 mm²) of highly oriented pyrolytic graphite (HOPG).

3. Results and Discussion

TCBPB is comprised of seven phenyl rings and functionalized with three carboxylic acid groups in a 3-fold symmetric manner. Its structure is depicted in Figure 1d and can be regarded as a central phenyl ring which is symmetrically substituted with three 4-biphenylcarboxylic acid entities.

Polymorphic Structures. In a series of STM experiments with varying TCBPB concentration in heptanoic acid, three crystallographically different monolayer polymorphs could be distinguished. Representative high resolution STM topographs of all three polymorphic modifications (oblique-I, oblique-II, and displaced chickenwire) are depicted in Figure 2. Unit cell parameters, as accurately determined by the so-called “split-image” technique, as well as number and type of intermolecular hydrogen bonds are summarized in Table 1. Tentative models of all polymorphic structures based on STM data are depicted in Figure 3. During the experimental time span neither phase transitions nor ripening were observed. As further discussed below, a clear correlation between surface structure and solute concentration is evident, albeit for diluted solutions (<10%) only coexistence of several structures was found.

(12) Sun, D.; Xe, Y.; Mattox, T. M.; Parkin, S.; Zhou, H. *Inorg. Chem.* **2006**, *45*, 7566.

(13) Lackinger, M.; Heckl, W. M. *Langmuir* **2009**, *25*, 11307–11321.

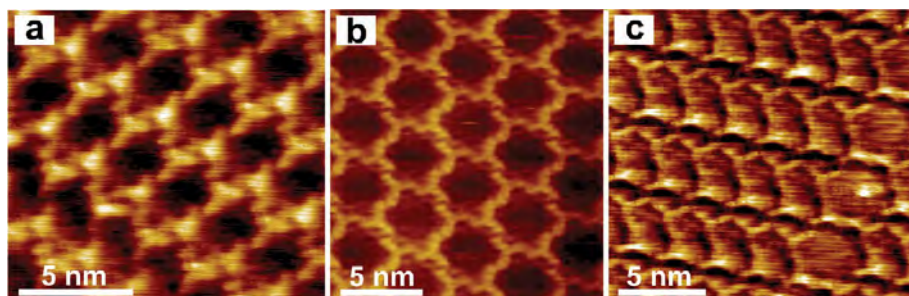


Figure 2. High resolution STM topographs of all three TCBPB monolayer polymorphs distinguished in this study: (a) oblique-I; (b) displaced chickenwire (drift corrected); (c) oblique-II intergrown with a single row of displaced chickenwire.

Table 1. Summarized Unit Cell Parameters and Overview over Number and Type of Intermolecular Hydrogen Bonds (per Unit Cell) for Each Polymorphic Structure^a

structure	<i>a</i> (nm)	<i>b</i> (nm)	γ (deg)	area (nm ²)	packing density (nm ⁻²)	C–H···O hydrogen bonds	O–H···O hydrogen bonds
oblique-I	3.6	2.5	81.8	9.0	0.22	6	2
oblique-II	3.8	2.4	78.3	9.0	0.22	4	2
displaced chickenwire	4.2	3.8	59.2	13.7	0.15	6	0

^aAll three structures incorporate two molecules per unit cell.

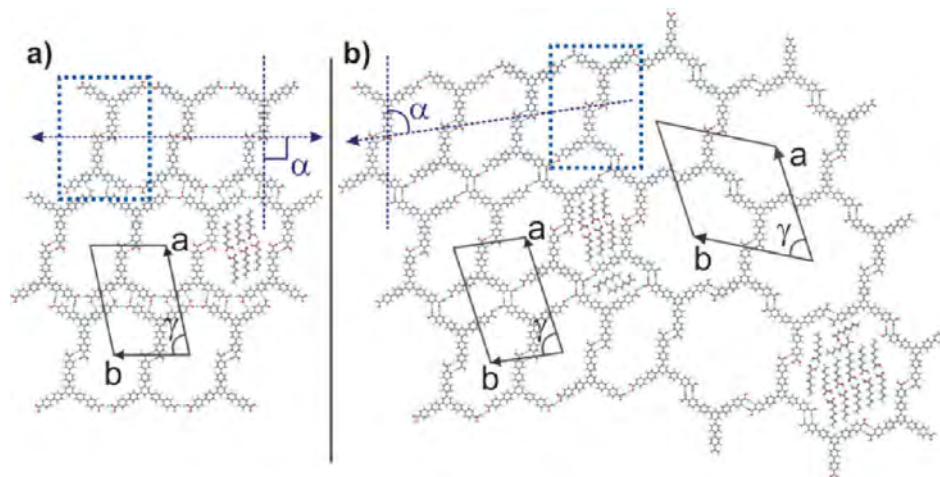


Figure 3. Proposed models of the three polymorphs (all models are to scale) with unit cells indicated. In addition, possible configurations for solvent coadsorption (based on dimerization) within the cavity voids are depicted. The dotted rectangle highlights the displaced TCBPB dimer motif, the basic unit of all three structures. Dashed purple lines with arrows indicate the row direction and the definition of the dimer axis, respectively (a) oblique-I structure ($\alpha \approx 90^\circ$); (b) oblique-II (left-hand side, $\alpha \approx 81^\circ$) and displaced chickenwire (right-hand side). This model illustrates the perfect structural match between oblique-II and displaced chickenwire, and the possibility of the two structures to deliberately intergrow.

In order to check for the generality of the observed concentration-induced polymorphism, a series of different solvents was tested: In dodecane no self-assembled TCBPB monolayers were observed at all, in full agreement with its solubility being even below the detection limit of the UV–vis spectrometer. On the other hand, STM experiments with nonanoic acid and 1-nonanol as solvents exclusively yielded the oblique-I polymorph, and no concentration-induced polymorphism was observed for dilutions down to 10% and 5% saturation, respectively. Below these concentrations self-assembly of TCBPB was not observed anymore. Interestingly, for concentrations down to 35% saturation 1-undecanol as solvent resulted either in isolated small patches of the oblique-I polymorph or disordered but stable molecular aggregates (cf. Supporting Information Figure S4). For lower concentrations adsorbed molecules could not be observed anymore. Concentration dependent emergence of three distinct monolayer structures was *exclusively* observed with heptanoic acid as solvent.

As anticipated, the large aromatic system of TCBPB results in planar adsorption on graphite. Single molecules can be identified by means of their 3-fold symmetry and the size match between STM image and molecular geometry. Planar adsorption is common to all three polymorphic structures with a dimer, as highlighted in Figure 3, being the basic motif of all structures. Yet, in contrast to the commonly encountered head-to-head dimer motifs of carboxylic acids, the observed TCBPB dimer is bound in a displaced geometry. These untypical dimers are associated via two C–H···O hydrogen bonds, rather than by two equivalent O–H···O hydrogen bonds as for the commonly encountered configuration. According to the model which was derived from the STM topographs, the carbon–oxygen distance in the dimer amounts to ~ 0.25 nm, and hence lies well within the range of C–H···O hydrogen bonds.^{14,15}

(14) Scheiner, S.; Kar, T.; Gu, Y. *J. Biol. Chem.* **2001**, *276*, 9832.

(15) Desiraju, G. R. *Acc. Chem. Res.* **1996**, *59*, 441.

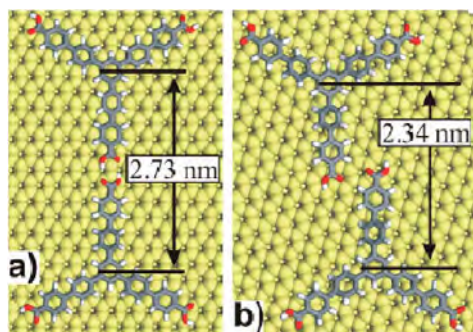


Figure 4. Molecular mechanics simulations of both isolated ideal and displaced dimers with their corresponding dimensions. Ideal dimers form two cyclic O–H···O hydrogen bonds, while displaced dimers are associated via two C–H···O hydrogen bonds.

The association motif described above is not so common for carboxylic acids, albeit bulk crystal structures of carboxylic acids do not always necessarily feature the cyclic 2-fold O–H···O hydrogen bond between COOH groups. For instance in acetic acid crystals, the COOH hydroxyl groups form O–H···O hydrogen bonds, whereas the corresponding carbonyl oxygen atoms take part in C–H···O hydrogen bonds.^{16–19} Another example is given by crystalline pyrazinic acid, where the carbonyl oxygen atoms preferentially take part in heteronuclear C–H···O hydrogen bonds.²⁰ Although, the formation probability of 2-fold cyclic O–H···O hydrogen bonds is very high for carboxylic acids, different bonding patterns may still arise.¹⁵ It is also known that C(sp²)-H groups can act as weak hydrogen bond donors, because their acidity is sufficiently enhanced,²¹ and in particular cyclic synthons emerge for this moiety.²² Moreover, the acidity of H atoms in the *ortho* position of benzoic acid is enhanced.²³

As compared to the more common head-to-head dimer, the displaced dimer exhibits nonideal hydrogen bonds, but on the other hand allows for a higher packing density of molecules on the surface. Also, the displaced dimer gives rise to chiral monolayers, an important difference in comparison to the head-to-head dimer. Accordingly, both enantiomeric forms have been observed for all three polymorphs. Interestingly, a very similar tricarboxylic acid of comparable size resulted in monolayers with head-to-head dimers at the octanoic acid–graphite interface.^{24,25}

Molecular mechanics simulations of both, ideal and displaced dimers along with the corresponding dimensions are depicted in Figure 4. According to *ab initio* calculations the binding enthalpy for the cyclic 2-fold O–H···O hydrogen bond between two carboxylic groups amounts to -60 kJ mol^{-1} (slightly dependent on functional and basis set^{26–28}) whereas a single C–H···O hydrogen bond contributes only -4 to -8 kJ mol^{-1} .^{23,29} Because

(16) Jones, R. E.; Templeton, D. H. *Acta Crystallogr.* **1958**, *11*, 484.

(17) Nahringerbauer, I. *Acta Chem. Scand.* **1970**, *24*, 453.

(18) Jönsson, P. G. *Acta Crystallogr.* **1971**, *B27*, 893.

(19) Turi, L.; Dannenberg, J. J. *J. Phys. Chem.* **1993**, *97*, 12197.

(20) Takusagawa, F.; Higuchi, T.; Shimada, A.; Tamura, C.; Sasada, Y. *Bull. Chem. Soc. Jpn.* **1974**, *47*, 1409.

(21) Steiner, T.; Desiraju, G. R. *Chem. Commun.* **1998**, *1998*, 891.

(22) Nangia, A. *Cryst. Eng.* **2001**, *4*, 49.

(23) Vishweshwar, P.; Nangia, A.; Lynch, V. M. *J. Org. Phys.* **2002**, *67*, 556.

(24) Ma, Z.; Wang, Y.; Wang, P.; Huang, W.; Li, Y.; Lei, S.; Yang, Y.; Fan, X.; Wang, C. *ACS Nano* **2007**, *1*, 160.

(25) Li, Y.; Ma, Z.; Qi, G.; Yang, Y.; Zeng, Q.; Fan, X.; Wang, C.; Huang, W. *J. Phys. Chem. C* **2008**, *112*, 8649.

(26) Zhao, J.; Khalizov, A.; Zhang, R.; McGraw, R. *J. Phys. Chem. A* **2009**, *113*, 680.

(27) Neuheuser, T.; Hess, B. A.; Reutel, C.; Weber, E. *J. Phys. Chem.* **1994**, *98*, 6459.

(28) Winkler, A.; Mehl, J. B.; Hess, P. *J. Chem. Phys.* **1994**, *100*, 2717.

(29) Desiraju, G. R. *Acc. Chem. Res.* **1991**, *24*, 290.

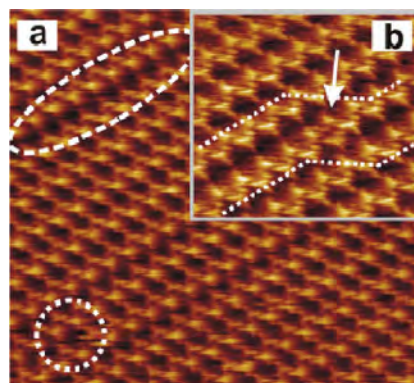


Figure 5. STM topographs of oblique-I obtained at 10% saturation illustrating commonly observed defects. (a) This topograph ($46 \times 41 \text{ nm}^2$) demonstrates how the chirality of the displaced dimer can switch within one row (dotted circle) without major disturbance of the surrounding network. The dashed oval highlights a row of molecules self-assembled in a head-to-head configuration, instead of the commonly found displaced geometry. (b) Close-up ($21 \times 18 \text{ nm}^2$) of the head-to-head row of dimers showing how this defect propagates from one row to the adjacent row, by means of two molecules (highlighted by the arrow) which acquire intermediate positions.

the strength of a 2-fold cyclic O–H···O hydrogen bond is considerably enhanced by cooperative effects, a phenomenon known in the literature as resonance-assisted hydrogen bonding (RAHB),³⁰ the binding energy of the 2-fold cyclic hydrogen bond is significantly larger than twice the binding energy of a single O–H···O hydrogen bond. RAHB is well established for cyclic O–H···O hydrogen bonds between two carboxylic groups, but this cooperative effect is in principle also conceivable for the two cyclic C–H···O hydrogen bonds of the displaced dimer (cf. Supporting Information, Figure S5 for a detailed bonding scheme).^{31,32} Nevertheless, it can be stated that the association strength of ideal straight dimers is considerably higher than for the displaced geometry.

The three observed polymorphs differ in the mutual arrangement of the dimers, their unit cell parameters, packing densities, and hydrogen bond patterns. In the following discussion, the numbers of hydrogen bonds refer to the primitive unit cells.

In the oblique-I structure, dimers are aligned along rows with their axis (as defined in Figure 3a) almost perpendicular to the row. Unit cell parameters of the oblique-I structure amount to $3.6 \pm 0.2 \times 2.5 \pm 0.2 \text{ nm}^2$ with an angle of $81.8^\circ \pm 4^\circ$. According to the tentative model each dimer is associated with its intrarow neighbor through two single O–H···O hydrogen bonds. The binding strength of such a single, nonlinear hydrogen bond is estimated to be in the order of -8.4 kJ mol^{-1} .^{33,34} Adjacent rows of dimers are interconnected by networks of four comparatively weak C–H···O hydrogen bonds, with each bond adding ~ -4 to -8 kJ mol^{-1} to the binding enthalpy.^{23,29}

Two different types of defects as illustrated in Figure 5 are commonly observed in the oblique-I structure. The white dotted circle highlights an area where within a row the dimer chirality

(30) Gilli, G.; Gilli, P. *J. Mol. Struct.* **2000**, *552*, 1.

(31) Steiner, T. *Chem. Commun.* **1997**, *1997*, 727.

(32) Castellano, R. K. *Curr. Org. Chem.* **2004**, *8*, 845.

(33) The binding enthalpy of a single straight O–H···O hydrogen bond amounts to -11 kJ mol^{-1} ; common force fields approximate the angular dependence of the binding energy with a cosine function; in this case the angle is $\sim 40^\circ$, consequently the binding energy of this nonlinear hydrogen bond is reduced to -8.4 kJ mol^{-1} .

(34) Beck, J. F.; Mo, Y. *J. Comput. Chem.* **2006**, *28*, 455.

changes. Another interesting defect is the occurrence of an intermingled row of head-to-head dimers. The origin of this defect is not entirely clear: it may be a consequence of an antiphase domain boundary or may also result from the continuation of a point defect. Both types of defects can easily be incorporated into the structure without major disturbances or stress imposed on the surrounding network. Figure 5b shows how the head-to-head arrangement propagates from one row to the adjacent row. In order to facilitate this transition, the two molecules marked by the arrow, occupy intermediate positions.

The second polymorph distinguished in this study is the displaced chickenwire structure as depicted in Figure 2b. This structure can either occur as a single row, as observed in Figure 2c, or self-assemble into larger domains. The displaced chickenwire structure is hexagonal within the experimental error and belongs to the two-dimensional space group $P6$ which does not exhibit any mirror or glide planes. The unit cell parameters amount to $4.2 \pm 0.2 \times 3.8 \pm 0.2 \text{ nm}^2$ with an angle of $59^\circ \pm 2^\circ$ and a tentative model is depicted in Figure 3b. Each TCBPB molecule is interconnected to three adjacent molecules through in total six $\text{C-H}\cdots\text{O}$ hydrogen bonds in a 3-fold symmetric manner. The number of $\text{C-H}\cdots\text{O}$ hydrogen bonds per unit cell also amounts to six. The displaced chickenwire structure encompasses approximately circular cavities with an inner diameter of 3.5 nm. The space group $P6$ is chiral, and correspondingly, both enantiomeric forms of the displaced chickenwire structure have been observed on the surface. It is highly likely that growth of a nucleus into a chirally pure domain is promoted, since only attachment of homochiral dimers allows for translational symmetry.^{35,36}

The third structure observed for TCBPB is oblique-II with unit cell parameters $3.8 \pm 0.2 \times 2.4 \pm 0.2 \text{ nm}^2$ and an angle of $78^\circ \pm 4.5^\circ$. Figure 2c exemplifies the close relation between oblique-II and displaced chickenwire. In fact, oblique-II cannot exist independently from the displaced chickenwire structure (vide infra). Oblique-I and -II are very similar to each other, with both structures consisting of linearly aligned dimers. Equally, their packing densities are nearly identical. Besides all similarities, there are important differences: In oblique-II, the angle between the dimer axis (cf. Figure 3 for a definition) and row axis amounts to $\sim 81^\circ$, while in oblique-I it is perpendicular. Second, while the TCBPB dimers in oblique-I form hydrogen bonds with six adjacent dimers, in oblique-II, dimers form hydrogen bonds with only four adjacent dimers. In oblique-II, dimers are interconnected by two $\text{O-H}\cdots\text{O}$ hydrogen bonds within the rows, whereas in between the rows interaction is mediated by two $\text{C-H}\cdots\text{O}$ hydrogen bonds. These differences in hydrogen bonding also result in important morphological differences: While oblique-I exhibits one larger cavity per unit cell, oblique-II contains both a larger and a smaller cavity per unit cell which can be understood as the opening of voids in between the rows, as evident from Figure 3. Yet, since the packing densities of both structures are so similar, the summed cavity area of oblique-II has to be similar to the cavity area of oblique-I. Finally, in contrast to oblique-I, we have never observed defects in oblique-II, where adjacent dimers within the same row exhibit different chirality. The reason is most likely that in oblique-II such a defect would seriously disturb or even interrupt the network. Because in oblique-II the dimer axis is no longer perpendicular to the row direction, the rows cannot be continued anymore if one of the dimers exhibits opposite chirality. The same holds true for the

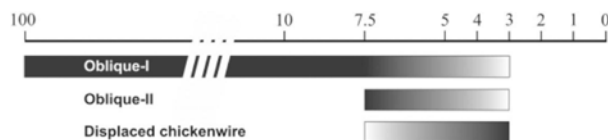


Figure 6. Dependence between solute concentration and emergence of the various interfacial monolayer phases of TCBPB in heptanoic acid (dark colors imply a large weight of the respective phase). The percentage refers to saturated solutions, where the solubility in heptanoic acid amounts to $49.3 \pm 5.3 \mu\text{M}$. Only for concentrations between 10% and 100% oblique-I was observed as single phase, otherwise phase mixtures were observed, where the relative weight depends on concentration. For concentrations below 3% saturation interfacial monolayers could not be observed anymore. Tested concentrations are 100% (saturation), 50, 20, 10, 7.5, 5, 4, 3, 2, and 1%.

displaced chickenwire, where only homochiral domains have been observed. Moreover, also at the interface of intergrown chickenwire and oblique-II the chirality is preserved. In contrast to oblique-I and displaced chickenwire, no unattached domains of oblique-II were found in numerous independent experimental runs. Each oblique-II domain was always associated with at least one row of the displaced chickenwire structure. As evident from the model in Figure 3(b) there is an ideal structural match between oblique-II and displaced chickenwire. The two structures can intergrow without strain, provided that the chirality is maintained across the interface. The fact that pure extended domains of displaced chickenwire have regularly been observed without any indications of oblique-II suggests that the latter phase cannot exist independently of the displaced chickenwire acting as a nucleus. In the light of the similarity in packing densities of oblique-I and -II and the perfect match between oblique-II and chickenwire, oblique-II may be considered as an intermediate phase.

Concentration Dependence. The occurrence of the three distinct phases can be controlled by solute concentration in solution. The concentration dependence is graphically summarized in Figure 6: from 100% down to 10% saturation, oblique-I self-assembles exclusively. At a concentration of 7.5%, both oblique-II and displaced chickenwire start to appear on the surface, yet in coexistence with oblique-I. With increasing dilution, i.e. in the range between 7.5% and 3% saturation, the equilibrium shifts toward the displaced chickenwire structure, while the percentage of the two oblique phases diminishes. At a concentration of 5%, oblique-II dominates over the two other polymorphs, while at 3% displaced chickenwire is observed almost exclusively. At concentrations below $\sim 3\%$ saturation, no self-assembled monolayers could be detected anymore. It is noteworthy that at these low concentrations, the number of dissolved molecules in the liquid phase becomes already comparable to the number of molecules in the monolayer (cf. Supporting Information Figure S6 for details). Albeit below 10% saturation none of the phases has been observed exclusively, a clear correlation between solute concentration and dominance of one of the monolayer phases has been found: the higher the solute concentration in solution, the higher the packing density of molecules on the surface. A more gradual increase of average surface packing density becomes possible through the coexistence of various phases. For instance, as illustrated in Figure 7, parts a and b, for concentrations of 5% and 3%, respectively the coexistence of chickenwire and oblique-II was found. Yet, for the higher solute concentration of 5% the dominant phase is densely packed oblique-II, whereas for the lower concentration of 3% the less dense displaced chickenwire structure dominates. It can clearly be seen that the intergrown arrangement of displaced chickenwire

(35) Miura, A.; Jonkheijm, P.; De Feyter, S.; Schenning, A. P. H. J.; Meijer, E. W.; De Schryver, F. C. *Small* **2005**, *1*, 131.

(36) De Feyter, S.; De Schryver, F. C. *J. Phys. Chem. B* **2005**, *109*, 4290.

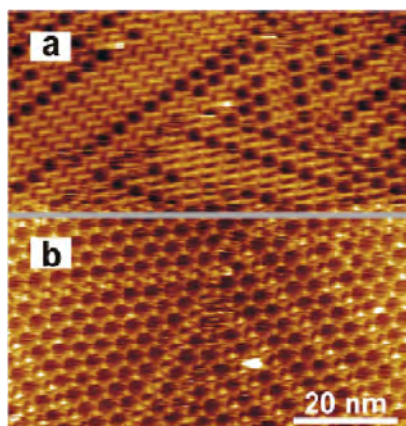


Figure 7. STM topographs acquired at (a) 5%, and (b) 3% TCBPB concentration. By means of controlling the solute concentration the relative amount of adsorbed monolayer phases can be influenced. The more diluted solution yielded a higher amount of the less densely packed chickenwire structure, whereas for the higher concentration oblique-II dominates. The scale bar applies to both images. Parts a and b exhibit opposite chirality.

and oblique-II retains the same chirality. Apparently, by varying the surface content of the two phases the system can continuously adjust any average surface concentration of molecules between the packing densities of both structures.

Solvent Coadsorption. Since nanoporous networks expose pristine substrate to solution, coadsorption of either solute or solvent molecules within the cavities is to be expected and was concluded also for other nanoporous systems.^{10,11,25} Especially in the displaced chickenwire structure six free hydroxyl groups of bordering molecules point into each cavity, resulting in “sticky cavities”. Hence the host–guest interaction is enhanced, which could promote coadsorption of guests with hydrogen bond acceptors. This coadsorption is manifested in the reproducible observation of contrast features within the cavities, as also observed for other nanoporous systems at the liquid–solid interface.⁷ A representative example of internal contrast in the cavities of the chickenwire structure is depicted in Figure 2c. Contrast features are not unique for the chickenwire structure, but were also observed within the cavities of both oblique structures, as shown in Figure 8 for oblique-I. Because in the oblique structures the internal contrast features have a striped appearance which is consistent with the lamella characteristics observed for alkane derivatives³⁷ or carbamates with long aliphatic chains,^{38,39} they could be readily associated with assemblies of heptanoic acid solvent molecules²⁵ rather than with TCBPB molecules. Although, a single stabilizing O–H···O hydrogen bond between a coadsorbed solvent molecule and the free hydroxyl groups in the cavity wall is conceivable, it is more favorable for heptanoic acid solvent molecules to adsorb dimerized in the cavities of the three structures as shown in the tentative models in Figure 3. The proposed adsorption geometry is also in agreement with the contrast features depicted in Figure 8. Interaction between the free hydroxyl groups of the TCBPB network with heptanoic acid molecules in a more upright geometry is still possible. Yet, such an arrangement is difficult to verify by STM imaging.

(37) Giancarlo, L. C.; Fang, H.; Rubin, S. M.; Bront, A. A.; Flynn, G. W. *J. Phys. Chem. B* **1998**, *102*, 10255.

(38) Kim, K.; Plass, K. E.; Matzger, A. J. *Langmuir* **2003**, *19*, 7149.

(39) Kim, K.; Plass, K. E.; Matzger, A. J. *Langmuir* **2005**, *21*, 647.

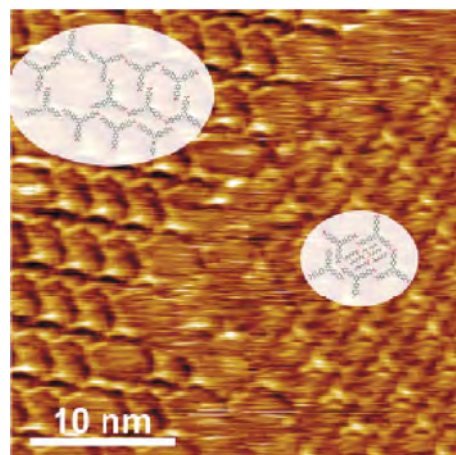


Figure 8. A representative example of internal contrast features found within the cavities of oblique-I with a tentative model of coadsorbed heptanoic acid molecules. This image was obtained at 4% concentration. Notice that the three structures can coexist at this concentration.

Thermodynamics. In view of the self-assembled structures of smaller analogous tricarboxylic acids an important question arises: Why has the common ideal chickenwire structure based on head-to-head dimers never been observed for TCBPB molecules, but only the displaced chickenwire structure? Since many studies on 2D interfacial self-assembly conclude that the monolayers are in thermodynamical equilibrium with the supernatant solution,^{40–43} in the following it is argued that thermodynamics favors the displaced rather than the ideal chickenwire structure for this large aromatic tricarboxylic acid. In general, the driving force for self-assembly is the associated minimization of Gibbs free energy which in this case is composed of an enthalpic gain and an entropic loss. The enthalpic gain arises from attractive adsorbate–substrate and adsorbate–adsorbate interactions, while entropy is generally diminished when molecules associate or adsorb on a surface.

Estimates of the enthalpic gain per molecule ΔH were obtained from a combination of molecular mechanics (MM) simulations based on the Dreiding force field with literature values for intermolecular interaction energies. The molecule–substrate interaction was estimated by MM, while for intermolecular hydrogen bonds literature values were considered. According to MM results, the enthalpy of adsorption of a single TCBPB molecule on graphite amounts to -392 kJ mol^{-1} . In the displaced chickenwire structure each molecule is interconnected with three adjacent molecules by in total six hydrogen bonds, where each bond adds about -6 kJ mol^{-1} when a possible RAHB stabilization is not taken into account.^{23,29} Consequently the total average molar binding enthalpy in the displaced chickenwire structure amounts to $\Delta H = -392 \text{ kJ mol}^{-1} + 0.5 \times 6 \times -6 \text{ kJ mol}^{-1} = -410 \text{ kJ mol}^{-1}$, where the factor 0.5 corrects for double counting of pairwise intermolecular interactions. The same procedure provides ΔH for oblique-I ($-418.4 \text{ kJ mol}^{-1}$), oblique-II (-415 kJ mol^{-1}), and ideal chickenwire (-482 kJ mol^{-1}). For the latter

(40) Kampschulte, L.; Werblösch, T. L.; Kishore, R. S. K.; Schmittl, M.; Heckl, W. M.; Lackinger, M. *J. Am. Chem. Soc.* **2008**, *130*, 8502.

(41) Lei, S.; Tahara, K.; De Shryver, F. C.; Van der Auweraer, M.; Tobe, Y.; De Feyter, S. *Angew. Chem., Int. Ed.* **2008**, *47*, 2964.

(42) Stabel, A.; Heinz, R.; Schryver, F. C.; Rabe, J. P. *J. Phys. Chem.* **1995**, *99*, 205.

(43) Eichhorst-Gerner, K.; Stabel, A.; Moessner, G.; Declercq, D.; Valiyaveetil, S.; Enkelmann, V.; Müllen, K.; Rabe, J. P. *Angew. Chem., Int. Ed. Engl.* **1996**, *13-14*, 1492.

Table 2. Comparison of Molecular Packing Densities, Entropic Costs Δs , Enthalpic Gains Δh , and Free Energies Δg per Unit Area of the Three Experimentally Observed and One Hypothetical TCBPB Polymorphs for Two Different Concentrations (Saturated Solution vs Diluted Solution at 4% Saturation)^a

structure	packing density (10 ¹⁴ cm ⁻²)	$-T\Delta s$ ($\mu\text{J cm}^{-2}$) saturated ^b	$-T\Delta s$ ($\mu\text{J cm}^{-2}$) 4% saturated ^b	Δh ($\mu\text{J cm}^{-2}$)	$\Delta g = \Delta h - T\Delta s$ ($\mu\text{J cm}^{-2}$) saturated	$\Delta g = \Delta h - T\Delta s$ ($\mu\text{J cm}^{-2}$) 4% saturation
displaced chickenwire	0.15	+2.88 (+2.91)	+3.08 (+3.13)	-10.21	-7.33 (-7.30)	-7.13 (-7.08)
ideal chickenwire	0.10	+1.92 (+1.97)	+2.05 (+2.11)	-8.00	-6.08 (-6.03)	-5.95 (-5.89)
oblique-I	0.22	+4.22 (+4.22)	+4.52 (+4.59)	-15.28	-11.06 (-11.06)	-10.77 (-10.69)
oblique-II	0.22	+4.22 (+4.22)	+4.52 (+4.59)	-15.16	-10.94 (-10.94)	-10.64 (-10.57)

^aThe entropic contribution to the free energy $-T\Delta s$ was evaluated at room temperature (300 K) and considers translational and rotational entropy. The total binding enthalpy Δh contains contributions from molecule–molecule and molecule–substrate interactions. For molecule–molecule interactions only hydrogen bonds were considered and van der Waals contributions neglected. Area normalized values were derived by multiplying molar quantities with molecular packing densities as obtained from STM (displaced chickenwire, oblique-I and -II) or MM data (ideal chickenwire).

^bFor values in parentheses the concentration change upon self-assembly has been included (cf. Supporting Information), whereas for the other values the loss of translational entropy has been estimated based on eq 1.

structure the *ab initio* value of -60 kJ mol^{-1} was employed for the binding enthalpy of straight 2-fold O–H \cdots O hydrogen bonds.^{27,28} The packing density of this hypothetical polymorph was estimated by MM simulations of a single six membered ring which result in a hexagonal lattice with $a = 4.7 \text{ nm}$, and consequently a packing density of 0.10 nm^{-2} .

In the following a molecule based approach proposed by Whitesides et al. is used to estimate the entropic loss of self-assembly.⁴⁴ Upon adsorption from solution, molecules completely lose their rotational and translational entropy. For conformationally rigid molecules like TCBPB, the loss of conformational entropy can be neglected. Likewise, vibrational entropy does not change significantly during self-assembly and can also be ignored. Translational and rotational entropy of soluted molecules can be estimated by the following equations:⁴⁴

$$S_{\text{trans}} = R \ln \left[\frac{1}{c} \left(\frac{2\pi m k_B T e^{5/3}}{h^2} \right)^{3/2} \right] \quad (1)$$

$$S_{\text{rot}} = R \ln \left[\frac{\pi^{1/2}}{\gamma} \left(\frac{8\pi^2 k_B T e}{h^2} \right)^{3/2} (I_1 I_2 I_3)^{1/2} \right] \quad (2)$$

Here, R is the gas constant, T the temperature, k_B is Boltzmann's, and h Planck's constant while e is Euler's number, m denotes the solute's mass, and c is its concentration. In order to avoid overestimation of translation entropy, the concentration refers to the free volume of the solvent (32 mL for 1 L of heptanoic acid) as obtained by the hard cube approximation.⁴⁴ Furthermore, γ is related to the symmetry of the solute molecule, while I_1 , I_2 , and I_3 are its principle moments of inertia. According to the equations above, the loss of rotational entropy per adsorbed molecule is independent of concentration, whereas the loss of translational entropy per molecule as derived from the Sackur–Tetrode equation depends inversely logarithmic on concentration. Consequently, the total entropy change per adsorbed molecules, as given by the sum of rotational and translational entropy, depends on concentration and increases with dilution.

Because of the relatively low solubility of TCBPB in heptanoic acid, the amount of dissolved molecules in $5 \mu\text{L}$ becomes comparable to the amount of molecules in $5 \times 5 \text{ mm}^2$ of a monolayer, especially for diluted solutions. Thus, the concentration can already decrease significantly upon self-assembly of a monolayer, and eq 1 underestimates the loss of translational

entropy per molecule. A more accurate expression for loss of translational entropy which also includes changes of the concentration upon self-assembly is provided in the Supporting Information (eqs S1 and S2). However, as evident from Table 2, concentration changes during self-assembly result only in minor corrections.

Since the surface coverage in these experiments is always close to unity, we refer to the free energy per unit area $\Delta g = \Delta G/A$. Combining the total entropic cost $\Delta S = \Delta S_{\text{trans}} + \Delta S_{\text{rot}}$ with STM derived molecular packing densities allows to estimate entropic cost per unit area $\Delta s = \Delta S/A$. Similarly, multiplication of ΔH with packing density allows to estimate the enthalpic gain per unit area $\Delta h = \Delta H/A$. Summation of $-T\Delta s$ with Δh results in the free energy per unit area Δg . Values for the three experimentally observed structures and the hypothetical ideal chickenwire structure are provided in Table 2 for two different solute concentrations.

According to these estimates of Δg , the experimentally observed displaced chickenwire polymorph is thermodynamically more stable than the anticipated hypothetical ideal chickenwire structure. The decisive reason is that for such a large aromatic molecule as TCBPB the interaction with the substrate becomes relatively strong, and a higher packing density facilitates significantly larger Δh from adsorption. This major enthalpic advantage cannot be compensated by the comparatively small enthalpic advantage offered by formation of two ideal O–H \cdots O hydrogen bonds which would lead to a significantly lower packing density. From this pure enthalpic consideration the displaced chickenwire structure is more favorable. But even when the increased entropic cost of the displaced chickenwire structure due to its higher packing density is taken into account, it still remains thermodynamically more stable than the ideal chickenwire structure.

Similarly, Δg values were evaluated for both oblique structures. According to this consideration, the oblique-I structure should be the thermodynamically most stable independent phase, consistent with the experimental observation for higher concentrations. From Table 2 it becomes also obvious that at lower concentrations, the increased translational entropy cost diminishes Δg of the densely packed oblique structures more seriously than for the less densely packed chickenwire structures. Yet, according to these estimates even for dilute solutions, Δg of oblique-I remains more favorable than for the displaced chickenwire structure, posing the question, how can the emergence of the displaced chickenwire polymorph be explained by this thermodynamical model.

In general, coexistence of different monolayer polymorphs over a wide concentration range is a clear experimental indication for similarity of the respective Δg values.⁴¹ In order to rationalize the thermodynamical stability of the displaced chickenwire

(44) Mammen, M.; Shakhnovich, E. I.; Deutch, J. M.; Whitesides, G. M. *J. Org. Chem.* **1998**, *63*, 3821.

structure, further contributions to Δg have to be included. One conceivable additional contribution arises from cooperative effects of cyclic 2-fold C–H···O hydrogen bonds as already discussed above. The cyclic arrangement of the two C–H···O hydrogen bonds allows for resonance assisted hydrogen bonds, similar to the cyclic O–H···O hydrogen bond between carboxylic groups, and RAHB has also been theoretically predicted for weaker C–H···O hydrogen bonds.^{31,32} The fact that all observed structures share the displaced dimer as basic unit can be seen as experimental indication for a relatively high stability of this arrangement. Since the displaced chickenwire structure features three pairs of possibly RAHB stabilized C–H···O hydrogen bonds per unit cell, consideration of this cooperative effect increases the thermodynamic stability of displaced chickenwire with respect to oblique-I.

Second, additional enthalpic contributions from solvation significantly affect the Δg values, and therefore the relative stabilities of distinct monolayer phases. The reference state for our enthalpy estimates are single isolated molecules in vacuum. Yet, upon self-assembly of interfacial monolayers, solute molecules adsorb from the liquid phase where they are dissolved and solvated. The associated solvation enthalpy considerably lowers the effective binding enthalpy, however, this additional enthalpic contribution is very difficult to assess. For tricarboxylic acids dissolved in fatty acid solvents, it is reasonable to assume that each carboxylic group of the solute molecules is saturated by a 2-fold hydrogen bond. Thus, a lower limit for solvation enthalpy is -180 kJ mol^{-1} , i.e. three times the binding enthalpy of a 2-fold O–H···O hydrogen bond. Since solvation significantly reduces the effective enthalpy of adsorption per molecule, this additional contribution weakens the enthalpic gain of densely packed structures more seriously than that of less densely packed structures. Consequently, inclusion of the solvation enthalpy further increases the thermodynamical stability of the displaced chickenwire structure with respect to oblique-I.

Both RAHB of cyclic C–H···O hydrogen bonds and enthalpic contributions from solvation are in principle able to explain the concentration dependent crossover between oblique-I and displaced chickenwire on thermodynamic grounds, while both polymorphs still remain thermodynamically more stable than the ideal chickenwire structure. It is noteworthy, that the applied method of molecule based estimation of enthalpic gains and entropic losses is not sufficiently precise to exactly reproduce concentration dependent crossovers. Nevertheless, our results reproduce a generally observed trend for concentration induced monolayer polymorphism at the liquid solid interface: higher solute concentrations lead to more densely packed monolayer polymorphs. In two recent works by de Feyter et al. and Behm et al. this trend could likewise be explained by thermodynamic models.^{41,45}

Although it is rather complex and challenging to establish a rigid quantitative thermodynamic model for monolayers at the liquid–solid interface, the proposed method at least allows understanding and reproducing trends. In the present case the thermodynamical preference of more densely packed polymorphs over a structure where specifically the intermolecular hydrogen bonds are optimized can be explained.

4. Conclusion

In this work, three different monolayer polymorphs emerged upon adsorption of the enlarged tricarboxylic acid TCBPB from heptanoic acid solution on a graphite surface. All three polymorphs share the same dimer motif as building block and are

nanoporous; i.e., they exhibit a periodic arrangement of cavities. Contrary to monolayer structures observed for smaller tricarboxylic acids, here the dimers are not associated through two strong cyclic O–H···O hydrogen bonds but by two weaker C–H···O hydrogen bonds. This results in a displaced geometry and gives rise to chirality, a phenomenon which has not been encountered before for monolayers of aromatic tricarboxylic acids. Also, the displaced dimer geometry is definitely suboptimal in terms of intermolecular hydrogen bonds, but facilitates higher packing density, and thus a larger contribution from stabilizing molecule–substrate interactions.

During the course of concentration dependent experiments a positive correlation between solute concentration and average surface packing density could clearly be established. For any concentration below 10% saturation only coexistence of all phases was observed, yet, the relative weight of each phase depends on concentration. Interestingly, the two oblique polymorphs exhibit almost identical packing density whereas the displaced chickenwire structure is significantly less dense. Oblique-I is an independent phase, whereas oblique-II was only observed in conjunction with the chickenwire polymorph. The latter two phases feature perfect structural match and can intergrow without strain, thereby providing a possibility to continuously tune the average packing density between those of the pure phases.

The preference of the observed displaced chickenwire structure over the hypothetical ideal chickenwire structure can be understood on thermodynamical grounds: Gibbs free energies per unit area Δg were evaluated for all polymorphs. The entropic cost arises from losses of translational and rotational entropy, and was evaluated by established methods. The enthalpic gain was estimated by combining literature values for intermolecular hydrogen bond energies with a molecular mechanics derived adsorption energy. According to these estimates the hypothetical ideal chickenwire is thermodynamically less favorable than the experimentally observed displaced chickenwire structure. Yet, both densely packed oblique structures are thermodynamically more stable than the displaced chickenwire structure, even at lower concentrations, where the cost due to translational entropy is increased. However, if enthalpic contributions from solvation and cooperative effects of cyclic C–H···O hydrogen bonds are included, the displaced chickenwire can become the thermodynamically favored polymorph at low concentrations. Thermodynamics of molecular monolayers at the liquid–solid interface is a complex problem. For the complete picture, the solution definitely needs to be included. For that reason this problem is difficult to address by atomistic simulations because of the large system size. Nevertheless, semiquantitative considerations as applied in the present case have the potential to at least provide a basic understanding of the main contributions to Gibbs free energy of adsorption and their dependence on external parameters as concentration and temperature.

A major lesson to be learnt from this study is that structure prediction cannot exclusively be based on formation of ideal intermolecular hydrogen bonds. In particular, for larger compounds, the relative enthalpic weight of other contributions as molecule–surface interactions becomes increasingly important and formation of ideal hydrogen bond patterns is not the most important criterion.

Acknowledgment. We gratefully acknowledge financial support by the DFG within the Sonderforschungsbereich 486 and FOR 516 as well as by the cluster of excellence Nanosystems-Initiative-Munich (NIM) and the Bayerische Forschungsförderung.

(45) Meier, C.; Roos, M.; Künzel, D.; Breitruck, A.; Hoster, H. E.; Landfester, K.; Gross, A.; Behm, R. J.; Ziener, U. *J. Phys. Chem. C* **2010**, *114*, 1268.

Note Added after ASAP Publication. This article was published ASAP on June 10, 2010. A new reference (13) has been added to the reference list. The correct version was published on June 15, 2010.

Supporting Information Available: Text discussing the synthesis and NMR characterization of TCBPB, additional STM topographs, detailed hydrogen bonding

scheme, comparison of number of molecules in solution and for monolayer, and translational entropy for concentration changes, including a scheme showing the synthesis and figures showing the NMR spectra, STM topography, bonding patterns, and plot of the number of TCBPB molecules vs relative concentration. This material is available free of charge via the Internet at <http://pubs.acs.org>.

On the Scalability of Supramolecular Systems – High Packing Density vs.

Optimized Hydrogen Bonds in Tricarboxylic Acid Monolayers

Jürgen F. Dienstmaier, Kingsuk Mahata, Wolfgang M. Heckl, Michael Schmittel,

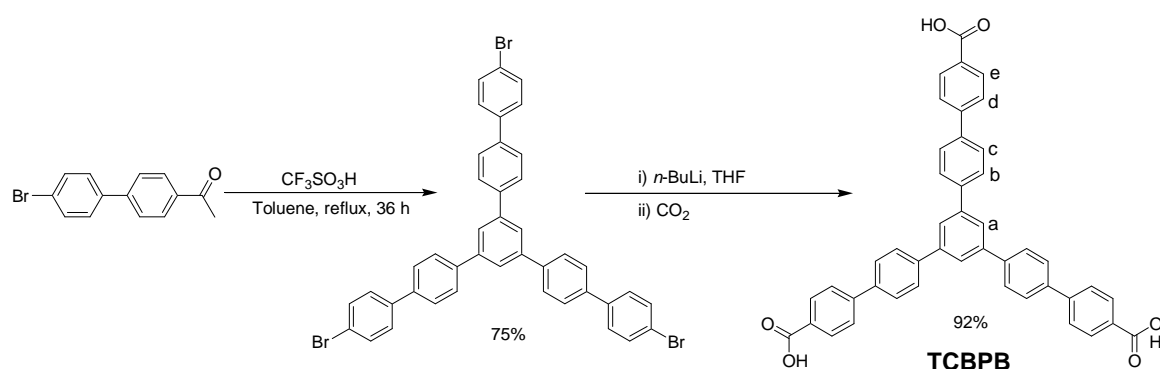
*and Markus Lackinger**

Supporting Information

- (1) Synthesis of 1,3,5-tris[4'-carboxy(1,1'-biphenyl-4-yl)]benzene (TCBPB)**
- (2) Additional STM topographs**
- (3) Hydrogen Bond Pattern for displaced Dimers**
- (4) Number of molecules in solution vs. monolayer**
- (5) Translational entropy loss for changing concentrations**

(1) Synthesis of 1,3,5-tris[4'-carboxy(1,1'-biphenyl-4-yl)]benzene (TCBPB)

^1H NMR and ^{13}C NMR were recorded on a Bruker Avance 400 MHz spectrometer using the deuterated solvent as the lock and residual solvent as the internal reference. NMR measurements were carried out at 298 K. The following abbreviations were utilized to describe peak patterns: s = singlet and d = doublet. The numbering of the carbon atoms of the molecular formula shown in the experimental section is only used for the assignments of the NMR signal and is not in accordance with the IUPAC nomenclature rules. The melting point was measured on a Büchi SMP-20 and the infrared spectrum recorded using a Varian 1000 FT-IR instrument. Elemental analysis measurement was done using a EA 3000 CHNS.



Scheme S1. Synthesis of 1,3,5-tris[4'-carboxy(1,1'-biphenyl-4-yl)]benzene (TCBPB).

1,3,5-Tris(4'-bromobiphenyl-4-yl)benzene was synthesized according to a known procedure.¹

Synthesis of 1,3,5-Tris[4'-carboxy(1,1'-biphenyl-4-yl)]benzene (TCBPB): In an oven-dried three-neck round-bottomed flask 1,3,5-tris(4'-bromobiphenyl-4-yl)benzene (2.01 g, 2.61 mmol) was loaded under nitrogen atmosphere. After addition of dry THF (120 mL), $n\text{-BuLi}$ (6.30 mL, 15.8 mmol) was added slowly at $-60\text{ }^\circ\text{C}$ to $-70\text{ }^\circ\text{C}$ over a period of 30 min. The resultant green solution was stirred for another 6 h at the same temperature. CO_2 gas was passed through the reaction mixture over a period of 30 min maintaining the temperature unchanged. Thereafter, the reaction mixture was allowed to warm up to room temperature with slow purging of CO_2 gas. Excess of $n\text{-BuLi}$ was neutralized using water. The salts were acidified using acetic acid furnishing a clear solution. After removal of THF under reduced pressure a white precipitate was obtained which was filtered off and was dried inside a desiccator. Yield 92%; mp $> 260\text{ }^\circ\text{C}$; ^1H NMR (400 MHz, $\text{THF-}d_8$) δ 7.82 (d, $^3J = 8.4\text{ Hz}$, 6 H,

d-H), 7.86 (d, $^3J = 8.4$ Hz, 6 H, [b/c]-H), 7.95 (d, $^3J = 8.4$ Hz, 6 H, [b/c]-H), 8.03 (s, 3 H, a-H), 8.12 (d, $^3J = 8.4$ Hz, 6 H, e-H); ^{13}C NMR (100 MHz, THF- d_8) δ 125.7, 127.5, 128.4, 128.6, 130.9, 131.1, 140.2, 141.6, 142.8, 145.5, 167.4; IR (KBr) ν 3330-2400, 1683, 1606, 1420, 1271, 1179, 1101, 1004, 822, 772 cm^{-1} ; Anal. Calcd. for $\text{C}_{45}\text{H}_{30}\text{O}_6 \cdot \text{H}_2\text{O}$: C, 78.93; H, 4.71. Found: C, 78.94; H, 4.34.

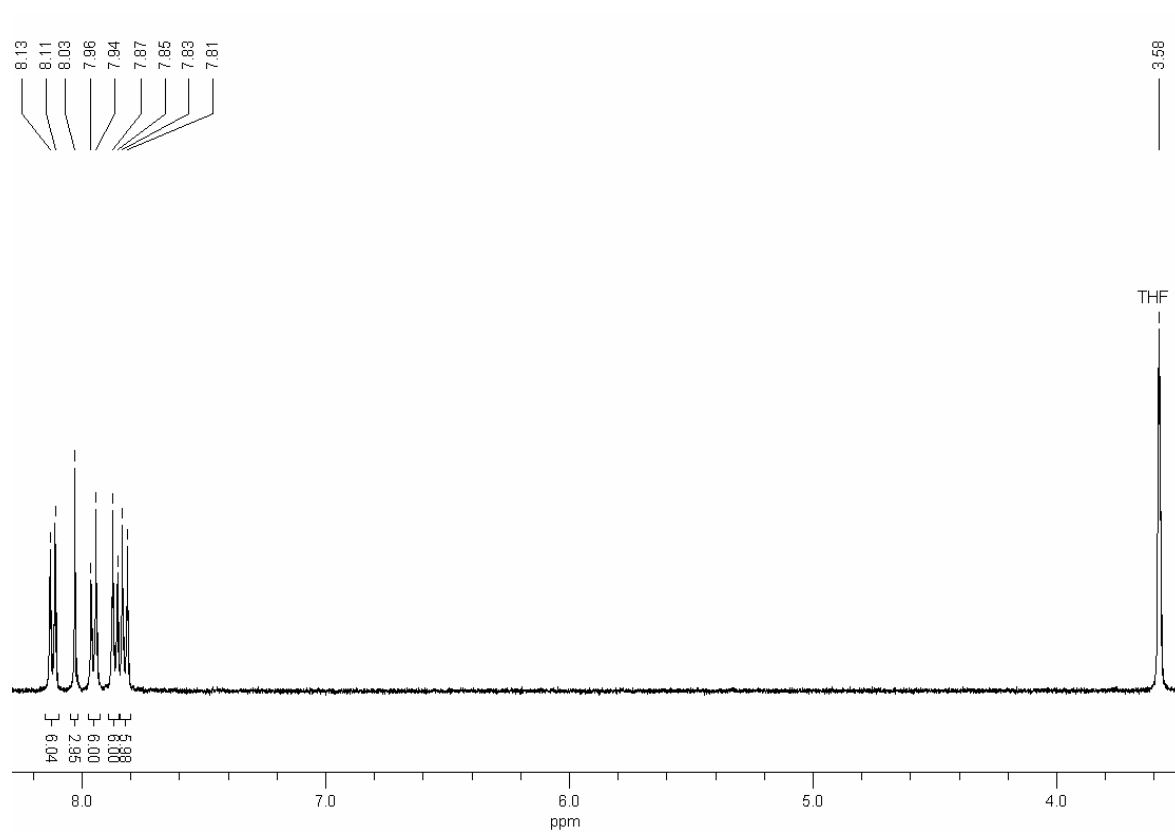


Figure S2. ^1H NMR spectrum (400 MHz, THF- d_8 , 298 K) of TCBPB

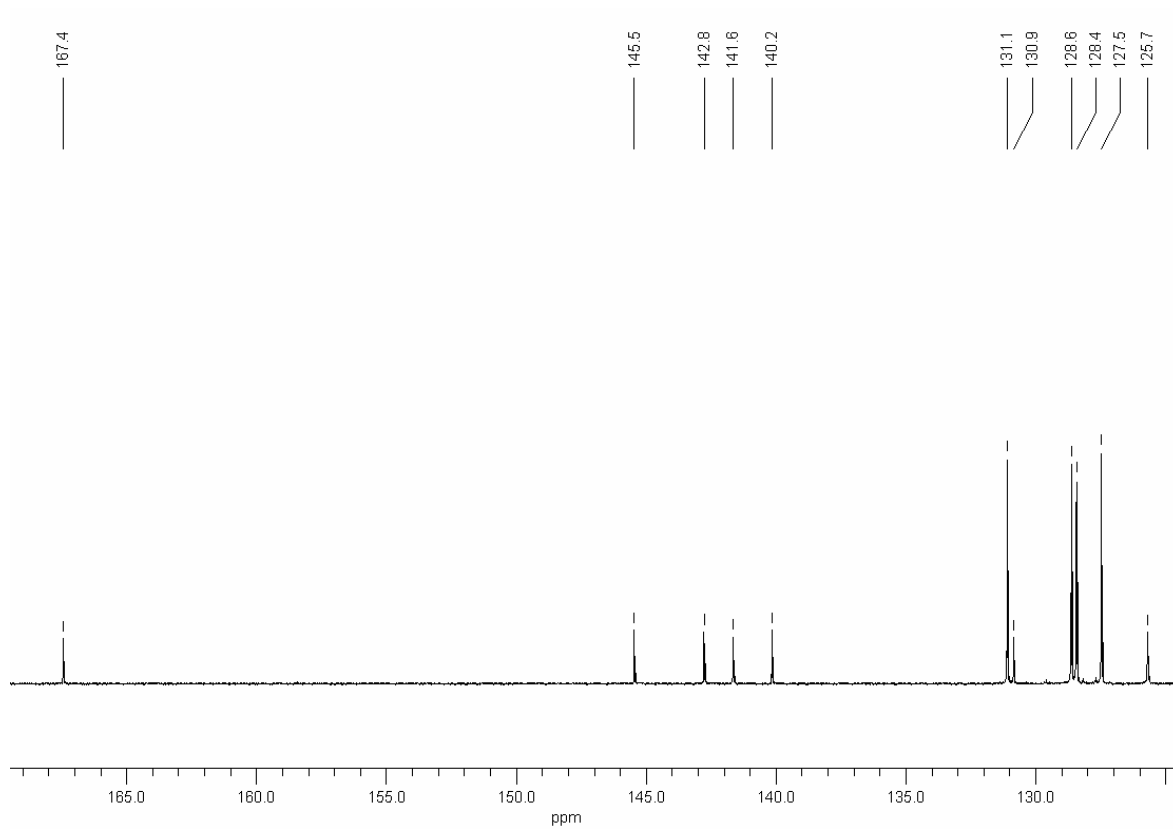


Figure S3. ^{13}C NMR spectrum (100 MHz, $\text{THF-}d_8$, 298 K) of TCBPB.

(2) Additional STM topographs

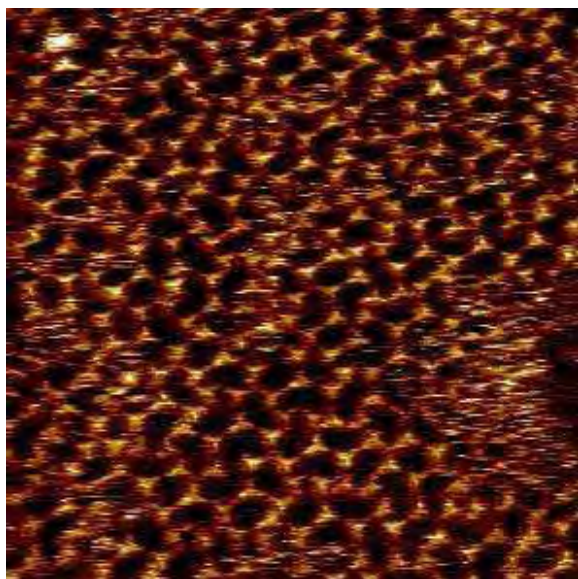


Figure S4 Representative STM topograph ($40 \times 40 \text{ nm}^2$) of the disordered structure found for concentrations between 100% and 35% saturation in 1-undecanol solutions. This image was obtained at a concentration of 35% saturation.

(3) Hydrogen Bond Pattern for displaced Dimers

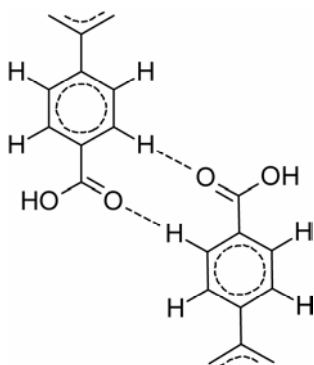


Figure S5 Bonding pattern of the cyclic two-fold C-H...O hydrogen bond between displaced TCBPB dimers. By a cooperative effect known in the literature as “resonance assisted hydrogen bond” (RAHB), the binding energy of cyclic hydrogen bonds is significantly enhanced as compared to twice the binding energy of a single hydrogen bond.

(4) Number of molecules in solution vs. monolayer

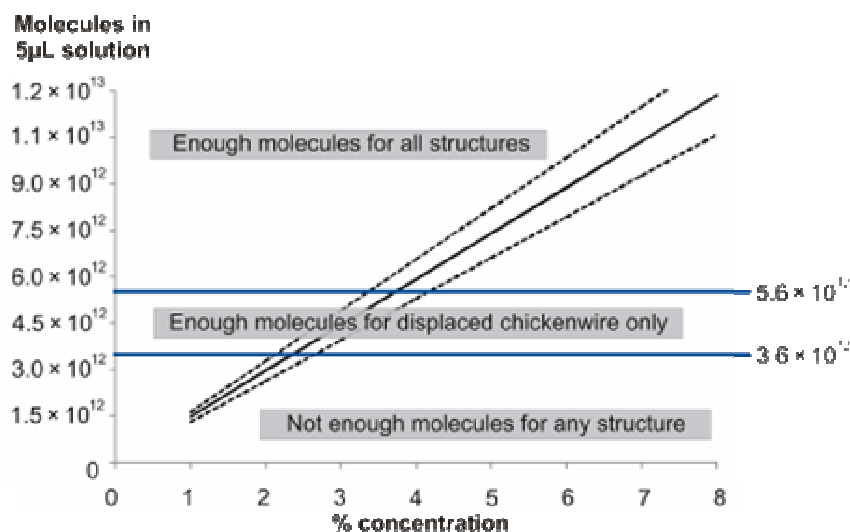


Figure S6 Number of TCBPB molecules in 5 µL TCBPB in heptanoic acid solution as a function of relative concentrations between 1 % and 8 % saturation. For full coverage of a 5×5 mm² HOPG crystal surface, oblique-I and -II require 5.6×10^{12} molecules, whereas displaced chickenwire requires only 3.6×10^{12} molecules. Accordingly, if all dissolved molecules were adsorbed on the surface, for concentrations above ~3.7 %, the oblique phases should have been observed exclusively. However, between 3 % and 7.5 %, all three phases were found in coexistence. The dashed lines indicate the experimental error of the concentration measurement. Notice that below ~2.5 %, no self-assembled structure of TCBPB was found, although the number of dissolved molecules would still be sufficient to at least partly cover the surface.

(5) Translational entropy loss for changing concentrations

The following expression allows evaluation of the loss of translational entropy for the case that the solute concentration changes markedly upon self-assembly:

$$\Delta S_{trans} = k_B \cdot \int_{N_0}^{N_0 - \Delta N} dN \cdot \ln \left[\frac{V}{N} \left(\frac{2\pi \cdot m \cdot k_B T \cdot e^{\frac{5}{3}}}{h^2} \right)^{\frac{3}{2}} \right] \quad (S1)$$

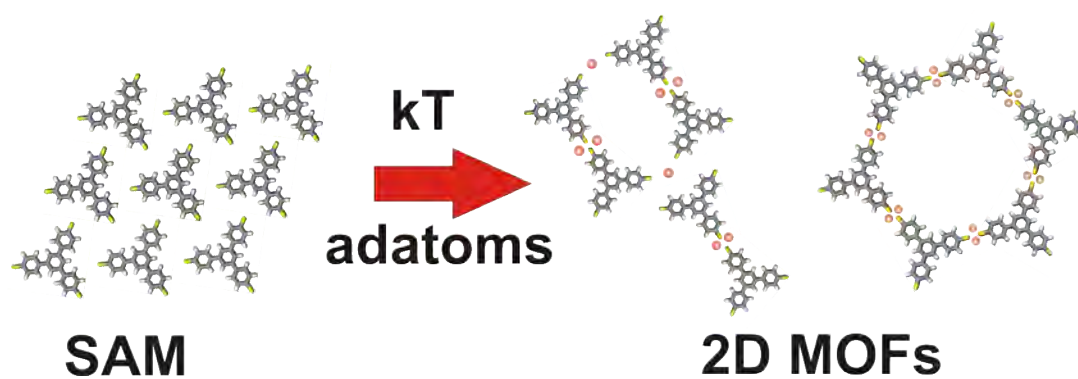
$$\Delta S_{trans} = k_B \cdot \left(\begin{aligned} & (N_0 - \Delta N) \cdot \ln \left[\frac{V}{N_0 - \Delta N} \left(\frac{2\pi \cdot m \cdot k_B T \cdot e^{\frac{5}{3}}}{h^2} \right)^{\frac{3}{2}} \right] - \Delta N \\ & - N_0 \cdot \ln \left[\frac{V}{N_0} \left(\frac{2\pi \cdot m \cdot k_B T \cdot e^{\frac{5}{3}}}{h^2} \right)^{\frac{3}{2}} \right] \end{aligned} \right) \quad (S2)$$

Here N_0 denotes the number of molecules in solution before self-assembly, ΔN the number of molecules adsorbed during self-assembly of a monolayer, and the actual concentration c is expressed as number of molecules N in the solution volume V , i.e. $c = N/V$.

For instance self-assembly of an oblique-I monolayer (5 μL solution on 0.25 cm^2 substrate) causes a rotational entropy loss of 0.168 kJ K^{-1} , whereas the loss of translational entropy amounts to 0.217 kJ K^{-1} for saturated solution and increases to 0.244 kJ K^{-1} for a diluted solution at 4% saturation.

[1] J. Lu, Y. Tao, M. D'iorio, Y. Li, J. Ding, M. Day, *Macromolecules* **2004**, *37*, 2442.

6.5 Extended Two-dimensional Metal-Organic Frameworks Based on Thiolate-Copper Coordination Bonds



submitted

Hermann Walch, Jürgen F. Dienstmaier, Georg Eder, Rico Gutzler, Stefan Schlögl, Kalpataru Das, Michael Schmittel, and Markus Lackinger

Extended Two-Dimensional Metal-Organic Frameworks Based on Thiolate-Copper Coordination Bonds

Hermann Walch^{[a],*}, Jürgen Dienstmaier^[a], Georg Eder^[a], Rico Gutzler^[a], Stefan Schlögl,^[a] Kalpataru Das^[b], Michael Schmittel^[b], and Markus Lackinger^{[a],[c],*}

Molecular electronics not only requires precise electronic function within a single molecule, but equally directional communication between molecules. So far, research is mostly focussed on encoding and studying functionality as for instance rectification or transistor action in single molecular entities.^{[1],[2]} Yet, up to now the issue of interconnecting single molecule devices into more complex circuits is not satisfactorily addressed. Numerous studies concluded that for contacts and interconnects bond topology on the atomic level is of utmost importance due to the coherent nature of electron transport in molecular electronics.^[3] Hence, tools are urgently required that allow to interconnect molecular entities in an atomically defined manner without perturbing or interrupting electronic conjugation. Herein, we present molecular interconnects based on metal-coordination which are topologically well defined, electronically coupled, and also compatible with self-assembly fabrication techniques.

In this communication, we discuss self-assembly of extended fully conjugated two-dimensional (2D) metal-organic frameworks based on thiolate-copper coordination bonds. Although bulk synthesis already yielded comparable copper thiolate metal-organic frameworks^[4] and linear polymeric structures,^[5] this type of interlinking chemistry has not been utilized for surface supported 2D systems. As evident from respective electronic states, organic moieties interconnected by thiolate-copper bonds are electronically coupled, rendering these complexes promising candidates for intermolecular nodes in future integrated molecular electronics.

Subject of this study is adatom mediated coordination of 1,3,5-tris(4-mercaptophenyl)benzene (**TMB**, cf. Figure 1) on Cu(111). Organic molecules with similar triphenylbenzene backbone but

different functionalization can form versatile structures ranging from porous honeycomb^[6] to close-packed networks.^[7] Normally, primarily the functional head groups determine type and strength of intermolecular links. Substrate induced chemistry, however, can also affect intermolecular bonding. For instance on chemically inert substrates (e.g. graphite), carboxylic acids are normally interlinked via cyclic hydrogen bonds,^[8] while on reactive metal surfaces thermally activated deprotonation and subsequent formation of coordination bonds have been observed.^[7] We demonstrate that upon thermal annealing an initial precursor structure is converted into copper-thiolate coordinated networks mediated by the free-adatom gas of the Cu(111) surface.

Room temperature deposition

Thiols are well known to deprotonate upon chemisorption on reactive metal surfaces through a thermally activated process which can be inhibited at low temperatures.^[9] Ethanethiols adsorbed on Cu(111) for instance, already deprotonate above 85 K.^{[10],[11]} The resulting thiolate species then forms covalent bonds with substrate metal atoms.^[10, 12]

In a first preparation step **TMB** is deposited by thermal sublimation under ultra-high vacuum (UHV) conditions on Cu(111) at room temperature and characterized by means of in-situ Scanning Tunneling Microscopy (STM). Figure 1 depicts an STM topograph of the resulting self-assembled close packed trigonal structure with a lattice parameter of (1.30±0.05) nm. Trithiolates originating from full deprotonation of **TMB** adsorb in a planar geometry on Cu(111), whereas monothiolates tend to adsorb upright,^[12a, 13] or inclined, as it is the case for halogen-substituted thiophenols.^[14] For **TMB** planar adsorption offers the energetic advantage of forming three covalent sulfur-copper bonds, albeit in a distorted geometry as compared to upright adsorption. In addition, planar adsorption maximizes interaction of the aromatic triphenylbenzene backbone with the substrate.

In a second preparation step, thermal annealing at 160 – 200 °C for ca. 10 minutes converts the self-assembled trithiolate monolayers into metal-organic coordination networks. Since two different structures emerge, this conversion is not thermodynamically governed. The conversion of the monolayer into the 2D network is accompanied by substantial reorientation and repositioning of **TMB** molecules, but most importantly by introducing intermolecular copper-thiolate coordination bonds. STM topographs of both metal-coordinated structures are depicted in Figure 2.

The effect of annealing is two-fold: first lateral mobility of the trithiolate species is enhanced. Second, the area density of the free copper adatom gas is greatly increased, whereby a sufficient amount of highly mobile coordination centers is supplied.

[a] Mr. H. Walch, Mr. J. Dienstmaier, Mr. G. Eder, Mr. R. Gutzler, Mr. S. Schlögl, Prof. Dr. M. Lackinger
Department for Earth and Environmental Sciences and Center for NanoScience, Ludwig-Maximilians-Universität Theresienstrasse 41, 80333 München, Germany
Fax: (+49 89 2180 4334)
E-mail: markus@lackinger.org
Homepage: <http://www.2d-materials.com/>

[b] Dr. K. Das, Prof. Dr. M. Schmittel
Center of Micro and Nanochemistry and Engineering Organische Chemie I, Universität Siegen
Adolf-Reichwein-Strasse 2, 57068 Siegen, Germany

[c] Deutsches Museum, Museumsinsel 1
80538 München, Germany

[**] Financial Support by the Nanosystems Initiative Munich (NIM) and the Deutsche Forschungsgemeinschaft (FOR516) is gratefully acknowledged



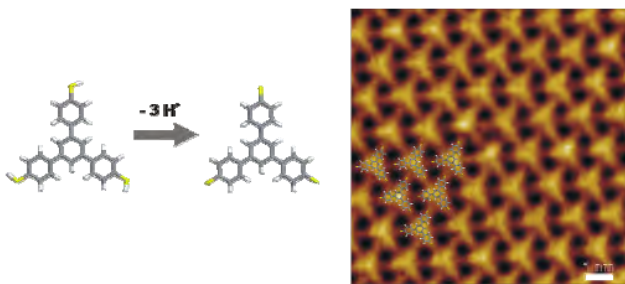


Figure 1. Left: 1,3,5-tris(4-mercaptophenyl)benzene (**TMB**) fully deprotonates upon room temperature adsorption on reactive copper surfaces forming a covalently anchored trithiolate. Right: STM topograph of as deposited TMB on Cu(111) acquired at room temperature ($I_T=185$ pA, $U_T=0.79$ V, image size 10×10 nm², lattice parameters: $a=b=1.30$ nm, $\gamma=120^\circ$)

Formation of extended metal-coordination networks

Generally, 2D metal-coordination networks are prepared either by co-deposition of metal atoms (e.g. Fe, Co)^[15] or by coordination of suitable organic building blocks through freely diffusing adatoms of the substrate.^[16]

The influence of a 2D adatom gas has been recognized as an important contribution to the surface chemistry of metals.^[17] The adatom gas originates from a temperature dependent evaporation / condensation equilibrium at step-edges. At lower temperatures processes with lower activation energies are dominant, i.e. mass transport along step-edges. For higher temperatures a transition occurs, rendering mass exchange between step-edges and terraces the dominant process.^[18] According to Giesen et al., at room temperature the equilibrium concentration of free adatoms and mono-vacancies on Cu and Ag surfaces is in the order of 10^{-9} per surface atom.^[19] Around ~ 500 K the concentration increases drastically by four orders of magnitude to $\sim 10^{-5}$ which corresponds to a astonishingly low area density of 9×10^{-5} adatoms / nm² for Cu(111). Nevertheless, the massive increase in adatom density at moderately elevated temperatures agrees well with the observed onset of metal-organic network formation. Similarly, by means of a variable temperature STM study of tetraazaperpyrene on Cu(111) Matena and coworkers showed that only above a temperature of ~ 150 °C conversion of a hydrogen bonded molecular assembly into a fully metal-coordinated network occurred by the same mechanism.^[16a] A similar observation has been made by Pawin et al. where likewise on Cu(111) initial intermolecular hydrogen bonds are with the aid of adatoms converted into metal coordination-bonds.^[20] Annealing at lower temperatures leads to a partially hydrogen bonded and partially metal-coordinated polymorph. Whereas annealing at higher temperatures results in a fully metal-coordinated structure with substantially higher area density of metal centers. These results and the present study lead to the hypothesis that temperature controlled adatom availability is not only an important requirement for adatom mediated formation of metal-coordination networks, but also a way to steer emergence of various polymorphs.

Recently, the involvement of gold adatoms has also become an established model for the surface anchor bond in alkythiol based Self-Assembled Monolayers on Au(111).^{[21],[22]} Besides, formation of gold-adatom coordinated oligomers and polymers with various coordination geometries have been predicted by means of density functional theory (DFT)^[23] and were also observed by STM for alkanethiol species^[22c] and benzenethiol.^[24]

As already mentioned above, for **TMB** depending on the initial coverage of the trithiolate precursor structure two different

crystalline porous metal-organic networks, a hexagonal honeycomb and an oblique dimer-row structure emerge. STM topographs and corresponding models are depicted in Figure 2. Both structures are metal-organic networks where copper adatoms coordinate **TMB** molecules via their thiolate groups. Thiolate-copper coordination complexes are common and important for biological processing of Cu(I) in proteins.^[25] While surface confined coordination networks based on copper-carboxylate coordination bonds have recently been reported by several groups,^[16, 26] to our knowledge extended 2D networks based on copper-thiolate coordination have not been reported previously.

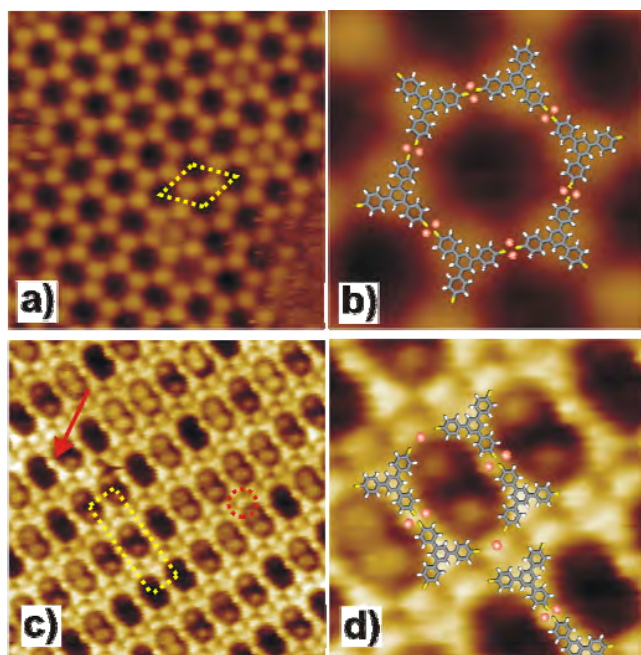


Figure 2. (a) STM topograph of honeycomb structure with unit cell indicated ($U_T=-1.0$ V, $I_T=67$ pA, image size 24×24 nm², lattice parameters: $a=b=3.4$ nm, $\gamma=120^\circ$) and (b) close-up of honeycomb structure with molecular model (c) STM topograph of dimer-row structure with unit cell indicated ($U_T=-0.8$ V, $I_T=121$ pA, image size 18×18 nm², lattice parameters $a=1.9$ nm, $b=6.6$ nm, $\gamma=90^\circ$) and (d) close-up of dimer-row structure with molecular model

The hexagonal honeycomb structure (Figure 2a,b) has a lattice parameter of 3.4 nm and belongs to the plane space group $p6mm$. The second structure is less symmetric (plane space group $c2mm$) and composed of rows of dumbbell shaped dimers. Adjacent dimer rows are offsetted by exactly half a lattice parameter along the row axes, resulting in a centered non-primitive unit cell. The detailed intermolecular bonding scheme of both structures will be discussed in the following.

For a fundamental understanding of the thiolate-copper coordination bonds, DFT calculations have been performed of the connecting nodes, modelled by two phenylthiolates and corresponding copper centers. DFT calculations were conducted with the Gaussian 03 software package.^[27] The B3LYP hybrid functional was used in combination with the 6-31+G* basis set for the elements hydrogen, carbon, and sulfur, and the TZVP basis set for copper. Geometries were optimized for neutral assemblies with atom positions fixed in a plane, allowing equilibration of atomic coordinates only within this plane. Standard convergence criteria were applied. Total binding energies were calculated as the

difference between energies of the geometry optimized complexes and the summed energies of all individually geometry optimized single entities, i.e. phenylthiolate and copper species. Counterpoise correction as included in the Gaussian 03 package did not yield significantly different values, with differences being less than 5 kJ/mol.

Four different intermolecular bonding schemes were considered: metal coordination bonds mediated by one or two copper atoms, and a covalent disulfur bridge. Motivated by the experimental results on thiolate-gold complexes^[22c] both cis and trans arrangements were taken into account for the one-center coordination bonds. For simplicity only the outer phenylthiolate parts were simulated and the explicit substrate influence has been neglected; results are depicted in Fig. 3. Major findings and the resulting association topology can be summarized as follows. Only two-center coordination bonds facilitate linear interconnection. Both, one-center coordination bonds and covalent disulfur bridges result in lateral offsets perpendicular to the bond axis.

Although these simplified model calculations only roughly approximate the substrate's influence by enforced planarity, tendencies concerning association topology and binding energies of the different bonding schemes can be identified. In addition, DFT derived bond lengths can be applied to estimate lattice parameters of resulting metal-organic networks.

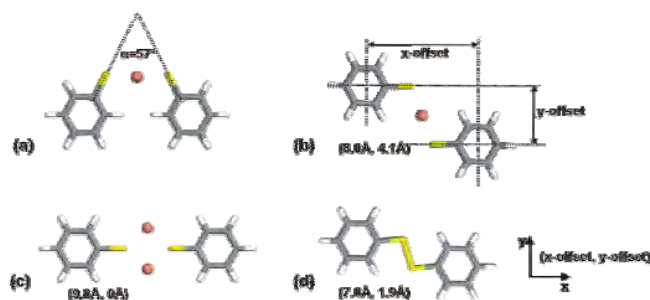


Figure 3. Conceivable intermolecular bonding schemes for interconnected phenylthiolates via (a) one-center cis coordination bond ($\alpha=57^\circ$) (b) one-center trans coordination bond ($x\text{-offset} = 8.0 \text{ \AA}$, $y\text{-offset} = 4.1 \text{ \AA}$) (c) two-center coordination bond ($x\text{-offset} = 9.8 \text{ \AA}$, no $y\text{-offset}$) (d) covalent coupling via disulfur-bridge ($x\text{-offset} = 7.0 \text{ \AA}$, $y\text{-offset} = 1.9 \text{ \AA}$) For all bonds, the center-to-center distance of the phenyl groups ($x\text{-offset}$) and the perpendicular axial offset ($y\text{-offset}$) respectively are given in parenthesis.

Both, the one-center trans coordination bond as well as the disulfur bridge result in a lateral bond offset of $\sim 4.1 \text{ \AA}$ and $\sim 1.9 \text{ \AA}$, respectively. In the one-center cis coordination bond the molecular axes include an angle of 57° , which is significantly larger than about 35° reported for Au coordinated methylthiolate by Voznyy and coworkers.^[22c] This can readily be explained by steric repulsion, being more pronounced for the bulky phenyl ligands as compared to methyl groups.

According to DFT results, the total binding energy of two-center coordination complexes is strongest with a value of 555 kJ/mol. Total binding energies of cis (394 kJ/mol) and trans (397 kJ/mol) one-center coordination complexes are comparable, but notably lower than for the two-center complex. The covalent disulfur bridge is the weakest bond with a strength of 151 kJ/mol. Covalent S-S bonds exhibit a certain variability of bond angles and energies,^[28] with the latter value being within the usual range.

Occasionally, specific tip states result in STM contrasts, where protruding features midst between dimers can be observed. Such faint protrusions can also be identified in Figure 2c at the center between two **TMB** molecules constituting a dimer, as marked by the arrow. Comparable contrast features were similarly observed in other studies and are interpreted as signature of metal-coordination complexes.^[29] However, based on high resolution STM images it is not unambiguous to distinguish between one- and two-center coordination bonds. Yet, a distinction can be made by comparison between experimental and theoretical bond lengths and geometries.

Both the honeycomb and the dimer-row structure contain dumbbell shaped **TMB** dimers as basic structural motif. In high resolution STM images of both structures no lateral displacement can be discerned along the dimer axis, further evidence for a two-center coordination bond. This conclusion is substantiated by comparison of experimental and theoretical bond lengths. STM data yield a center-to-center distance of $2.0 (\pm 0.2) \text{ nm}$ between two **TMB** molecules in the dimer. DFT results in combination with the intramolecular distance between central and outer phenyl rings in **TMB** (0.46 nm for a geometry optimized isolated molecule) postulate a dimer center-to-center distance of 1.90 nm . Accordingly, the experimental lattice parameter of the honeycomb structure ($(3.4 \pm 0.2) \text{ nm}$) is in good agreement with the anticipated lattice parameter from the two-center coordination interconnect (3.3 nm), while both the one-center coordination bond (2.9 nm) and the covalent disulfur bridge (2.8 nm) would yield notably smaller lattice parameters. From its symmetry it can be concluded that all intermolecular bonds in the honeycomb structure are equivalent. Consequently, one unit cell contains two fully thiolated **TMB** molecules and six copper centers, yielding area densities of $0.20 \text{ molecules/nm}^2$ and 0.6 adatoms/nm^2 .

Yet, due to its lower symmetry the dimer-row structure cannot consistently be explained solely based on two-center coordination bonds. Thus, a bonding scheme is proposed involving different types of intermolecular bonds. Both appearance and center-to-center distance of dimers ($\sim 2.0 \text{ nm}$) within the rows are similar to the honeycomb structure. Hence, it is concluded that also dimers of the dimer-row structure are again interconnected by two-center coordination bonds. These dimers assemble in parallel rows, where adjacent rows are shifted half a lattice parameter with respect to the row direction. STM topographs exhibit protruding contrast features directly above and below intrarow neighbors (marked in Figure 2c by a dashed circle) which point towards cis coordination bonds. In the model in Figure 2d one-center cis coordination bonds are implemented. In this case the S-Cu-S angle would be around 120° which does not correspond to 57° obtained by our DFT calculations of isolated dimers. Yet, the DFT simulations do not include explicit substrate effects and packing requirements. Considering the weak angular dependence of the coordination bond energy, significant deviations of the bond angle are conceivable.

Besides, and consistent with other works, the coordinating copper atoms cannot be resolved separately, as it is also the case for the two adatoms coordinating bonds within dimers. However, dimer-dimer coordination by more than one Cu atom cannot be excluded which could also be the reason for the obtuse angle suggested by the tentative molecular overlay. Polynuclear copper-thiolate coordination bonds are common,^[30] where coordinating copper clusters are further stabilized by cuprophilicity.^[31] For instance, coordination by Cu_3 clusters has also been observed previously for bulk systems.^[4] Based on the proposed one atom coordination model we obtain area densities of $0.32 \text{ molecules/nm}^2$, which is significantly higher as compared to the honeycomb

structure and $0.65 \text{ adatoms/nm}^2$, which is comparable to the adatom density in the honeycomb structure.

For both structures contrast features within the pores are frequently observed, albeit without molecular resolution. In accord with other studies on porous networks,^[32] these features are interpreted as trapped molecules or adatoms which are not stabilized by inclusion into the network. Hence, the trapped species remains mobile and cannot be resolved by STM at room temperature.

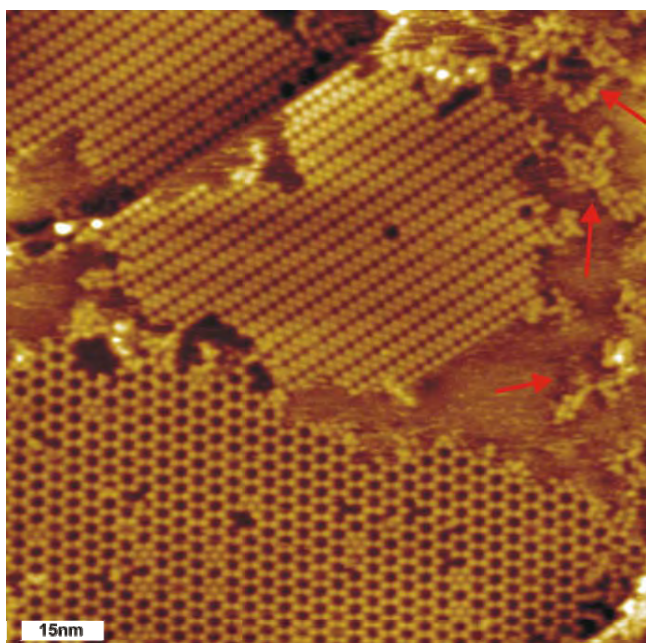


Figure 4. Overview STM image illustrating the coexistence of both phases. ($U_T = -1.64 \text{ V}$, $I_T = 66 \text{ pA}$, image size $116 \times 116 \text{ nm}^2$) Red arrows indicate first occurrence of degraded molecules starting at annealing temperatures around 220°C

Both honeycomb and dimer-row structure were observed in coexistence. The relative ratio of both phases slightly depends on the initial coverage of the precursor structure, with a preference for the more densely packed dimer-row structure at higher coverages. The packing density of the initial self-assembled trithiolate structure amounts to $0.63 \text{ molecules/nm}^2$. Since both metal-coordinated structures exhibit lower molecular packing densities (honeycomb: $0.20 \text{ molecules/nm}^2$, dimer-row: $0.33 \text{ molecules/nm}^2$), conversion results in expansion and increasing coverage. Consequently, in order to obtain full monolayer coverage of the honeycomb (dimer-row) structure the initial coverage must nominally not exceed 0.32 (0.52) monolayers (ignoring possible desorption and inclusion in cavities). Coexistence of both phases can be taken as a hint for rather similar thermodynamic stability of both structures.^[33] Yet, according to these simple packing arguments, we propose that initial coverage of the precursor structure in concert with kinetic factors is important for the structural outcome of the interconversion process.

In order to study thermal stability of thiolate-copper metal-coordination networks further annealing experiments were conducted. Thermal treatment at slightly higher temperatures of $\sim 220^\circ\text{C}$ already leads to the onset of degradation, indicated by the red arrows in Figure 4. Annealing at 300°C and higher results in complete deterioration of the networks, where only amorphous molecular films remain.

In order to illustrate the electronic properties of the copper-thiolate metal-coordination interlink, DFT derived frontier molecular orbitals are depicted in Fig. 5. Evidently, both highest occupied molecular orbital (HOMO) and lowest unoccupied molecular orbital (LUMO) of bicoordinated phenylthiolates exhibit intensity at the bond site. The LUMO wavefunction appears to be more localized at the bond, whereas the HOMO wavefunction is evenly distributed across the metal-coordination complex. Such delocalization allows for coherent electron transport through the metal-coordination bond, rendering this interconnection chemistry a suitable candidate for interlinking single molecules into more complex molecular electronics circuitry.

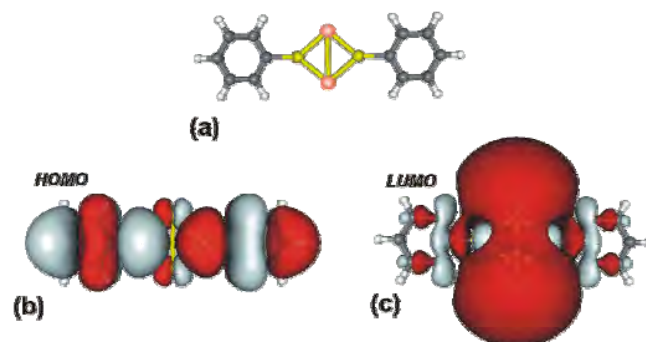


Figure 5. DFT results of structure and frontier molecular orbitals of a two-center coordination bond interconnecting two phenylthiolates (a) geometry optimized structure (b) HOMO of the complex, indicating a pronounced conjugation between the organic moieties through the metal-coordination bond (c) LUMO of the complex, exhibiting a pronounced localization in the vicinity of the coordination bond. (red and grey colours represent regions of negative and positive sign of molecular orbitals, respectively.)

In summary, copper-thiolate based 2D metal-organic frameworks were synthesized in a two-step process. First, after thermal sublimation aromatic trithiols adsorb planar on Cu(111), deprotonate and self-assemble into trigonal trithiolate domains. In a second step thermal annealing converts this precursor structure into metal-organic frameworks. An annealing temperature between $160 - 200^\circ\text{C}$ was necessary to initiate molecular diffusion in combination with a sufficient supply of adatoms, resulting in two different metal-coordinated phases. The two observed metal-organic networks are based on coordinative bonds between thiolates and either one or two copper adatoms. Comparison between DFT derived and experimental bond lengths aided in the identification of intermolecular coordination bonds. Copper-thiolate complexes were found to be electronically conjugated, thus rendering thiol groups not only useful as electrode anchor groups in molecular electronics, but also valuable for interlinks between single molecule devices.

Experimental Section

All samples were prepared and characterized in an ultrahigh-vacuum chamber (base pressure $< 5 \times 10^{-10} \text{ mbar}$) equipped with an Omicron VT Scanning Tunneling Microscope (STM). The Cu(111) single crystal was prepared by subsequent cycles of Ar^+ -ion sputtering and annealing at 820 K . 1,3,5-Tris(4-mercaptophenyl)benzene (TMB) was thermally evaporated from a home-built Knudsen cell with crucible temperatures around 145°C . During deposition and imaging the substrate was held at room temperature.

Synthesis of TMB:^[34] Solid NaSMe (0.395 g , 5.64 mmol) was added in one portion to a solution of 1,3,5-tris(4-bromophenyl)benzene (1.00

g, 1.84 mmol) in dry DMF (35 mL). The reaction mixture was stirred for 1 h at 150 °C. Additional NaSMe (0.395 g, 5.64 mmol) was added, heating was continued for 1 h, and then a third portion of NaSMe (0.395 g, 5.64 mmol) was added to the reaction. The mixture was heated at 150 °C for another 6 h, cooled to 40 °C, and diluted with acetic acid (1.30 mL) and water (39.0 mL). The product forms as a pale gray precipitate, which was filtered, washed with water, and dried in vacuum to afford pure 1,3,5-tris(4-mercaptophenyl)benzene (0.650 g, 88%), mp 179-180 °C (uncorrected). IR (film / cm⁻¹): 3055 (m), 2987 (w), 2306 (w), 1422 (m), 1264 (s), 896 (m), 751 (s); ¹H NMR (CD₂Cl₂, 400 MHz): δ 7.71 (s, 3H), 7.58 (d, J = 8.3 Hz, 6H), 7.38 (d, J = 8.3 Hz, 6H), 3.62 (s, 3H). ¹³C NMR (CD₂Cl₂, 100 MHz): δ 141.8, 138.5, 131.0, 129.9, 128.2, 124.7. Elemental anal. for C₂₄H₁₈S₃: Calcd. C 71.60, H 4.51, S 23.89; found C 71.46, H 4.49, S 24.27.

Received: ((will be filled in by the editorial staff))

Published online on ((will be filled in by the editorial staff))

Keywords: 2D metal-organic frameworks · thiolate-copper coordination · 2D adatom gas · Scanning Tunneling Microscopy · surface chemistry

- [1] K. E. Heller, A. F. Shugart, F. A. Lohmann, J. Darcy, H. F. Roessle, E. D. Decastro, W. E. Terry, E. Wantland, T. Sasaki, J. L. Sprague, G. E. Moore, J. Clark, Y. Ishii, G. L. Tooker, J. D. Bowen, A. J. Stein, J. Towne, C. M. Clough, E. Harrison, *Electronics* **1982**, *55*, 118-127.
- [2] a)M. C. Petty, *Molecular electronics : from principles to practice*, John Wiley & Sons, Chichester, England ; Hoboken, NJ, **2007**; b)C. Joachim, J. K. Gimzewski, A. Aviram, *Nature* **2000**, *408*, 541-548.
- [3] a)K. W. Hipps, *Science* **2001**, *294*, 536-537; b)K. Stokbro, J. Taylor, M. Brandbyge, J. L. Mozos, P. Ordejón, *Comp Mater Sci* **2003**, *27*, 151-160; c)V. V. Zhirmov, R. K. Cavin, *Nat Mater* **2006**, *5*, 11-12.
- [4] J. He, C. Yang, Z. T. Xu, M. Zeller, A. D. Hunter, J. H. Lin, *J Solid State Chem* **2009**, *182*, 1821-1826.
- [5] C. M. Che, C. H. Li, S. S. Y. Chui, V. A. L. Roy, K. H. Low, *Chem-Eur J* **2008**, *14*, 2965-2975.
- [6] L. Kampschulte, M. Lackinger, A. K. Maier, R. S. K. Kishore, S. Griessl, M. Schmittel, W. M. Heckl, *J Phys Chem B* **2006**, *110*, 10829-10836.
- [7] M. Ruben, D. Payer, A. Landa, A. Comisso, C. Gattinoni, N. Lin, J. P. Collin, J. P. Sauvage, A. De Vita, K. Kern, *J Am Chem Soc* **2006**, *128*, 15644-15651.
- [8] M. Lackinger, W. M. Heckl, *Langmuir* **2009**, *25*, 11307-11321.
- [9] L. Kankate, A. Turchanin, A. Golzhauser, *Langmuir* **2009**, *25*, 10435-10438.
- [10] S. A. Sardar, J. A. Syed, E. Ikenaga, S. Yagi, T. Sekitani, S. Wada, M. Taniguchi, K. Tanaka, *Nucl Instrum Meth B* **2003**, *199*, 240-243.
- [11] P. Maksymovych, D. C. Sorescu, J. T. Yates, *Phys Rev Lett* **2006**, *97*, 146103.
- [12] a)M. Konopka, R. Turansky, M. Dubecky, D. Marx, I. Stich, *J Phys Chem C* **2009**, *113*, 8878-8887; b)S. M. Driver, D. P. Woodruff, *Surf Sci* **2000**, *457*, 11-23; c)H. Keller, P. Simak, W. Schrepp, J. Dembowski, *Thin Solid Films* **1994**, *244*, 799-805; d)A. Ferral, P. Paredes-Olivera, V. A. Macagno, E. M. Patrito, *Surf Sci* **2003**, *525*, 85-99.
- [13] V. Di Castro, F. Bussolotti, C. Mariani, *Surf Sci* **2005**, *598*, 218-225.
- [14] K. L. Wong, X. Lin, K. Y. Kwon, G. Pawin, B. V. Rao, A. Liu, L. Bartels, S. Stolbov, T. S. Rahman, *Langmuir* **2004**, *20*, 10928-10934.
- [15] a)S. Stepanow, N. Lin, J. V. Barth, K. Kern, *J Phys Chem B* **2006**, *110*, 23472-23477; b)Y. F. Zhang, N. Zhu, T. Komeda, *Surf Sci* **2008**, *602*, 614-619; c)S. Stepanow, M. Lingenfelder, A. Dmitriev, H. Spillmann, E. Delvigne, N. Lin, X. B. Deng, C. Z. Cai, J. V. Barth, K. Kern, *Nat Mater* **2004**, *3*, 229-233; d)U. Schlickum, R. Decker, F. Klappenberger, G. Zoppellaro, S. Klyatskaya, M. Ruben, I. Silanes, A. Arnau, K. Kern, H. Brune, J. V. Barth, *Nano Lett* **2007**, *7*, 3813-3817.
- [16] a)M. Matena, M. Stohr, T. Riehm, J. Bjork, S. Martens, M. S. Dyer, M. Persson, J. Lobo-Checa, K. Muller, M. Enache, H. Wadepohl, J. Zegehnagen, T. A. Jung, L. H. Gade, *Chem-Eur J* **2010**, *16*, 2079-2091; b)C. C. Perry, S. Haq, B. G. Frederick, N. V. Richardson, *Surf Sci* **1998**, *409*, 512-520.
- [17] N. Lin, D. Payer, A. Dmitriev, T. Strunskus, C. Woll, J. V. Barth, K. Kern, *Angewandte Chemie-International Edition* **2005**, *44*, 1488-1491.
- [18] M. Giesen, *Surf Sci* **1999**, *442*, 543-549.
- [19] M. Giesen, *Prog Surf Sci* **2001**, *68*, 1-153.
- [20] G. Pawin, K. L. Wong, D. Kim, D. Z. Sun, L. Bartels, S. Hong, T. S. Rahman, R. Carp, M. Marsella, *Angewandte Chemie-International Edition* **2008**, *47*, 8442-8445.
- [21] a)F. Schreiber, *Prog Surf Sci* **2000**, *65*, 151-256; b)J. C. Love, L. A. Estroff, J. K. Kriebel, R. G. Nuzzo, G. M. Whitesides, *Chem Rev* **2005**, *105*, 1103-1169.
- [22] a)R. Mazzarello, A. Cossaro, A. Verdini, R. Rousseau, L. Casalis, M. F. Danisman, L. Floreano, S. Scandolo, A. Morgante, G. Scoles, *Phys Rev Lett* **2007**, *98*, -; b)P. Maksymovych, D. C. Sorescu, J. T. Yates, *Phys Rev Lett* **2006**, *97*, 146103; c)O. Voznyy, J. J. Dubowski, J. T. Yates, P. Maksymovych, *J Am Chem Soc* **2009**, *131*, 12989-12993.
- [23] D. E. Jiang, S. Dai, *J Phys Chem C* **2009**, *113*, 7838-7842.
- [24] P. Maksymovych, J. T. Yates, *J Am Chem Soc* **2008**, *130*, 7518-7519.
- [25] N. Romero-Isart, M. Vasak, *J Inorg Biochem* **2002**, *88*, 388-396.
- [26] a)J. V. Barth, J. Weckesser, N. Lin, A. Dmitriev, K. Kern, *Appl Phys a-Mater* **2003**, *76*, 645-652; b)N. Lin, A. Dmitriev, J. Weckesser, J. V. Barth, K. Kern, *Angewandte Chemie-International Edition* **2002**, *41*, 4779-4783; c)D. B. Dougherty, P. Maksymovych, J. T. Yates, *Surf Sci* **2006**, *600*, 4484-4491.
- [27] M. J. Frisch, *Chem Listy* **2006**, *100*, A9-A9.
- [28] R. Steudel, *Angew Chem Int Edit* **1975**, *14*, 655-664.
- [29] S. Stepanow, N. Lin, J. V. Barth, *J Phys-Condens Mat* **2008**, *20*, -.
- [30] P. Ahte, P. Palumaa, T. Tamm, *J Phys Chem A* **2009**, *113*, 9157-9164.
- [31] H. L. Hermann, G. Boche, P. Schwerdtfeger, *Chem-Eur J* **2001**, *7*, 5333-5342.
- [32] S. Stepanow, N. Lin, D. Payer, U. Schlickum, F. Klappenberger, G. Zoppellaro, M. Ruben, H. Brune, J. V. Barth, K. Kern, *Angewandte Chemie-International Edition* **2007**, *46*, 710-713.
- [33] S. B. Lei, K. Tahara, F. C. De Schryver, M. Van der Auweraer, Y. Tobe, S. De Feyter, *Angewandte Chemie-International Edition* **2008**, *47*, 2964-2968.
- [34] M. V. Ovchinnikov, B. J. Holliday, C. A. Mirkin, L. N. Zakharov, A. L. Rheingold, *P Natl Acad Sci USA* **2002**, *99*, 4927-4931.

References

- [1] Peter Grütter, Werner Hofer, and Federico Rosei. *Properties of single organic molecules on crystal surfaces*. Imperial College Press ; Distributed by World Scientific, London Singapore ; Hackensack, NJ, 2006.
- [2] J. C. Love, L. A. Estroff, J. K. Kriebel, R. G. Nuzzo, and G. M. Whitesides. Self-assembled monolayers of thiolates on metals as a form of nanotechnology. *Chemical Reviews*, 105(4):1103–1169, 2005.
- [3] J. Seto, N. Asai, I. Fujiwara, T. Ishibashi, T. Kamei, and S. Tamura. Functional organic ultra-thin films for device applications. *Thin Solid Films*, 273(1-2):97–104, 1996.
- [4] T. Sano, H. Fujii, Y. Nishio, Y. Hamada, H. Takahashi, and K. Shibata. Organic electroluminescent devices doped with condensed polycyclic aromatic compounds. *Synthetic Metals*, 91(1-3):27–30, 1997.
- [5] L. Schmidt-Mende, A. Fechtenkotter, K. Mullen, E. Moons, R. H. Friend, and J. D. MacKenzie. Self-organized discotic liquid crystals for high-efficiency organic photovoltaics. *Science*, 293(5532):1119–1122, 2001.
- [6] A. Dmitriev, H. Spillmann, N. Lin, J. V. Barth, and K. Kern. Modular assembly of two-dimensional metal-organic coordination networks at a metal surface. *Angewandte Chemie-International Edition*, 42(23):2670–2673, 2003.
- [7] G. E. Moore. Cramming more components onto integrated circuits (Reprinted from *Electronics*, pg 114-117, April 19, 1965). *Proceedings of the Ieee*, 86(1): 82–85, 1998.
- [8] A. Aviram and M. A. Ratner. Molecular Rectifiers. *Chemical Physics Letters*, 29(2):277–283, 1974.
- [9] C. Joachim, J. K. Gimzewski, and A. Aviram. Electronics using hybrid-molecular and mono-molecular devices. *Nature*, 408(6812):541–548, 2000.
- [10] J. R. Heath and M. A. Ratner. Molecular electronics. *Physics Today*, 56(5): 43–49, 2003.
- [11] M. A. Reed, C. Zhou, C. J. Muller, T. P. Burgin, and J. M. Tour. Conductance of a molecular junction. *Science*, 278(5336):252–254, 1997.
- [12] X. D. Cui, A. Primak, X. Zarate, J. Tomfohr, O. F. Sankey, A. L. Moore, T. A. Moore, D. Gust, G. Harris, and S. M. Lindsay. Reproducible measurement of single-molecule conductivity. *Science*, 294(5542):571–574, 2001.

- [13] M. Forshaw, R. Stadler, D. Crawley, and K. Nikolic. A short review of nano-electronic architectures. *Nanotechnology*, 15(4):S220–S223, 2004.
- [14] S. Iijima. Helical Microtubules of Graphitic Carbon. *Nature*, 354(6348):56–58, 1991.
- [15] J. Chen, M. A. Reed, A. M. Rawlett, and J. M. Tour. Large on-off ratios and negative differential resistance in a molecular electronic device. *Science*, 286(5444):1550–1552, 1999.
- [16] G. A. Prinz. Device physics - Magnetoelectronics. *Science*, 282(5394):1660–1663, 1998.
- [17] G. M. Whitesides, J. P. Mathias, and C. T. Seto. Molecular Self-Assembly and Nanochemistry - a Chemical Strategy for the Synthesis of Nanostructures. *Science*, 254(5036):1312–1319, 1991.
- [18] D. M. Eigler and E. K. Schweizer. Positioning Single Atoms with a Scanning Tunneling Microscope. *Nature*, 344(6266):524–526, 1990.
- [19] B. Neu, G. Meyer, and K. H. Rieder. Controlled Vertical and Lateral Manipulation of Single Atoms and Molecules with the Scanning Tunneling Microscope. *Modern Physics Letters B*, 9(15):963–969, 1995.
- [20] T. A. Jung, R. R. Schlittler, J. K. Gimzewski, H. Tang, and C. Joachim. Controlled room-temperature positioning of individual molecules: Molecular flexure and motion. *Science*, 271(5246):181–184, 1996.
- [21] R. Otero, F. Rosei, and F. Besenbacher. Scanningtunneling microscopy manipulation of complex organic molecules on solid surfaces. *Annual Review of Physical Chemistry*, 57:497–525, 2006.
- [22] J. V. Barth. Molecular architectonic on metal surfaces. *Annual Review of Physical Chemistry*, 58:375–407, 2007.
- [23] S. Stepanow, N. Lin, and J. V. Barth. Modular assembly of low-dimensional coordination architectures on metal surfaces. *Journal of Physics-Condensed Matter*, 20(18):184002, 2008.
- [24] D. F. Perepichka and F. Rosei. CHEMISTRY Extending Polymer Conjugation into the Second Dimension. *Science*, 323(5911):216–217, 2009.
- [25] A. Gourdon. On-surface covalent coupling in ultrahigh vacuum. *Angewandte Chemie-International Edition*, 47(37):6950–6953, 2008.
- [26] J. Sakamoto, J. van Heijst, O. Lukin, and A. D. Schluter. Two-Dimensional Polymers: Just a Dream of Synthetic Chemists? *Angewandte Chemie-International Edition*, 48(6):1030–1069, 2009.
- [27] S. J. H. Griessl, M. Lackinger, F. Jamitzky, T. Markert, M. Hietschold, and W. A. Heckl. Incorporation and manipulation of coronene in an organic template structure. *Langmuir*, 20(21):9403–9407, 2004.

-
- [28] M. Lackinger, S. Griessl, T. Markert, F. Jamitzky, and W. M. Heckl. Self-assembly of benzene-dicarboxylic acid isomers at the liquid solid interface: Steric aspects of hydrogen bonding. *Journal of Physical Chemistry B*, 108(36):13652–13655, 2004.
- [29] S. W. Hla, G. Meyer, and K. H. Rieder. Selective bond breaking of single iodobenzene molecules with a scanning tunneling microscope tip. *Chemical Physics Letters*, 370(3-4):431–436, 2003.
- [30] B. J. McIntyre, M. Salmeron, and G. A. Somorjai. A Variable Pressure Temperature Scanning Tunneling Microscope for Surface Science and Catalysis Studies. *Review of Scientific Instruments*, 64(3):687–691, 1993.
- [31] F. Tao, D. Tang, M. Salmeron, and G. A. Somorjai. A new scanning tunneling microscope reactor used for high-pressure and high-temperature catalysis studies. *Review of Scientific Instruments*, 79(8):–, 2008.
- [32] R. Young, J. Ward, and F. Scire. Topografiner - Instrument for Measuring Surface Microtopography. *Review of Scientific Instruments*, 43(7):999–, 1972.
- [33] E. C. Teague. Room-Temperature Gold-Vacuum-Gold Tunneling Experiments. *Bulletin of the American Physical Society*, 23(3):290–290, 1978.
- [34] A. D. Gottlieb and L. Wesoloski. Bardeen’s tunnelling theory as applied to scanning tunnelling microscopy: a technical guide to the traditional interpretation. *Nanotechnology*, 17(8):R57–R65, 2006.
- [35] G. Binnig and H. Rohrer. Vacuum Tunnel Microscope. *Helvetica Physica Acta*, 55(2):128–128, 1982.
- [36] M. J. Rost, L. Crama, P. Schakel, E. van Tol, G. B. E. M. van Velzen-Williams, C. F. Overgaw, H. ter Horst, H. Dekker, B. Okhuijsen, M. Seynen, A. Vijftigschild, P. Han, A. J. Katan, K. Schoots, R. Schumm, W. van Loo, T. H. Oosterkamp, and J. W. M. Frenken. Scanning probe microscopes go video rate and beyond. *Review of Scientific Instruments*, 76(5):053710, 2005.
- [37] Frank Trixler. *Erzeugung organischer Halbleiter-Nanostrukturen durch Festphasenbenetzung*. PhD thesis, Ludwig-Maximilians-University Munich, 2007.
- [38] C. Julian Chen. *Introduction to scanning tunneling microscopy*. Oxford series in optical and imaging sciences 4. Oxford University Press, New York, 1993.
- [39] D. Drakova. Theoretical modelling of scanning tunnelling microscopy, scanning tunnelling spectroscopy and atomic force microscopy. *Reports on Progress in Physics*, 64(2):205–290, 2001.
- [40] J. Tersoff and D. R. Hamann. Theory and Application for the Scanning Tunneling Microscope. *Physical Review Letters*, 50(25):1998–2001, 1983.
- [41] J. Tersoff and D. R. Hamann. Theory of the Scanning Tunneling Microscope. *Physical Review B*, 31(2):805–813, 1985.

- [42] X. H. Lu, M. Grobis, K. H. Khoo, S. G. Louie, and M. F. Crommie. Spatially mapping the spectral density of a single C-60 molecule. *Physical Review Letters*, 90(9):096802, 2003.
- [43] A. Scarfato, S. H. Chang, S. Kuck, J. Brede, G. Hoffmann, and R. Wiesendanger. Scanning tunneling microscope study of iron(II) phthalocyanine growth on metals and insulating surfaces. *Surface Science*, 602(3):677–683, 2008.
- [44] C. J. Villagomez, T. Zambelli, S. Gauthier, A. Gourdon, S. Stojkovic, and C. Joachim. STM images of a large organic molecule adsorbed on a bare metal substrate or on a thin insulating layer: Visualization of HOMO and LUMO. *Surface Science*, 603(10-12):1526–1532, 2009.
- [45] C. J. Villagomez, T. Zambelli, S. Gauthier, A. Gourdon, C. Barthes, S. Stojkovic, and C. Joachim. A local view on hyperconjugation. *Chemical Physics Letters*, 450(1-3):107–111, 2007.
- [46] J. K. Gimzewski, E. Stoll, and R. R. Schlittler. Scanning Tunneling Microscopy of Individual Molecules of Copper Phthalocyanine Adsorbed on Polycrystalline Silver Surfaces. *Surface Science*, 181(1-2):267–277, 1987.
- [47] D. P. E. Smith, A. Bryant, C. F. Quate, J. P. Rabe, C. Gerber, and J. D. Swalen. Images of a Lipid Bilayer at Molecular Resolution by Scanning Tunneling Microscopy. *Proceedings of the National Academy of Sciences of the United States of America*, 84(4):969–972, 1987.
- [48] D. P. E. Smith, M. D. Kirk, and C. F. Quate. Molecular Images and Vibrational Spectroscopy of Sorbic Acid with the Scanning Tunneling Microscope. *Journal of Chemical Physics*, 86(11):6034–6038, 1987.
- [49] S. U. Nanayakkara, E. C. H. Sykes, L. C. Fernandez-Torres, M. M. Blake, and P. S. Weiss. Long-range electronic interactions at a high temperature: Bromine adatom islands on Cu(111). *Physical Review Letters*, 98(20):206108, 2007.
- [50] T. Zambelli, J. Winterlin, J. Trost, and G. Ertl. Identification of the "active sites" of a surface-catalyzed reaction. *Science*, 273(5282):1688–1690, 1996.
- [51] N. D. Lang. Vacuum Tunneling Current from an Adsorbed Atom. *Physical Review Letters*, 55(2):230–233, 1985.
- [52] N. D. Lang. Theory of Single-Atom Imaging in the Scanning Tunneling Microscope. *Physical Review Letters*, 56(11):1164–1167, 1986.
- [53] P. Sautet and C. Joachim. Electronic Transmission Coefficient for the Single-Impurity Problem in the Scattering-Matrix Approach. *Physical Review B*, 38(17):12238–12247, 1988.
- [54] P. S. Weiss and D. M. Eigler. Site Dependence of the Apparent Shape of a Molecule in Scanning Tunneling Microscope Images - Benzene on Pt(111). *Physical Review Letters*, 71(19):3139–3142, 1993.

-
- [55] P. Sautet and M. L. Bocquet. Shape of molecular adsorbates in STM images: A theoretical study of benzene on Pt(111). *Physical Review B*, 53(8):4910–4925, 1996.
- [56] P. Sautet. Images of adsorbates with the scanning tunneling microscope: Theoretical approaches to the contrast mechanism. *Chemical Reviews*, 97(4):1097–1116, 1997.
- [57] R. Gutzler, W. M. Heckl, and M. Lackinger. Combination of a Knudsen effusion cell with a quartz crystal microbalance: In situ measurement of molecular evaporation rates with a fully functional deposition source. *Review of Scientific Instruments*, 81(1):015108, 2010.
- [58] V. T. Binh and J. Marien. Characterization of Microtips for Scanning Tunneling Microscopy. *Surface Science*, 202(1-2):L539–L549, 1988.
- [59] O. Albrektsen, H. W. M. Salemink, K. A. Morch, and A. R. Tholen. Reliable Tip Preparation for High-Resolution Scanning-Tunneling-Microscopy. *Journal of Vacuum Science & Technology B*, 12(6):3187–3190, 1994.
- [60] D. K. Biegelsen, F. A. Ponce, and J. C. Tramontana. Simple Ion Milling Preparation of (111)Tungsten Tips. *Applied Physics Letters*, 54(13):1223–1225, 1989.
- [61] George A. Jeffrey. *An introduction to hydrogen bonding*. Topics in physical chemistry. Oxford University Press, New York, 1997.
- [62] L. J. Prins, D. N. Reinhoudt, and P. Timmerman. Noncovalent synthesis using hydrogen bonding. *Angewandte Chemie-International Edition*, 40(13):2382–2426, 2001.
- [63] H. Tsubomura. Nature of the Hydrogen Bond .2. The Effect of Hydrogen Bonding and Other Solute-Solvent Interactions Upon the Shape and Intensity of the Infrared Oh Band of Phenol. *Journal of Chemical Physics*, 23(11):2130–2133, 1955.
- [64] H. Tsubomura. Nature of the Hydrogen Bond .3. The Measurement of the Infrared Absorption Intensities of Free and Hydrogen-Bonded Oh Bands - Theory of the Increase of the Intensity Due to the Hydrogen Bond. *Journal of Chemical Physics*, 24(5):927–931, 1956.
- [65] G. R. Desiraju. Supramolecular Synthons in Crystal Engineering - a New Organic-Synthesis. *Angewandte Chemie-International Edition in English*, 34(21):2311–2327, 1995.
- [66] P. W. Atkins. *Physical chemistry*. W.H. Freeman, New York, 3rd edition, 1986.
- [67] M. Lackinger and W. M. Heckl. Carboxylic Acids: Versatile Building Blocks and Mediators for Two-Dimensional Supramolecular Self-Assembly. *Langmuir*, 25(19):11307–11321, 2009.

- [68] G. Gilli, F. Bellucci, V. Ferretti, and V. Bertolasi. Evidence for Resonance-Assisted Hydrogen-Bonding from Crystal-Structure Correlations on the Enol Form of the Beta-Diketone Fragment. *Journal of the American Chemical Society*, 111(3):1023–1028, 1989.
- [69] P. Gilli, V. Bertolasi, V. Ferretti, and G. Gilli. Covalent Nature of the Strong Homonuclear Hydrogen-Bond - Study of the O-H—O System by Crystal-Structure Correlation Methods. *Journal of the American Chemical Society*, 116(3):909–915, 1994.
- [70] P. Gilli, V. Bertolasi, L. Pretto, V. Ferretti, and G. Gilli. Covalent versus electrostatic nature of the strong hydrogen bond: Discrimination among single, double, and asymmetric single-well hydrogen bonds by variable-temperature X-ray crystallographic methods in beta-diketone enol RAHB systems. *Journal of the American Chemical Society*, 126(12):3845–3855, 2004.
- [71] C. F. Guerra and F. M. Bickelhaupt. Charge transfer and environment effects responsible for characteristics of DNA base pairing. *Angewandte Chemie-International Edition*, 38(19):2942–2945, 1999.
- [72] O. Hassel. Structural Aspects of Interatomic Charge-Transfer Bonding. *Science*, 170(3957):497–, 1970.
- [73] P. Metrangolo and G. Resnati. Halogen bonding: A paradigm in supramolecular chemistry. *Chemistry-a European Journal*, 7(12):2511–2519, 2001.
- [74] T. B. Richardson, S. deGala, R. H. Crabtree, and P. E. M. Siegbahn. Unconventional hydrogen bonds: Intermolecular B-H center dot center dot center dot H-N interactions. *Journal of the American Chemical Society*, 117(51):12875–12876, 1995.
- [75] E. Bosch and C. L. Barnes. Triangular halogen-halogen-halogen interactions as a cohesive force in the structures of trihalomesitylenes. *Crystal Growth & Design*, 2(4):299–302, 2002.
- [76] F. F. Awwadi, R. D. Willett, S. F. Haddad, and B. Twamley. The electrostatic nature of aryl-bromine-halide synthons: The role of aryl-bromine-halide synthons in the crystal structures of the trans-bis(2-bromopyridine)dihalocopper(II) and trans-bis(3-bromopyridine)dihalocopper(II) complexes. *Crystal Growth & Design*, 6(8):1833–1838, 2006.
- [77] F. F. Awwadi, R. D. Willett, K. A. Peterson, and B. Twamley. The nature of halogen ... halogen synthons: Crystallographic and theoretical studies. *Chemistry-a European Journal*, 12(35):8952–8960, 2006.
- [78] S. Leininger, B. Olenyuk, and P. J. Stang. Self-assembly of discrete cyclic nanostructures mediated by transition metals. *Chemical Reviews*, 100(3):853–907, 2000.

- [79] B. J. Holliday and C. A. Mirkin. Strategies for the construction of supramolecular compounds through coordination chemistry. *Angewandte Chemie-International Edition*, 40(11):2022–2043, 2001.
- [80] M. Ruben, J. Rojo, F. J. Romero-Salguero, L. H. Uppadine, and J. M. Lehn. Grid-type metal ion architectures: Functional metallosupramolecular arrays. *Angewandte Chemie-International Edition*, 43(28):3644–3662, 2004.
- [81] M. Eddaoudi, J. Kim, N. Rosi, D. Vodak, J. Wachter, M. O’Keeffe, and O. M. Yaghi. Systematic design of pore size and functionality in isorecticular MOFs and their application in methane storage. *Science*, 295(5554):469–472, 2002.
- [82] Z. Y. Zhang, J. Zhang, T. Wu, X. H. Bu, and P. Y. Feng. Three-Dimensional Open Framework Built from Cu-S Icosahedral Clusters and Its Photocatalytic Property. *Journal of the American Chemical Society*, 130(46):15238–15239, 2008.
- [83] S. Stepanow, N. Lin, D. Payer, U. Schlickum, F. Klappenberger, G. Zoppellaro, M. Ruben, H. Brune, J. V. Barth, and K. Kern. Surface-assisted assembly of 2D metal-organic networks that exhibit unusual threefold coordination symmetry. *Angewandte Chemie-International Edition*, 46(5):710–713, 2007.
- [84] S. Stepanow, M. Lingenfelder, A. Dmitriev, H. Spillmann, E. Delvigne, N. Lin, X. B. Deng, C. Z. Cai, J. V. Barth, and K. Kern. Steering molecular organization and host-guest interactions using two-dimensional nanoporous coordination systems. *Nature Materials*, 3(4):229–233, 2004.
- [85] M. Matena, M. Stohr, T. Riehm, J. Bjork, S. Martens, M. S. Dyer, M. Persson, J. Lobo-Checa, K. Muller, M. Enache, H. Wadepohl, J. Zegenhagen, T. A. Jung, and L. H. Gade. Aggregation and Contingent Metal/Surface Reactivity of 1,3,8,10-Tetraazaperopyrene (TAPP) on Cu(111). *Chemistry-a European Journal*, 16(7):2079–2091, 2010.
- [86] C. C. Perry, S. Haq, B. G. Frederick, and N. V. Richardson. Face specificity and the role of metal adatoms in molecular reorientation at surfaces. *Surface Science*, 409(3):512–520, 1998.
- [87] G. Pawin, K. L. Wong, D. Kim, D. Z. Sun, L. Bartels, S. Hong, T. S. Rahman, R. Carp, and M. Marsella. A Surface Coordination Network Based on Substrate-Derived Metal Adatoms with Local Charge Excess. *Angewandte Chemie-International Edition*, 47(44):8442–8445, 2008.
- [88] N. N. Greenwood and A. Earnshaw. *Chemistry of the elements*. Pergamon Press, Oxford Oxfordshire ; New York, 1st edition, 1984.
- [89] J. He, C. Yang, Z. T. Xu, M. Zeller, A. D. Hunter, and J. H. Lin. Building thiol and metal-thiolate functions into coordination nets: Clues from a simple molecule. *Journal of Solid State Chemistry*, 182(7):1821–1826, 2009.

- [90] L. Kankate, A. Turchanin, and A. Golzhauser. On the Release of Hydrogen from the S-H groups in the Formation of Self-Assembled Monolayers of Thiols. *Langmuir*, 25(18):10435–10438, 2009.
- [91] S. A. Sardar, J. A. Syed, E. Ikenaga, S. Yagi, T. Sekitani, S. Wada, M. Taniguchi, and K. Tanaka. Orientation and charge transfer upon adsorption of ethanethiol on Cu(111) surface at 85 K. *Nuclear Instruments & Methods in Physics Research Section B-Beam Interactions with Materials and Atoms*, 199:240–243, 2003.
- [92] M. Konopka, R. Turansky, M. Dubecky, D. Marx, and I. Stich. Molecular Mechanochemistry Understood at the Nanoscale: Thiolate Interfaces and Junctions with Copper Surfaces and Clusters. *Journal of Physical Chemistry C*, 113(20):8878–8887, 2009.
- [93] S. M. Driver and D. P. Woodruff. Scanning tunnelling microscopy study of the interaction of dimethyl disulphide with Cu(111). *Surface Science*, 457(1-2): 11–23, 2000.
- [94] H. Keller, P. Simak, W. Schrepp, and J. Dembowski. Surface-Chemistry of Thiols on Copper - an Efficient Way of Producing Multilayers. *Thin Solid Films*, 244(1-2):799–805, 1994.
- [95] A. Ferral, P. Paredes-Olivera, V. A. Macagno, and E. M. Patrito. Chemisorption and physisorption of alkanethiols on Cu(111). A quantum mechanical investigation. *Surface Science*, 525(1-3):85–99, 2003.
- [96] M. Giesen. Step and island dynamics at solid/vacuum and solid/liquid interfaces. *Progress in Surface Science*, 68(1-3):1–153, 2001.
- [97] K. S. Novoselov, A. K. Geim, S. V. Morozov, D. Jiang, Y. Zhang, S. V. Dubonos, I. V. Grigorieva, and A. A. Firsov. Electric field effect in atomically thin carbon films. *Science*, 306(5296):666–669, 2004.
- [98] A. K. Geim and K. S. Novoselov. The rise of graphene. *Nature Materials*, 6(3): 183–191, 2007.
- [99] S. Stankovich, D. A. Dikin, G. H. B. Dommett, K. M. Kohlhaas, E. J. Zimney, E. A. Stach, R. D. Piner, S. T. Nguyen, and R. S. Ruoff. Graphene-based composite materials. *Nature*, 442(7100):282–286, 2006.
- [100] E. Stolyarova, D. Stolyarov, K. Bolotin, S. Ryu, L. Liu, K. T. Rim, M. Klima, M. Hybertsen, I. Pogorelsky, I. Pavlishin, K. Kusche, J. Hone, P. Kim, H. L. Stormer, V. Yakimenko, and G. Flynn. Observation of Graphene Bubbles and Effective Mass Transport under Graphene Films. *Nano Letters*, 9(1):332–337, 2009.
- [101] F. Chen and N. J. Tao. Electron Transport in Single Molecules: From Benzene to Graphene. *Accounts of Chemical Research*, 42(3):429–438, 2009.
- [102] P. Avouris, Z. H. Chen, and V. Perebeinos. Carbon-based electronics. *Nature Nanotechnology*, 2(10):605–615, 2007.

-
- [103] K. S. Novoselov, Z. Jiang, Y. Zhang, S. V. Morozov, H. L. Stormer, U. Zeitler, J. C. Maan, G. S. Boebinger, P. Kim, and A. K. Geim. Room-temperature quantum hall effect in graphene. *Science*, 315(5817):1379–1379, 2007.
- [104] L. Grill, M. Dyer, L. Lafferentz, M. Persson, M. V. Peters, and S. Hecht. Nano-architectures by covalent assembly of molecular building blocks. *Nature Nanotechnology*, 2(11):687–691, 2007.
- [105] N. A. A. Zwaneveld, R. Pawlak, M. Abel, D. Catalin, D. Gigmès, D. Bertin, and L. Porte. Organized formation of 2D extended covalent organic frameworks at surfaces. *Journal of the American Chemical Society*, 130(21):6678–6679, 2008.
- [106] F. Ullmann and J. Bielecki. Synthesis in the Biphenyl series. (I. Announcement). *Berichte Der Deutschen Chemischen Gesellschaft*, 34:2174–2185, 1901.
- [107] R. Gutzler, H. Walch, G. Eder, S. Kloft, W. M. Heckl, and M. Lackinger. Surface mediated synthesis of 2D covalent organic frameworks: 1,3,5-tris(4-bromophenyl)benzene on graphite(001), Cu(111), and Ag(110). *Chemical Communications*, (29):4456–4458, 2009.
- [108] J. A. Lipton-Duffin, O. Ivasenko, D. F. Perepichka, and F. Rosei. Synthesis of Polyphenylene Molecular Wires by Surface-Confined Polymerization. *Small*, 5(5):592–597, 2009.
- [109] H. Ibach. *Physics of surfaces and interfaces*. Springer, Berlin ; New York, 2006.
- [110] Kurt W. Kolasinski. *Surface science : foundations of catalysis and nanoscience*. Wiley, Chichester, England ; Hoboken, NJ, 2nd edition, 2008.
- [111] S. Griessl, M. Lackinger, M. Edelwirth, M. Hietschold, and W. M. Heckl. Self-assembled two-dimensional molecular host-guest architectures from trimesic acid. *Single Molecules*, 3(1):25–31, 2002.
- [112] M. Lackinger, S. Griessl, W. A. Heckl, M. Hietschold, and G. W. Flynn. Self-assembly of trimesic acid at the liquid-solid interface - a study of solvent-induced polymorphism. *Langmuir*, 21(11):4984–4988, 2005.
- [113] L. Kampschulte, M. Lackinger, A. K. Maier, R. S. K. Kishore, S. Griessl, M. Schmittel, and W. M. Heckl. Solvent induced polymorphism in supramolecular 1,3,5-benzenetribenzoic acid monolayers. *Journal of Physical Chemistry B*, 110(22):10829–10836, 2006.
- [114] L. Kampschulte, T. L. Werblowsky, R. S. K. Kishore, M. Schmittel, W. M. Heckl, and M. Lackinger. Thermodynamical equilibrium of binary supramolecular networks at the liquid-solid interface. *Journal of the American Chemical Society*, 130(26):8502–8507, 2008.
- [115] D. M. Newns. Self-Consistent Model of Hydrogen Chemisorption. *Physical Review*, 178(3):1123, 1969.
- [116] P. W. Anderson. Localized Magnetic States in Metals. *Physical Review*, 1(1):41, 1961.

- [117] B. Hammer and J. K. Norskov. Theoretical surface science and catalysis - Calculations and concepts. *Advances in Catalysis, Vol 45*, 45:71–129, 2000.
- [118] Axel Gross. *Theoretical surface science : a microscopic perspective*. Advanced texts in physics,. Springer, Berlin ; New York, 2003.
- [119] John Venables. *Introduction to surface and thin film processes*. Cambridge University Press, Cambridge, UK ; New York, 2000.
- [120] J. Friedel. Band-Structure of Transition-Metals. *Journal of Physics F-Metal Physics*, 3(4):785–794, 1973.
- [121] J. B. Neaton, M. S. Hybertsen, and S. G. Louie. Renormalization of molecular electronic levels at metal-molecule interfaces. *Physical Review Letters*, 97(21):216405, 2006.
- [122] K. S. Thygesen and A. Rubio. Renormalization of Molecular Quasiparticle Levels at Metal-Molecule Interfaces: Trends across Binding Regimes. *Physical Review Letters*, 102(4):046802, 2009.
- [123] J. M. Garcia-Lastra, C. Rostgaard, A. Rubio, and K. S. Thygesen. Polarization-induced renormalization of molecular levels at metallic and semiconducting surfaces. *Physical Review B*, 80(24):245427, 2009.
- [124] Michael Schunack. *Scanning Tunneling Microscopy Studies of Organic Molecules on Metal Surfaces*. PhD thesis, University of Aarhus, Denmark, 2002.
- [125] B. Hammer and J. K. Norskov. Why Gold Is the Noblest of All the Metals. *Nature*, 376(6537):238–240, 1995.
- [126] J. K. Norskov. Effective Medium Potentials for Molecule-Surface Interactions - H-2 on Cu and Ni Surfaces. *Journal of Chemical Physics*, 90(12):7461–7471, 1989.
- [127] H. S. Taylor. A theory of the catalytic surface. *Proceedings of the Royal Society of London Series a-Containing Papers of a Mathematical and Physical Character*, 108(745):105–111, 1925.
- [128] W. K. Burton, N. Cabrera, and F. C. Frank. The Growth of Crystals and the Equilibrium Structure of Their Surfaces. *Philosophical Transactions of the Royal Society of London Series a-Mathematical and Physical Sciences*, 243(866):299–358, 1951.
- [129] J. K. Norskov, T. Bligaard, B. Hvolbaek, F. Abild-Pedersen, I. Chorkendorff, and C. H. Christensen. The nature of the active site in heterogeneous metal catalysis. *Chemical Society Reviews*, 37(10):2163–2171, 2008.
- [130] G. A. Somorjai, R. W. Joyner, and B. Lang. Reactivity of Low Index [(111) and (100)] and Stepped Platinum Single-Crystal Surfaces. *Proceedings of the Royal Society of London Series A - Mathematical Physical and Engineering Sciences*, 331(1586):335–, 1972.

-
- [131] G. A. Somorjai, K. R. McCrea, and J. Zhu. Active sites in heterogeneous catalysis: development of molecular concepts and future challenges. *Topics in Catalysis*, 18(3-4):157–166, 2002.
- [132] J. T. Yates. Surface-Chemistry at Metallic Step Defect Sites. *Journal of Vacuum Science & Technology a-Vacuum Surfaces and Films*, 13(3):1359–1367, 1995.
- [133] T. Zubkov, G. A. Morgan, J. T. Yates, O. Kuhlert, M. Lisowski, R. Schillinger, D. Fick, and H. J. Jansch. The effect of atomic steps on adsorption and desorption of CO on Ru(109). *Surface Science*, 526(1-2):57–71, 2003.
- [134] P. Gambardella, Z. Sljivancanin, B. Hammer, M. Blanc, K. Kuhnke, and K. Kern. Oxygen dissociation at Pt steps. *Physical Review Letters*, 8705(5):056103, 2001.
- [135] R. T. Vang, K. Honkala, S. Dahl, E. K. Vestergaard, J. Schnadt, E. Laegsgaard, B. S. Clausen, J. K. Norskov, and F. Besenbacher. Controlling the catalytic bond-breaking selectivity of Ni surfaces by step blocking. *Nature Materials*, 4(2):160–162, 2005.
- [136] M. G. Lagally and Z. Y. Zhang. Materials science - Thin-film cliffhanger. *Nature*, 417(6892):907–910, 2002.
- [137] N. Lin, D. Payer, A. Dmitriev, T. Strunskus, C. Woll, J. V. Barth, and K. Kern. Two-dimensional adatom gas bestowing dynamic heterogeneity on surfaces. *Angewandte Chemie-International Edition*, 44(10):1488–1491, 2005.
- [138] C. M. Chang and C. M. Wei. Self-diffusion of adatoms and dimers on fcc(100) surfaces. *Chinese Journal of Physics*, 43(1):169–175, 2005.
- [139] Markus Wahl. *Reactions of Organic Molecules on Metal Surfaces studied by STM*. PhD thesis, University of Basel, Switzerland, 2006.
- [140] C. L. Liu, J. M. Cohen, J. B. Adams, and A. F. Voter. Eam Study of Surface Self-Diffusion of Single Adatoms of Fcc Metals Ni, Cu, Al, Ag, Au, Pd, and Pt. *Surface Science*, 253(1-3):334–344, 1991.
- [141] E. Bauer. LEEM basics. *Surface Review and Letters*, 5(6):1275–1286, 1998.
- [142] J. la Figuera, N. C. Bartelt, and K. F. McCarty. Electron reflectivity measurements of Ag adatom concentrations on W(110). *Surface Science*, 600(18):4062–4066, 2006.
- [143] S. Stepanow, N. Lin, J. V. Barth, and K. Kern. Surface-template assembly of two-dimensional metal-organic coordination networks. *Journal of Physical Chemistry B*, 110(46):23472–23477, 2006.
- [144] Y. F. Zhang, N. Zhu, and T. Komeda. Programming of a Mn-coordinated 4-4'-biphenyl dicarboxylic acid nanosystem on Au(111) and investigation of the non-covalent binding of C60 molecules. *Surface Science*, 602(2):614–619, 2008.

- [145] U. Schlickum, R. Decker, F. Klappenberger, G. Zoppellaro, S. Klyatskaya, M. Ruben, I. Silanes, A. Arnau, K. Kern, H. Brune, and J. V. Barth. Metal-organic honeycomb nanomeshes with tunable cavity size. *Nano Letters*, 7(12): 3813–3817, 2007.
- [146] N. Romero-Isart and M. Vasak. Advances in the structure and chemistry of metallothioneins. *Journal of Inorganic Biochemistry*, 88(3-4):388–396, 2002.

Acknowledgements

It is a pleasure for me to finally thank those people who made this thesis possible. First and foremost I would like to thank my supervisor Prof. Markus Lackinger for giving me the opportunity to be part of his research group. His enormous support and advice in both, scientific questions and practical issues in the daily lab routine made me learn a lot and this work a very enjoyable time. Always having enough space and freedom was surely an additional motivation for me.

I am also grateful to Prof. Wolfgang Heckl who introduced me into the field of Nanoscience and Scanning Probe Techniques back in my undergraduate studies. Special thanks go also to Prof. Stefan Sotier for his help in various UHV issues and his constant supply of materials from his own lab.

I want to thank the members of the STM group who all contributed either way to this thesis. It has always been a great atmosphere working within the team. Especially I want to mention my fellow sufferer Rico Gutzler, who also had to learn the UHV business from scratch and was thus facing the same difficulties and problems in the beginning. This made life a lot easier. Thanks to Jürgen Dienstmayer and Georg Eder for the good teamwork we shared, particularly in the copper-thiolate project. Thanks to Anne-Kathrin Maier for providing a steady supply of STM images in the melamine project. But of course, this thesis would not have been possible without the support in a number of ways from all group members. Thank you to past and present group members and colleagues for fruitful discussions, proofreading of this thesis and not to neglect extracurricular activities: Marek Janko, Johanna Eichhorn, Alex Gigler, Christoph Heining, Michael Bauer, Stefan Schlögl, Stefan Kloft, Thommi Sirtl, Maria Wieland, and Sophie Lappe.

Prof. Michael Schmittel and his research group at the University of Siegen are acknowledged for providing many of the molecular samples and for helpful discussions. I would like point out the good collaboration I received from all the people from the mechanical and electronic workshops. Günther Hesberg and his team did a great job machining all sorts of components for our UHV system. Max Häberle and Detlef Körner I thank for fixing amplifiers, controllers, transformers, in short, everything that was needed to keep the instruments running.

Finally, I want to express my gratitude to my family and all my friends for the constant support I received during my studies.

Curriculum Vitae

Personal

Name	Hermann Heinrich Siegfried Walch
Birth	14.02.1979
in	Tegernsee

University

since 2006	PhD candidate, LMU Munich
2006	Diploma geophysics
2002 - 2006	Studies of geophysics, LMU Munich
2001 - 2002	Studies of physics, Uppsala University, Sweden
1998 - 2001	Studies of geophysics, LMU Munich

Education

1998	Abitur (general qualification for university entrance)
1989 - 1998	Secondary School, Gymnasium Tegernsee
1985 - 1989	Primary School, Kreuth

Practical Experience

2003 - 2004	Working student at Infineon Technologies, Munich
2002 - 2003	Working student, LMU Munich, seismological observatory
2002	Project work, Uppsala University, solid earth physics section
2001	Working student, LMU Munich, geophysics section